Science of the Total Environment 866 (2023) 161225

Contents lists available at ScienceDirect

Science of the Total Environment

journal homepage: www.elsevier.com/locate/scitotenv

Engine, aftertreatment, fuel quality and non-tailpipe achievements to lower gasoline vehicle PM emissions: Literature review and future prospects

M. Matti Maricq

Forest Glen Consulting, Brighton, UT, USA

HIGHLIGHTS

- Detailed analysis of engine technology advances that reduce PM emissions.
- Assessment of gasoline particulate filter capability to achieve ultra-low PM emissions.
- Examination of the particulate matter index and fuel effects on gasoline vehicle PM.
- Analyses of brake, tire and road wear PM emissions.
- Comparison of total vehicle PM emissions from gasoline versus battery electric vehicles.

ARTICLE INFO

Editor: Philip K. Hopke

Keywords:
Gasoline vehicle
PM emissions
Brake & tire emissions
Soot
Transportation

GRAPHICAL ABSTRACT

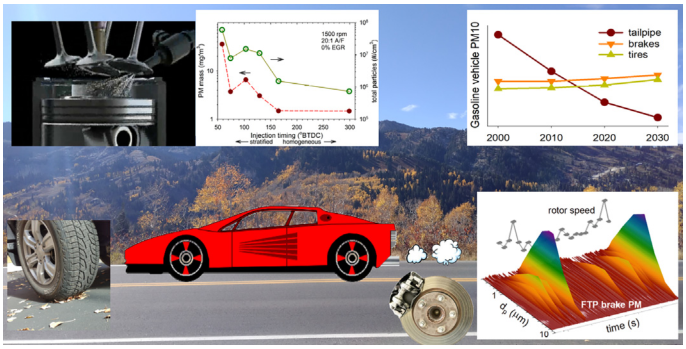

ABSTRACT

Spark ignition gasoline vehicles comprise most light duty vehicles worldwide. These vehicles were not historically associated with PM emissions. This changed about 15 years ago when emissions regulations forced diesel engines to employ exhaust particulate filters and fuel economy requirements ushered in gasoline direct injection (GDI) technology. These shifts reversed the roles of gasoline and diesel vehicles, with GDI vehicles now regarded as the high PM emitters. Regulators worldwide responded with new or revised PM emissions standards. This review takes a comprehensive look at PM emissions from gasoline vehicles. It examines the technological advances that made it possible for GDI vehicles to meet even the most stringent tailpipe PM standards. These include fuel injection strategies and injector designs to limit fuel films in the engine cylinder that were pathways for soot formation and the development of gasoline particle filters to remove PM from engine exhaust. The review also examines non-exhaust PM emissions from brake, tire, and road wear, which have become the dominant sources of vehicle derived PM. Understanding the low levels of GDI tailpipe PM emissions that have been achieved and its contribution to total vehicle PM emissions is essential for the current debate about the future of internal combustion engines versus rapidly evolving battery electric vehicles. In this context, it does not make sense to consider BEVs as zero emitting vehicles. Rather, a more holistic framework is needed to compare the relative merits of various vehicle powertrains.

Contents

E-mail address: mattimaricq@gmail.com.

http://dx.doi.org/10.1016/j.scitotenv.2022.161225
Received 16 October 2022; Received in revised form 12 December 2022; Accepted 23 December 2022
Available online 31 December 2022

1. Introduction

Motor vehicle exhaust emissions are currently regulated throughout the world owing to their environmental and health impacts. Historically, regulations have targeted ambient concentrations of ozone, particulate matter (PM), nitrogen dioxide, carbon monoxide, sulfur dioxide, and lead (Code of Federal Regulations, 2022a). Ozone is not directly emitted from combustion engines, but its tropospheric concentration is a strong function of local hydrocarbon and NO_x levels (Seinfeld and Pandis, 2016); therefore, vehicle emissions standards apply to these compounds (Code of Federal Regulations, 2022b). Switching to unleaded gasoline markedly lowered atmospheric concentrations of lead (U.S. Environmental Protection Agency, 1986) and, similarly, the introduction of three-way and oxidation catalysts has significantly reduced motor vehicle contributions to atmospheric CO (Lowry et al., 2016). Thus, the main constituents currently dominating air quality are ozone and PM. Additionally, NO_2, aldehydes and ammonia remain potential health concerns, and carbon dioxide, nitrous oxide, and methane have been added to the list of regulated exhaust species owing to their impact on climate change (U.S. Environmental Protection Agency, 2021a).

PM adversely impacts both air quality (McDuffie et al., 2021) and climate change (IPCC, 2014). The modern era of PM emissions regulations began with health concerns raised by epidemiological research findings in the early 1990's, such as from the Six Cities (Dockery et al., 1993) and Utah Valley steel mill closure (Pope, 1989) studies. The adverse effects of PM exposure were already known from the aftermath of incidents such as the great smog of London during the winter of 1952 (Martinez, 2021). Thus, United States and European regulations at the time included PM emissions standards. U.S. Environmental Protection Agency (EPA) Tier 1 and California Air Resources Board (CARB) LEV standards limited PM mass emissions to 80 mg/mi for light duty (LD) vehicles and progressively lowered the heavy duty (HD) engine PM emissions from 600 to 100 mg/bhp-hr between 1990 and 1994 (DieselNet, 2021). Euro 1 & 2 standards for diesel engines were comparable, whereas PM from gasoline vehicles was not regulated. The required reductions for diesel engines were met by changing from indirect to direct fuel injection, increasing injection pressure, and using post injection to help burn out the soot formed during combustion (Stumpp and Ricco, 1996; Guerrassi and Dupraz, 1998; Park et al., 2004). On the other hand, 1990's gasoline vehicles already exhibited PM emissions well below the standards (Ristovski et al., 1998; Maricq et al., 1999b; Zhang et al., 2010), so no engineering changes were necessary.

Weak but consistent associations between daily mortality and elevated PM levels revealed by 1990s epidemiological studies (Dominici, 2004), however, starkly highlighted a connection between PM exposure and health that sparked an order of magnitude increase in PM emissions stringency. U.S. EPA Tier 2 and CARB LEV II standards lowered PM mass limits to 10 mg/mi and the 2007 HD diesel engine regulations limited emissions to 10 mg/bhp-hr (DieselNet, 2021). The European Union went further. Unsatisfied with the progress made by OEMs to reduce PM mass emissions, it enacted a solid particle number (SPN) standard (Giechaskiel et al., 2008). Euro 5b regulations set a SPN emissions standard of $6{\cdot}10^{11}$ particles/km for light duty diesel vehicles and Euro 6 introduced an $8{\cdot}10^{11}$ particles/kWh HD diesel limit (DieselNet, 2021). Owing to the correlation between mass and number exhibited by combustion engine soot (Johnson and Joshi, 2018), this translates to an approximately 0.5 mg/km (1 mg/kWh) mass standard, a roughly 200-fold increase in stringency from Euro 2. The dramatic reductions in both U.S. and European PM emissions limits forced the development of new diesel engine aftertreatment technology, primarily the diesel particulate filter (DPF) (Khair, 2003). Gasoline vehicles, in contrast, remained unaffected by the new standards.

The situation with gasoline vehicles changed dramatically with the introduction of gasoline direct injection engine technology (Iwamoto et al., 1997; Davis et al., 2009; Yi et al., 2009; Shuai et al., 2018). Direct injection of fuel into the cylinder instead of the conventional approach of injecting onto a closed intake port affords opportunities to reduce fuel consumption and CO_2 emissions through higher efficiency (Kuwahara et al., 1998; Alkidas and El Tahry, 2003), boosting (Bandel et al., 2006), and downsizing (Fraser et al., 2009). This offered an attractive alternative to fuel cell or battery electric powertrains to achieve the glide path for fuel economy and CO_2 emissions improvement requirements that were being ushered in during the Obama administration (White House and Office of the Press Secretary, 2012). The advantage of GDI engines was that they represented a drop-in replacement for the existing port fuel injection (PFI) gasoline engines that did not require the technology and infrastructure changes needed for fuel cell or battery powered propulsion. However, this engine design risks impingement of fuel onto the piston and cylinder walls as well as incomplete fuel spray evaporation and mixing, which leads to soot formation (Myung et al., 2014; Fang et al., 2017). OEMs that introduced the first production vehicles using GDI engines calibrated the engines to mitigate these situations and achieved PM emissions levels that met the existing 10 mg/mi standard.

GDI technology proved very successful. Its market penetration was rapid, ~50 % within a decade, and it had an immediate impact on improving fuel economy and CO_2 emissions, as illustrated by Fig. 1. Although they met Tier 2 / LEV II standards, early GDI vehicles emitted substantially more PM than their PFI counterparts, for example, 1.5–8 mg/mi (Zhang and McMahon, 2012) instead of 0.5–2 mg/mi (Maricq et al., 1999b) for the weighted average mass over the Federal Test Procedure (FTP) drive cycle. This led to concerns about “backsliding”, namely that a relatively clean fleet of PFI gasoline vehicles would be replaced by a substantially higher PM emitting fleet of GDI vehicles (California Air Resources Board, 2010).

This potential increase in mobile source PM, an expanding literature of adverse health associations, e.g., with ultrafine particles (HEI Review Panel on Ultrafine Particles, 2013), and a growing environmental justice movement (Bolte et al., 2011) contributed to further tightening of U.S. PM emissions standards from 10 to 3 mg/mi under Tier 3 and LEV III regulations (DieselNet, 2021). These standards recently concluded the 2017–2021 phase-in period. CARB's LEV III program will go a step farther and limit PM mass emissions to 1 mg/mi beginning in 2025. This will bring the California mass-based standard to an essentially equivalent stringency with the European number standard, except that it applies to total exhaust PM, and not solely the solid component.

Also concerned about a rise in motor vehicle PM, Europe used its EU6 regulations to extend the solid particle number limit to GDI vehicles. It introduced Real Driving Emissions regulations (Hooftman et al., 2018) to overcome potential manipulation of dynamometer testing. China and much of the rest of the world have followed the European path (DieselNet, 2021). In November 2022 the European Commission proposed new Euro 7 standards, which include a number of notable changes (EU Commission, 2022): the new standards are fuel and technology neutral, they broaden the range of driving conditions and, importantly, they introduce for the first time limits on emissions from brakes and tires.

High PM emissions from early GDI vehicles as compared to PFI arose at least in part from unfamiliarity by engineers with how to optimize these new engines. The “calibration” process to program the engine control module (ECM) faces many simultaneous requirements; besides meeting fuel economy and emissions regulations, calibration needs to optimize engine power, torque, driving feel, transmission shift schedules, account for engine warm up, and protect components from excessive heat, to name a few. Owing to the larger number of calibration parameters for GDI engines, e.g., fuel injection timing and number of injections per cycle, the experience and rules of thumb from PFI engines did not immediately translate to GDI engines (Rodriguez and Cheng, 2015, 2016a). The past decade has seen numerous advances in engine technology and calibration, described in detail below, that have dramatically improved GDI vehicle tailpipe PM emissions. As Fig. 2 shows, new vehicle PM emissions, > 50 % of which are GDI, have steadily headed to below 3 mg/mi over the Tier 3 / LEV III phase-in period.

It is likely that most, if not all, GDI vehicles can meet a 3 mg/mi standard via engine design and optimization, without the need for exhaust filtration. It is unclear, however, to what extent this remains feasible at a 1 mg/mi or $6{\cdot}10^{11}$ particles/km SPN standard. At these low levels, measurement plays an increasingly important role. When setting emissions targets, manufacturers must account for their, and regulators', measurement uncertainty and aim for a level that is well below these standards. This uncertainty compounds the difficulty in identifying appropriate technology to meet the standards.

The motivation for the present review is to learn how advances in engine technology, aftertreatment, and fuel composition have enabled gasoline vehicles to meet dramatic increases in PM stringency over the past two decades and apply this knowledge to assess the ability to meet future PM standards, particularly CARB 1 mg/mi and EU and China SPN limits. Numerous reviews of GDI vehicle PM emissions already exist (Myung and Park, 2012; Choi et al., 2014; Myung et al., 2014; Fang et al., 2017; Karavalakis et al., 2018; Raza et al., 2018; Shuai et al., 2018; Qian et al., 2019; Awad et al., 2020), which raises the question: What new will the present review provide? The previous reviews give good summaries of various aspects of gasoline vehicle PM emissions research, such as how they vary with engine operating parameters and respond to changes in fuel formulation. The present review aims to distill from the literature the mechanisms for PM formation, their root causes, and the technical remedies available. It examines these questions holistically including both engine exhaust and non-exhaust sources of vehicle PM. This knowledge is critically

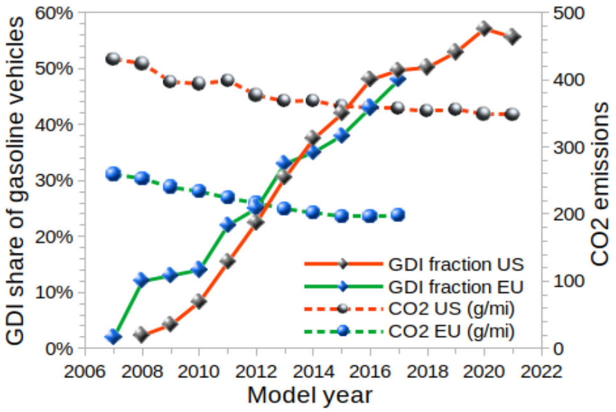

Fig. 1. United States and European GDI vehicle market penetration and CO_2 impact (averaged over all LD vehicles). US data (U.S. Environmental Protection Agency, 2021b); EU data (International Council on Clean Transportation, 2018).

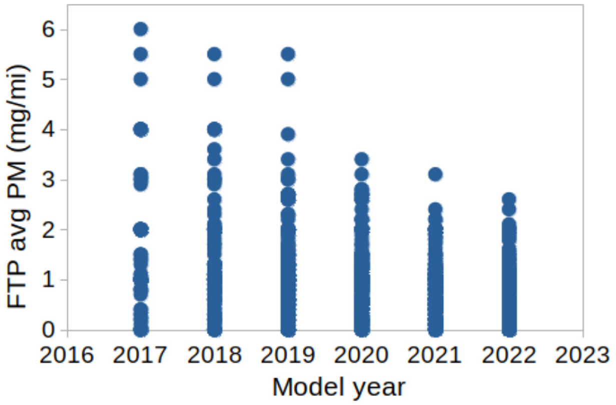

Fig. 2. United States PM emissions certification data for light duty vehicles (U.S. Environmental Protection Agency, 2021c). Data include both GDI and PFI vehicles, with the GDI fraction increasing to >50 %.

needed to ascertain the future role of gasoline vehicles in a transportation world that is becoming increasingly electrified and to inform policy decisions to best affect a transition from internal combustion engine to electrified vehicles.

Following this introduction, the review is divided into seven sections: 2. Engine Exhaust Particulate Matter, 3. PM Formation in Engines, 4. Gasoline Engine Technology Advances to Reduce PM, 5. Gasoline Vehicle PM Exhaust Aftertreatment, 6. Fuel and Lube Oil Impacts on PM, 7. Non-Tailpipe PM Emissions, and 8. Future Prospects. These sections are largely independent of each other; thus, readers wary of the review's length are encouraged to begin with Section 3, after which the remaining sections can be read in the order that most interests the reader.

2. Engine exhaust particulate matter

To gain insight into how advances in engine technology and exhaust aftertreatment have contributed to gasoline vehicles' ability to keep pace with tightening PM emissions standards, it is helpful to understand the nature of engine exhaust PM and how it is formed during combustion. This section examines the definition of PM as it is used scientifically as compared to regulatory language and summarizes the mechanisms of soot inception and growth in flames.

2.1. What defines PM?

Particulate matter has various definitions. Aerosol science defines it as a suspension of fine liquid or solid particles in a gas (Hinds, 1999). Emissions regulations define it operationally, i.e., via the measurement procedures described below. Fig. 3 illustrates room temperature engine exhaust aerosol, for example as it exists during filter collection from a dilution tunnel. Aerosols continually evolve. Initially, only carbonaceous particles with a high C/H ratio exist in the engine cylinder due to the high temperature of combustion, > 1000 °C, perhaps internally or externally mixed with a small amount of inorganic ash. This “soot” aerosol largely persists as 30–300 nm fractal-like aggregates through the exhaust system, where temperatures typically remain >300 °C.

When engine exhaust exits the tailpipe into a dilution tunnel, or ambient air, it cools rapidly. This causes condensation of semi-volatile organic compounds onto the soot and nucleation of sulfate and possibly some low volatility organic species into new nanoparticles, typically <10 nm in diameter. These processes alter PM mass and particle number, the latter often dramatically. The resulting particle size distribution is typically bimodal, with a ∼ 10 nm nucleation mode of organics and sulfate and a ∼ 70 nm accumulation mode of soot and condensed gases.

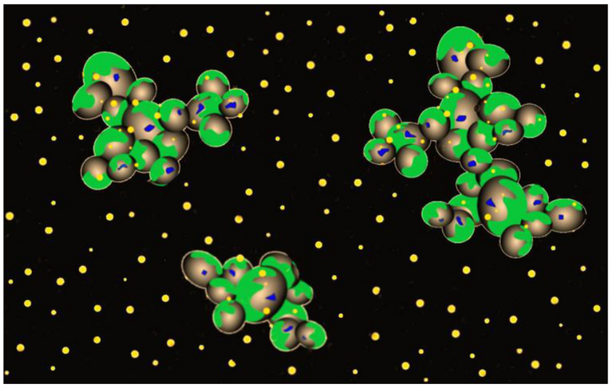

Fig. 3. Artist conception of engine exhaust aerosol as it exists at room temperature in a dilution tunnel. ● = carbon, 🔵 = ash, 🟢 = condensed semi-volatiles, 🟡 = nucleated sulfate / oil, and black background = suspending gas mixture (N_2, O_2, H_2O, CO_2, CO, NO_x, HCs, SO_x).

Exhaust aerosol continues to evolve in the dilution tunnel or ambient air owing to coagulation, partitioning of semivolatile species between particle and gas phase, deposition onto surfaces, and settling. As engine exhaust disperses in the atmosphere, photo-oxidation of some HC species by sunlight produces progressively lower volatility compounds, which partition into a secondary organic aerosol (SOA) (Odum et al., 1997).

Emissions regulations require a reproducible metric for PM; thus, they resort to operational definitions that seek to constrain the variability inherent to aerosols, as well as in the measurement process. This is true for both the U.S. EPA mass based and EU number-based definitions. The current U.S. EPA gravimetric method defines PM as the mass gain recorded on a teflon membrane or teflon coated fiber filter that samples diluted exhaust through a 2.5 mm cutpoint cyclone (Code of Federal Regulations, 2022c). The method was optimized prior to promulgating the 2007 EPA 10 mg/bhp-hr HD standard (Khalek, 2005) over concerns about reproducibility across test laboratories; therefore, specifications were tightened or added for the dilution ratio, temperature of diluted exhaust, sampling time, filter equilibration time, balance accuracy, buoyancy correction, and the temperature, humidity, and cleanliness of the weighing room. These were modified for light duty vehicles in EPA Title 40 Part 1066 regulations, for example specifying an average dilution factor between 7 and 20 over the test drive and allowing subtraction of up to the greater of 5 mg/filter or 5 % of the net mass to correct for background particles and gaseous adsorption onto the filter (Code of Federal Regulations, 2022d). These system constraints have proved successful, as they have allowed accurate mass determination at the 3 mg/mi LD standard, which at this level must distinguish an ∼0.1 mg weight gain by an ∼200 mg filter.

The EU solid number standard (Giechaskiel et al., 2021) is likewise operationally defined. Regulations dictate that diluted exhaust from a dilution tunnel pass through a thermodiluter or catalytic stripper to remove semi volatile particles (Abdul-Khalek and Kittelson, 1995; Swanson and Kittelson, 2010) and that the surviving particles larger than 23 nm (50 % cutpoint) are counted. The thermodiluter evaporates liquid droplets and prevents re-nucleation by dilution, whereas the catalytic stripper achieves this by evaporation, catalytic conversion of the evolved organic compounds, and trapping sulfur species. Possible evaporation of condensed material from the solid carbon particles is irrelevant since it does not affect particle count. The 23 nm lower cutpoint was included to avoid counting residual liquid particles that may not have completely evaporated. Concerns over possible solid sub-23 nm particle emissions under some vehicle operating conditions (Rönkkö et al., 2007; De Filippo and Maricq, 2008) and research demonstrating feasibility to accurately count solid particles below 23 nm (Samaras et al., 2020) have led to adoption of a 10 nm cutpoint in the EU 7 standards (Giechaskiel et al., 2021).

These operational definitions provide common bases for setting PM emission standards, as well as engineering targets to achieve these standards, but they are less useful to understand motor vehicles' atmospheric PM burden or to develop strategies to reduce their PM emissions. Consider, for example, the question: Does the catalytic converter reduce PM emissions? The catalyst does not directly remove particles; there is insufficient time for 10–500 nm soot particles to diffuse to the catalyst walls as the exhaust flows through the catalyst brick. However, the catalyst removes gaseous hydrocarbons that may condense onto solid particles or nucleate when the exhaust exits the tailpipe and cools; thus, it reduces the mass collected onto the filter from the dilution tunnel and, thus, PM emissions as defined by the EPA method.

Furthermore, the catalyst removes semi-volatile hydrocarbon precursors that form SOA via photochemical oxidation in the atmosphere (Robinson et al., 2007) and thereby reduces an atmospheric PM burden not included in the regulatory PM definition (Section 5.2). To avoid repeatability issues stemming from difficulties in measuring semivolatile particle number, the EU SPN standard effectively defines PM as the solid particles suspended in exhaust gas, which avoids the question of semi-volatile particles. The examination below of how advances in gasoline vehicles have improved PM emissions takes the broader view that includes semi-volatile contributions to direct PM emissions and SOA.

2.2. Particle formation by combustion

Except for a small fraction of particles aspirated into an engine via the intake air, the vast majority are generated via combustion. Not all flames produce soot. The task of reducing engine-out PM, therefore, amounts to identifying and mitigating the conditions that form soot, namely rich fuel air mixtures, and to promote soot oxidation after combustion.

The mechanism for soot formation in rich flames is very complex, with hundreds, if not thousands, of high temperature chemical reactions (Wang and Frenklach, 1997; Frenklach, 2002). The least well known, and an active area of research, are the pathways that produce incipient soot particles. This was historically thought to occur via formation of progressively larger polyaromatic hydrocarbons (PAHs) to the point where they condense into incipient particles. Recent research, however, points to alternative mechanisms involving resonance stabilized radical reactions that better fulfill the thermodynamic driving force needed at flame temperatures to produce particles (Wang, 2011; Johansson et al., 2018; Commodo et al., 2019).

A key element of soot formation is that it only occurs under sufficiently rich conditions. A premixed ethylene flame, for example, exhibits a non-sooting blue flame below an equivalence ratio of $\Phi = \sim 1.8$; but, above this it turns progressively brighter yellow from soot particle incandescence as their concentration and size rapidly increase at higher Φ (Maricq et al., 2003). Once formed, incipient soot particles grow from a combination of surface chemistry and coagulation. Surface growth occurs primarily via the H-abstraction-C_2H_2-addition (HACA) mechanism (Harris and Weiner, 1985; Xu et al., 1997; Frenklach, 2002). This begins when a gas phase hydrogen atom reacts with hydrogen on the soot surface to create a reactive radical site plus H_2. Then, acetylene, the principal soot growth species in a flame, adds to that site and releases one of its hydrogens. By retaining the other, the number of surface hydrogen atoms does not diminish. This establishes conditions for a chain reaction, which explains why this is the predominant mechanism for soot mass increase, that is, the conversion of gas phase to solid carbon. Coagulation, in contrast, does not alter mass; but it does increase particle size and leads to soot's characteristic fractal-like aggregate morphology (Fig. 3).

Fig. 4A presents time resolved measurements of soot formation and growth using the example of a premixed flame. Because the combusting mixture's flow rate remains constant in this type of flame, time can be measured by height above the burner. A growing nucleation mode of incipient soot particles appears at 8 mm. At 10 mm, this is fully formed, and the beginning of an accumulation mode is visible. The particles in this mode increase in size at nearly constant concentration over the next 2 mm in height; thus, this occurs primarily via surface growth. Particle number decreases from 12 to 15 mm as average size increases, indicating that coagulation is starting to play an increasingly important role.

The soot in this ethylene flame remains immature compared to typical engine exhaust soot, meaning that the carbon is not fully sp2 bonded (aromatic or double bonds), but instead retains a non-negligible fraction of hydrogen atoms. One way to measure this is optically; thus, visible light absorption increases as graphitic sp2 bonding increases. This provides a measure of the "black carbon" (BC) content of soot (Arnott et al., 2005; Petzold et al., 2013). Thermal analysis offers another means to determine gross soot composition. This method records organic carbon (OC) from the hydrocarbons evolved after heating the PM sample in the absence of air, and elemental carbon (EC) from the CO_2 evolved from burning the remainder in the presence of oxygen (Fung et al., 2002; Jeong et al., 2004).

Panel B in Fig. 4 shows the growth of black carbon (BC), measured optically, versus total soot mass, recorded by thermal analysis and calculated from the size distributions, as a function of time after start of combustion (height above burner) (Maricq, 2014). The BC to total soot mass ratio increases from ~25 % - 60 % owing to the carbonization that occurs as newly formed soot particles lose hydrogen in the later part of the flame (Dobbins, 2002). These processes of soot growth and carbonization also occur in combustion engines, but with significant differences between diesel, PFI gasoline, and GDI gasoline technologies. In engines, there is also the possibility of soot oxidation if excess O_2 is present in the post flame gas.

Soot control in a premixed flame is in principle simple; maintain an equivalence ratio below the sooting point of the fuel. But this is not possible in most practical flames which are non-premixed, since the fuel / air ratio varies with position across the fuel air mixture, e.g., from rich in the center to lean in the periphery of a diffusion flame. In some cases, such as a diesel engine, this arises from the choice of combustion process. In others it arises from non-idealities in the combustion system, for example incomplete evaporation of fuel droplets or unintended impingement of a fuel spray onto the piston surface. Here strategies for soot mitigation include engineering improvements to reduce the number and equivalence ratio of rich zones where soot forms, e.g., better fuel evaporation, increased air entrainment, or the use of lower sooting fuels, or to increase soot removal by post flame oxidation.

Ash and sulfate in engine exhaust PM arise from metal and other inorganic element-containing molecules that exist as impurities in the fuel and lube oil or are included in fuel and lube oil additives. Unlike soot, these elements remain present in the exhaust gas irrespective of engine operation or combustion conditions. In rich flames, these compounds reactively add to soot particles analogously to the HACA mechanism, or remain as partially oxidized organometallic, organosulfur, etc. species that can subsequently condense onto soot particles or nucleate. Under stoichiometric and lean conditions, these compounds are oxidized and can react with water vapor to produce metal and inorganic oxides, phosphates, sulfates, etc. If these nucleate and then mix with soot, they will collide to produce

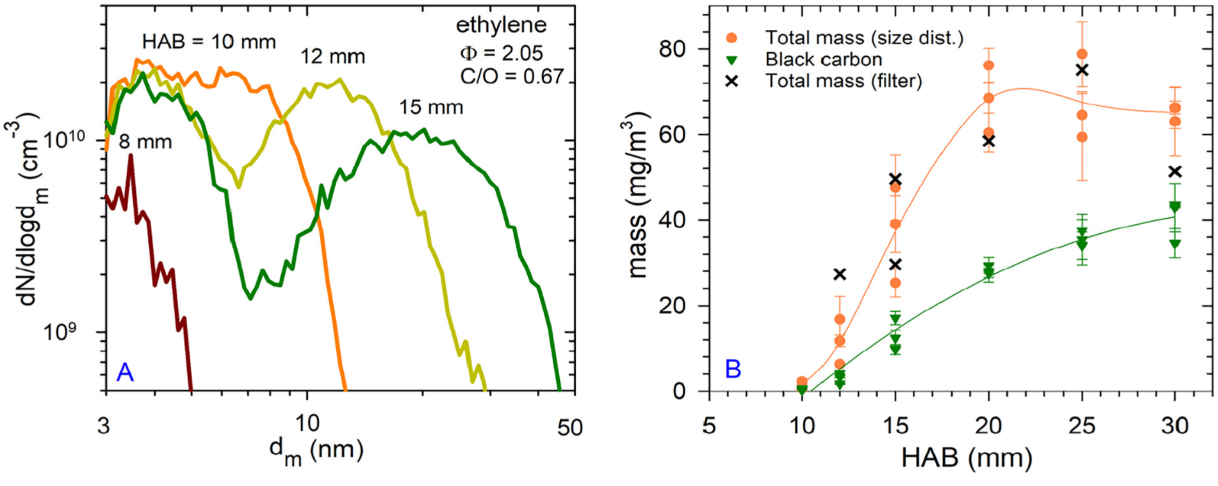

Fig. 4. Evolution of soot characteristics in a premixed ethylene flame (Maricq et al., 2003; Maricq, 2014). Panel A: Soot size distributions (mobility equivalent diameter) versus time (height above the burner). Panel B: Total and black carbon mass versus time.

"decorated" soot aggregates (Jung et al., 2005; Gagné et al., 2021). When soot levels are low or mixing times short, they can remain as a separate nucleation mode. In contrast to soot and HCs, ash and sulfate cannot be chemically converted to CO_2 and water vapor; thus, these species must be trapped, or metal and inorganic content in fuel and lube oil reduced, to limit their contributions to PM emissions.

3. PM formation in engines

Internal combustion engines burn fuel to produce power. The primary combustion products are CO_2 and water vapor, but a large array of other species, including HCs, NO_x, CO, SO_x and soot, are produced depending on engine type, operating condition, and fuel. This section examines soot formation in the three major internal combustion engine technologies used for light duty vehicles. The diesel engine is included to add context for the gasoline engines that are the main subject of the review.

3.1. Particle formation in diesel engines

Diesel combustion by its nature produces soot. There are numerous types of diesel engines, including 4-stroke and 2-stroke, indirect and direct injection, that fulfill applications ranging from portable generators to ships. Here, we consider the high-pressure common rail, direct injection, engine primarily used in modern LD vehicles (Stumpp and Ricco, 1996; Badami et al., 2002; Park et al., 2004). This technology permits multiple fuel injections per engine cycle, which can be used to optimize power, control noise and vibration, and reduce PM emissions.

The seminal study by Dec (1997) gives a detailed explanation of diesel combustion. He employed laser sheet imaging to produce a visual representation of a reacting diesel fuel jet. This technique sends a short, ~10 ns, sheet shaped light pulse, typically 25 mm wide and 0.3 mm thick, into an optically accessible engine cylinder and records any induced fluorescence or scattered light using a gated, intensified, array detector. Light wavelength is selected to probe a specific species, such as soot, OH radicals, PAHs, fuel droplets, etc. (Snelling et al., 1999; Kosaka et al., 2005), and the laser pulse and detector gate are varied with respect to the start of injection to acquire time resolved concentration images. Sweeping the laser sheet across the cylinder then provides a spatial map of the concentration profiles.

Dec (1997) combined images of the liquid fuel spray, evaporated fuel air mixture, laser induced soot incandescence, soot light scattering, and OH radical and PAH fluorescence to develop a comprehensive picture of diesel combustion. This is illustrated by Fig. 5. The top panel shows an instantaneous image of a flame, which exhibits effects of turbulence that contributes to cycle-to-cycle variation. The bottom panel portrays a schematic representation descriptive of a broad time period from injection to the mixing-controlled burn.

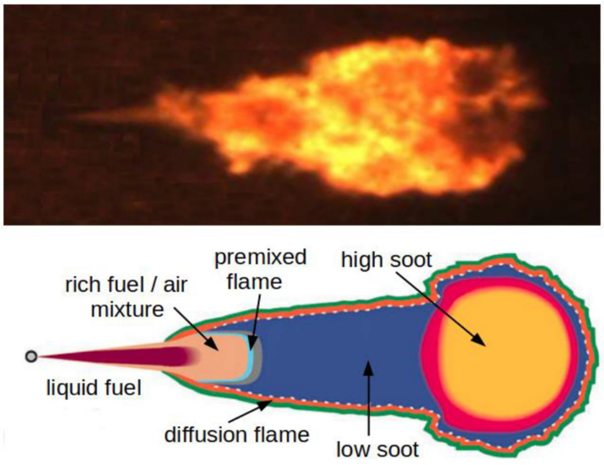

Fig. 5. Diesel combustion. Top: Flame image. Bottom: Schematic representation (Dec, 1997).

Upon injection, the jet of fuel droplets travels across the cylinder entraining air. This causes droplet evaporation and mixing, which produces a rich fuel air mixture with $\Phi = 2–4$ at the leading end of the jet. This mixture auto-ignites into a rich premixed flame that generates incomplete combustion byproducts including soot. The periphery of this partially combusted, but still fuel rich, region develops a diffusion flame, which also produces soot. This, plus the surface growth of soot from the premixed flame, combine to form a high concentration of soot in the leading portion of the flame. During late stages of combustion, the soot region breaks up and is mostly oxidized, >90 %, by the hot excess air in the cylinder (Dec and Kelly-Zion, 2000; Kamimoto et al., 2017). The remainder exits through the exhaust port as soot emissions.

This picture of diesel combustion was a vast improvement over the conventional view at the time; for example, it showed the important role of premixed combustion and demonstrated that soot is formed volumetrically within the jet, and not just at the periphery (Dec, 1997). However, like its predecessor, this conceptual picture retained the view that diesel combustion by its nature produces soot, the only question is how much. Consequently, diesel engine emissions research largely continued to follow a paradigm of comparative studies that mapped soot emissions as a function of engine load, injection strategy, exhaust gas recirculation level, etc., under steady state operating conditions. Aided by the improved understanding of the combustion process, strategies such as higher injection pressure (Pickett and Siebers, 2004), longer lift-off length (Siebers and Higgins, 2001), post injection (O'Connor and Musculus, 2014) and other advanced compression ignition concepts (Dec, 2009), were identified and studied for their potential to help meet the tight emissions standards imposed by the US EPA 2007 HD PM mass and EU solid particle emissions regulations.

In the end they proved insufficient to meet these standards, at least partly due to other constraints such as NO_x emissions, fuel economy, and driveability; thus, DPFs were adopted to satisfy the US EPA and EU requirements. These proved very effective, typically reducing PM emissions, mass and solid number, by 99 % or more, but they added cost and complexity owing to the need to periodically regenerate them from the captured soot (Khalek et al., 2011). Post 2007 HD exhaust aftertreatment also incorporates a diesel oxidation catalyst (DOC) that reduces HC emissions by >90 %. Since this includes SOA precursors, smog chamber measurements found that these engine / DOC / DPF systems led to near negligible SOA formation (Gordon et al., 2014a) and, thus, a very low atmospheric PM burden.

3.2. Particle emissions from PFI engines

Combustion in PFI gasoline engines stands in stark contrast with diesel combustion (Heywood, 2018). The underlying condition for soot formation remains the same, rich fuel air events, but these are the exception and not the rule. While there are variations, the standard process for combustion in PFI engines begins with fuel injection onto a closed intake valve. Heat from the valve evaporates the fuel. When the valve opens during the intake stroke, the piston draws air and fuel vapor into the cylinder, with the air intake throttled to allow in only enough air for a stoichiometric fuel / air ratio. Fluid motion during the intake and compression strokes mixes the fuel and air so that the spark ignites a homogeneous stoichiometric mixture that in principle produces no soot.

While gasoline engines are not zero PM emitters, they have come close to this ideal for some time. Fig. 6 compares PM emissions reported in two light duty PFI gasoline vehicle studies to those from pre-DPF equipped diesel vehicles. It is immediately evident that the PFI vehicle emissions are circa 50 times lower whether measured by mass or total particle number (solid plus semi-volatile). The test vehicles range in model year from 1994 to 2008. All of the PFI vehicles emitted an FTP weighted average PM mass emissions below 2 mg/mi. Except for four vehicles in the

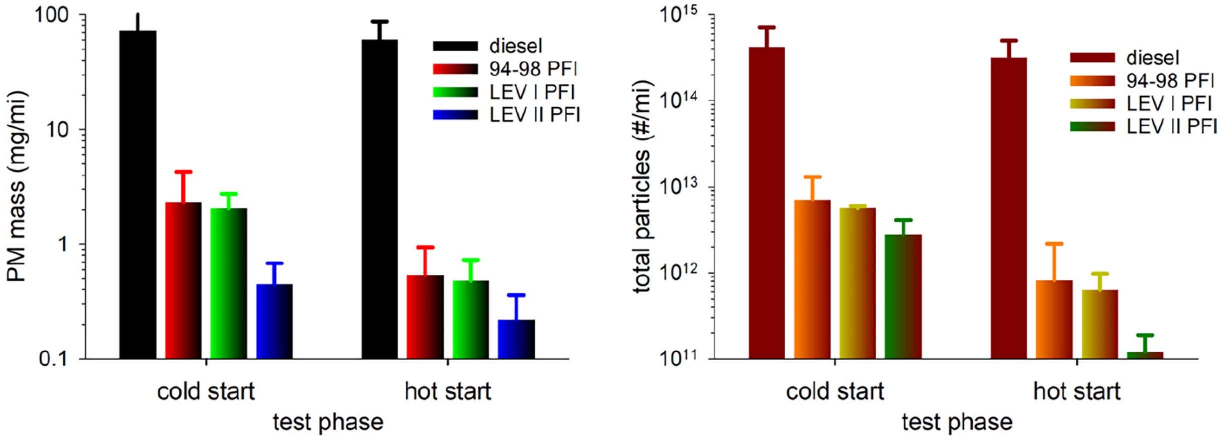

Fig. 6. PFI gasoline versus diesel vehicle particulate emissions over the cold and hot start phases of the FTP drive cycle. Left panel: PM mass. Right panel: Total number. Diesel data: average of three Euro 3 passenger cars (Maricq unpublished), 94–98 PFI data: average of sixteen 1994–1998 LD vehicles (Maricq et al., 1999b). LEV I and II data: average of three 2000–2002 and five 2005–2007 LD vehicles (Zhang et al., 2010). Error bars represent 1 σ of the test population.

1994–1998 range, they achieved emissions below the upcoming 2025 CARB 1 mg/mi standard.

Closer examination of Fig. 6 reveals two other observations worth noting. The first relates to the importance of the cold start. Diesel emissions, both mass and number, show little difference between the cold and hot start phases of the FTP cycle. In contrast, the PFI vehicles emit roughly five times less PM mass and particle number during the hot start; thus, unlike diesel engines, where instantaneous operating conditions dictate PM emissions, those from PFI vehicles depend on engine history. The second observation relates to improvement in PFI PM emissions over time. There is a significant, approximately four-fold drop in PM mass and two-fold drop in particle number emissions between LEV I and LEV II. This has been observed in other gasoline vehicle PM emissions studies as well (Robert et al., 2007) and is likely a benefit of improvements in fuel / air ratio control and three-way catalyst efficiency that were among the technological advances made by OEMs to meet the increased stringencies in non-methane hydrocarbon (NMHC) and NO_x emissions imposed by LEV II (Section 5.2).

There is a caveat; the data in Fig. 6 exemplify the potential for PFI gasoline vehicles to meet very stringent PM emissions standards, but do not represent the real-world emissions by these vehicles. The latter can differ from the results of regulatory lab tests for several reasons. One is that the FTP cycle is not especially representative of real-world driving; thus, U.S. regulations have added the US06 and SC03 cycles for aggressive driving and air conditioner use, respectively, and the EU has switched to the Worldwide harmonized Light vehicles Test Cycle (WLTC) (Samuel et al., 2002; Tutuianu et al., 2015). Environmental factors play a role; thus, cold ambient temperatures exacerbate PM emissions, as demonstrated for example by the Kansas City study (Fulper et al., 2010). Vehicle deterioration and lack of maintenance also play important roles in real-world emissions. Still, studies of in-use vehicles have shown that gasoline vehicle PM emissions have improved as new models are introduced to meet more stringent regulations (Robert et al., 2007; Fulper et al., 2010). Half of the 1996–2004 model year cars in the Kansas City study had emissions below 2 mg/mi and half of the LD trucks had emissions below 4 mg/mi when tested on the LA92 drive cycle, which is more aggressive than the FTP test (Fulper et al., 2010). Thus, a good fraction of vehicles in the real-world fleet for these model years had emissions comparable to those in Fig. 6.

Since the conceptual picture of gasoline combustion in a PFI spark ignition engine is one of no soot formation, how does it originate in real engines? The presence of fugitive hydrocarbons, those from fuel and lube oil that escape combustion, is one principal culprit. A study by Kayes and Hochgreb (1999) revealed a strong rise in PM emissions upon either an increase or decrease in equivalence ratio from stoichiometry, as shown in Fig. 7. Increased soot formation at higher Φ is expected, owing to rich combustion, as described in Section 2.2. A rise in soot under lean conditions is harder to explain, since one expects little carbon to escape oxidation and, hence, little available to produce soot. If, however, fugitive HCs are present after the end of combustion, such as unburned fuel in crevice volumes, or a lube oil / fuel film on the cylinder walls, the excess oxygen remaining after lean combustion can ignite these at the high post-flame in-cylinder temperature. As such regions are locally rich, they can produce soot.

Liquid fuel entering the engine cylinder presents another pathway for soot formation. Ideally all of the fuel evaporates in the intake manifold and begins to mix with the intake air prior to being drawn in by the piston. In practice, Meyer et al. (1998) identified several mechanisms that can transport liquid fuel into the engine, including direct penetration of fuel droplets if valve opening overlaps fuel injection, intake air atomization of liquid fuel remaining on the closed valve as it opens, and droplets formed by squeezing of liquid fuel remaining on the valve as it closes. Inadequate evaporation and mixing of these droplets produce locally rich zones capable of producing soot.

How these mechanisms contribute to soot formation depends on numerous engine operating conditions, including temperature, speed, load, EGR, and fuel injection and spark timing, which are discussed in Section 4 (Kayes and Hochgreb, 1999). In some cases, their impact is clear; for example, increased engine temperature reduces soot by promoting fuel evaporation. In others it is more complex; an increase in load requires more fuel, but it generates additional heat. Such conflicting impacts contribute to the engine

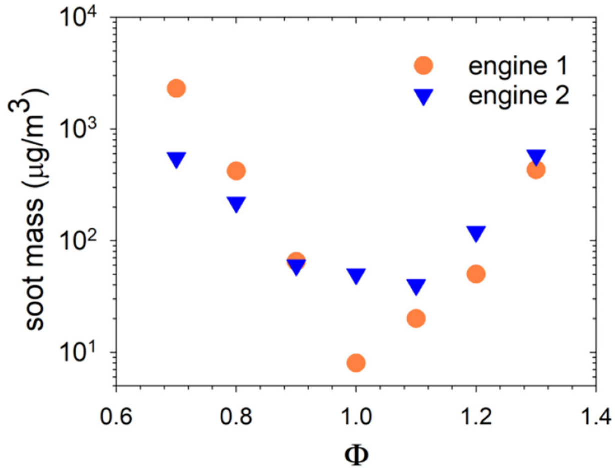

Fig. 7. Effect of fuel air ratio on PFI gasoline engine PM mass (Kayes and Hochgreb, 1999).

history dependence of PFI engine soot emissions. Under steady state operation one can map out competing effects, in this example to see if the higher evaporation rate from the added heat is sufficient to vaporize the larger quantity of fuel injected. But in real world transient driving, higher load usually occurs during vehicle acceleration, at the start of which the intake manifold is cooler than during the steady state condition at the same load. Thus, soot formation during a transient is presumably higher than, and not predictable from, the steady state engine PM emissions data.

Although they both originate from fuel, PM and HCs are generally found to be poorly correlated (Kayes and Hochgreb, 1999; Mazzoleni et al., 2004). One key reason is that PM consists of partially combusted fuel, whereas both partially burned, and fugitive fuel and oil contribute to HC emissions. The gasoline engine soot formation mechanisms described above, however, are also pathways for HC emissions (Cheng et al., 1993). Thus, engine improvements to mitigate HC emissions also reduce PM, even if the reductions are poorly correlated quantitatively, and have contributed to the improvements in PFI gasoline vehicle PM emissions over time.

Whereas black / elemental carbon is the main component of engine-out diesel exhaust PM, the situation is more variable for PFI gasoline vehicles. Laboratory and on-road measurements reveal considerable variation in EC/OC emissions depending on vehicle age, aftertreatment technology (Section 5), drive cycle, ambient temperature, fuel (Section 6), and other factors (Robert et al., 2007; Liggio et al., 2012; Forestieri et al., 2013; Chan et al., 2014). Vehicles with worn engines, malfunctioning fuel air ratio control, or older three-way catalysts tend to emit PM with low EC/OC ratios owing to high HC emissions and low catalyst efficiency. Cold starts, cold temperature operation, and low volatility / high aromaticity fuels lead to higher EC/OC ratios due to increased soot formation by the engine in these situations. However, the EC fraction of PM emissions from properly functioning LEV I / Tier 1 and LEV II / Tier 2 PFI vehicles tested over laboratory drive cycles has remained relatively high at roughly 75 % even as total PM mass levels have fallen to below 3 mg/mi (Forestieri et al., 2013). In essence, reductions in engine soot formation have been matched by declines in HC emissions.

3.3. Particle formation in GDI engines

Gasoline direct injection, also known as direct injection spark ignition (DISI), is a combustion technology that offers several opportunities to improve gasoline engine efficiency and, thereby, increase fuel economy and lower CO_2 emissions (Karl et al., 1997; Alkidas and El Tahry, 2003). Fig. 8 shows a cut-away view of a GDI engine cylinder with a side mounted fuel injector. The other major geometry features a centrally mounted fuel injector. Evaporative cooling by the intake fuel air charge increases the amount of fuel that can be injected relative to the same size PFI engine. The cooling reduces knock, which allows a higher compression ratio that further helps raise engine efficiency. Direct fuel injection improves control of the amount of fuel that enters the combustion chamber. This is especially important during a cold start when a substantial fraction of port injected fuel stays unevaporated in the intake manifold. Furthermore, it enables control of when during the engine cycle fuel enters the chamber, which opens the possibilities of lean stratified combustion and split injection.

Fig. 8. Cut-away view of side mounted gasoline direct injection engine.

The GDI concept has evolved over time as efforts have been made to simultaneously meet fuel efficiency and tightening restrictions on HC, NOx and PM emissions. Modern era GDI vehicles were first introduced by Mitsubishi in 1996 (Ashley, 1996). A key feature of these engines was the use of stratified combustion to reduce the pumping losses that exist when running a stoichiometric gasoline engine at low load (Bishop and Simko, 1968; Alkidas, 2007).

To maintain stoichiometry at low load, a PFI engine must throttle the air intake and allow in only the amount needed for complete combustion. Throttling requires the engine to perform work to aspirate air, which reduces engine efficiency. Direct injection - stratified combustion offers a means to avoid this pumping loss. The idea is to replace the throttled homogeneous fuel air mixture with a stratified mixture that is inhomogeneous but has a combustible local equivalence ratio at the spark plug (Bishop and Simko, 1968; Iwamoto et al., 1997). Fig. 9 schematically illustrates the principal strategies to achieve the necessary stratified fuel air mixture. In panel A, the injector is mounted centrally with a closely spaced spark plug, and the spray geometry is used to constrain fuel air mixing prior to ignition. In panel B, the injector is side mounted and widely spaced from the spark plug. The fuel is injected towards a shaped piston bowl and the momentum of the spray combined with the tumble of the air motion produces a locally combustible mixture at the spark plug (Fan et al., 1999). These strategies are often referred to as “spray guided” and “wall guided / air guided”, respectively. However, this is an oversimplification since these mechanisms do not apply uniquely to either GDI geometry.

In practice, vehicles such as the 1996 Mitsubishi GDI ran mixed mode. They used stratified combustion at low load to avoid pumping losses, but switched to homogeneous combustion, with fuel injected during the intake stroke, at high load. The reduced pumping losses from stratified combustion provide about a 10 % efficiency benefit (Alkidas and El Tahry, 2003; Alkidas, 2007), but at the price of higher PM emissions (Maricq et al., 1999a; Zhang and McMahon, 2012). As Fig. 10 illustrates, both PM mass and total particle number exhaust concentrations increase by more than an order of magnitude as fuel is injected later in the compression stroke. The non-monotonic behavior, which has also been observed in other studies (Park et al., 2012; Ketterer and Cheng, 2014), suggests that PM formation is a complex function of injection timing under stratified combustion.

One reason for an increase in PM emissions with late fuel injection is the short time available for mixture preparation. Thus, there is less time for fuel droplet evaporation and, consequently, a higher propensity to form soot. The main reason, however, is fuel impingement onto the piston surface and cylinder walls, which is observed in engines with both side and centrally mounted injectors (Stevens and Steeper, 2001; Drake et al., 2003; Velji et al., 2010; Dahlander and Hemdal, 2015; Miyashita et al., 2016). The images in Fig. 11 illustrate this process. The top panel shows the fuel

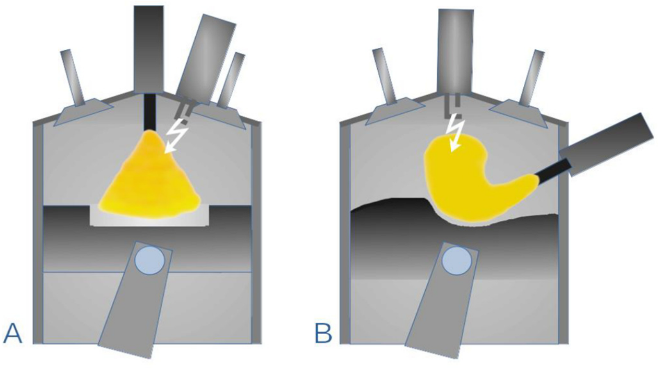

Fig. 9. A) Centrally mounted and B) side mounted injector configurations of a GDI engine.

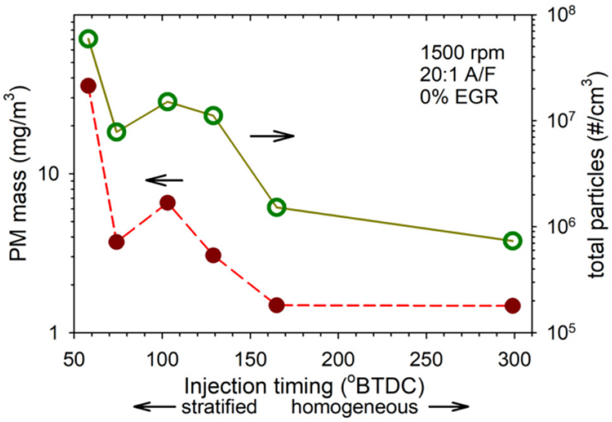

Fig. 10. PM mass and total number concentrations in the exhaust of a GDI engine as a function of injection timing (Maricq et al., 1999a).

spray into the cylinder and the bottom panel shows the incandescence from the soot produced above the piston surface. This mechanism has been referred to as "pool fires", but the study by Ketterer and Cheng (2014) attributes the soot formation instead to pyrolysis. They found that soot is produced after the flame passes; thus, it is not by combustion since very little oxygen remains available. Laser induced fluorescence (LIF) measurements show a decrease in OH radicals as injection is retarded; thus, a lower soot oxidation rate also contributes to the increase in soot with late injection (Hemdal et al., 2011).

Soot formation from fuel impingement can occur with both side and centrally mounted injection but is more commonly associated with the former. Late injection limits the time available for mixture preparation to optimize combustion. Deflection of the fuel spray by the piston in the wall guided approach increases the time it takes fuel to reach the spark plug, and the tumble motion enhances fuel air mixing relative to the spray guided method with its closely spaced spark plug (Iwamoto et al., 1997). Thus, early commercial stratified combustion GDI engines largely adopted the side mounted, wall guided, approach. These vehicles met CARB and EPA PM emissions standards of the time, but with significantly higher rates than their overachieving PFI counterparts. With more stringent regulations on the horizon, GDI technology evolved towards homogeneous operation. This mode has the additional advantage that meeting NOx emissions was possible with existing three-way catalyst technology, whereas the globally lean nature of stratified combustion required development of new aftertreatment approaches, such as lean NOx traps and selective catalytic reduction (Pauly et al., 2010; Kim et al., 2011).

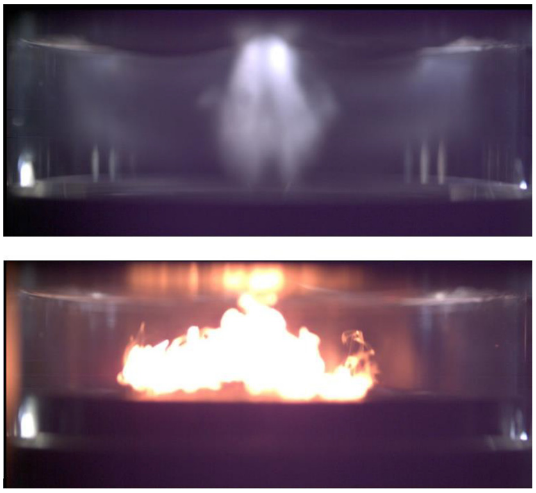

Fig. 11. PM formation in a GDI engine. Top panel: fuel spray into the cylinder from a side mounted injector. Bottom panel: soot formation from a rich "pool fire". (Courtesy of S. Wooldridge, Ford Motor Co.)

Current GDI engines utilize both wall and spray guided fuel injection. Homogeneous operation relies on early fuel injection, ordinarily during the intake stroke, to provide sufficient time and on the intake air turbulence to provide sufficient charge motion for complete fuel air mixing prior to spark ignition. Impingement remains a pathway for soot formation; if injection begins too early, fuel droplets can impact the piston before it has moved beyond the penetration length of the fuel spray. In this case, soot may result less from liquid films on the piston, which can evaporate prior to ignition, and more from films on the valves that arise as fuel droplets bounce from the piston (Ketterer and Cheng, 2014).

Injector nozzle wetting presents another path for soot formation. Just as with fuel films on the piston and cylinder walls, rich combustion, or pyrolysis of a fuel film on the injector tip leads to soot formation as evidenced by observations of injector tip flames (Piock et al., 2015; Imaoka et al., 2019). With nozzle wetting, however, the main strategies used to reduce piston and cylinder wall films, namely injection timing, spray penetration, and droplet size optimization, do not work. Instead, it is important to examine the mechanisms of tip wetting and understand how injector design and operation can be improved to reduce tip wetting.

The fuel injector's impact on GDI engine PM emissions is complex. It can be divided into three regimes. First, a variety of mechanisms, such as needle bounce (Section 4.2), and flash boiling (Sections 4 and 6.4) deposit liquid fuel films on the injector tip (Medina et al., 2021a). This film can then evaporate and burn as a diffusion flame during the combustion stroke, or pyrolyze after the flame front passes. Second, combustion and pyrolysis of the fuel film leads to tip deposits (Xu et al., 2015; Edney et al., 2020a). These can absorb fuel and increase the film volume on the injector tip, which leads to an increase in PM emissions with engine operation. Finally, sufficiently large injector deposits alter the spray pattern and droplet penetration, which can exacerbate fuel impingement onto the piston and cylinder walls (Jiang et al., 2017; Pilbeam et al., 2020).

The conceptual model of Medina et al. (2021a) divides tip wetting into three phases: during injection, at the end of injection, and late cycle dribbling from the sac volume. Wetting during injection occurs in two ways. The first is from fuel contact with the nozzle wall and subsequent flow around the edge and onto the tip. As observed via X-ray phase-contrast imaging and laser induced fluorescence imaging, flash boiling increases the width of the spray plume and, thus, exacerbates wetting (Leick et al., 2018; Huang et al., 2021; Yao et al., 2021). Second, vortices develop from the expanding fuel jet and accompanying air entrainment, which allow some droplets to escape the bulk flow and land on the injector tip (Medina et al., 2021a). Wetting at the end of injection occurs from ligaments and large droplets that form as the needle closes and then attach to the injector tip as fuel pressure and flow rate decrease. Needle bounce, where the injector briefly re-opens from mechanical rebound during closing, causes additional fuel dribble that comprises an important source of wetting (Huang et al., 2020). Finally, residual fuel in the sac can escape and condense onto the injector tip.

Injectors are prone to internal and external deposits over time as heat and reactive combustion products degrade fuel components (Xu et al., 2015). Owing to their porous nature, tip deposits can increase wetting by absorbing fuel and, thereby, increase PM emissions. Fig. 12 depicts the rise in exhaust particle number concentration that occurs over 13 h of tip deposit accumulation. Similar behavior, sometimes denoted PN drift, has been observed in various other studies (Henkel et al., 2017; Barker et al., 2019; Imaoka et al., 2019). In general, there is an induction phase before PM emissions begin to rise. Emissions then increase relatively rapidly and level off to a steady state plateau as the deposit develops a more complex layered structure. As examined in Section 4.3, the time span for deposit formation and the extent to which this increases PM emissions varies depending on engine operating conditions, fuel composition, and presence of fuel additives.

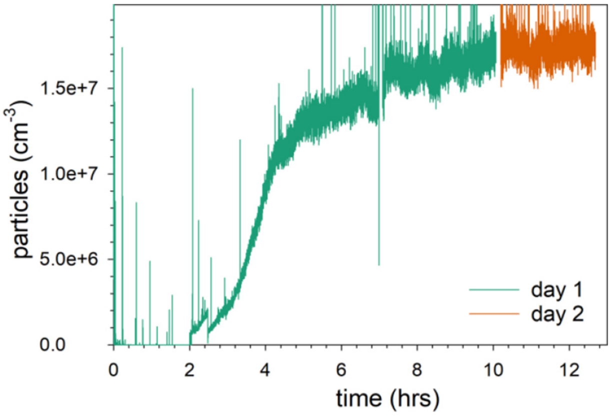

Fig. 12. PN emissions versus time after installation of clean injectors in a GDI engine. The test occurred over two days with a pause in between: green = day 1 and orange = day 2. (Data courtesy of T Han and A Boehman, University of Michigan). (For interpretation of the references to colour in this figure legend, the reader is referred to the web version of this article.)

3.4. Gasoline engine PM characteristics

Piston and cylinder wall impingement, injector wetting, and poor mixture preparation, are the primary PM formation pathways for GDI engines. Those identified previously for PFI gasoline engines, namely crevice volumes, unburned hydrocarbons in the quench layer, and the lube oil and dissolved hydrocarbon film on the cylinder walls, also play a role, especially under conditions where the primary pathways produce little PM. All of these pathways involve rich combustion or pyrolysis of hydrocarbons, so soot is expected to be the major PM component. Indeed, this is generally the case. Tailpipe EC/OC and BC measurements of GDI vehicle exhaust generally reveal that roughly 80–90 % is elemental or black carbon over the FTP drive cycle (Chan et al., 2017; Chang and Shields, 2017; Maricq et al., 2017). These particles mostly exhibit a typical soot-like morphology (Barone et al., 2012; Seong et al., 2014), as illustrated in Fig. 13.

However, there is a substantial variability in the composition and morphology of GDI vehicle exhaust PM owing to the wide range of engine operating conditions and fuel compositions (Section 6), as well as the presence of lack of aftertreatment (Karjalainen et al., 2014). For example, in their examination of injection timing impact on PM emissions, Barone et al. (2012) observed small solid spherical particles and liquid droplets in addition to the more prevalent soot aggregates. When they delayed injection from 320 to 280 degrees before top dead center (°BTDC) to reduce piston fuel impingement and lower emissions the fraction of droplets decreased from 25 to 1 %, while single solid spheres increased from 8 to 21 %. The droplets were, therefore, proposed to originate from oil washed from the piston top by the impinging fuel spray.

Another study, which compared stratified to homogeneous operation at 2000 rpm and 2 bar BMEP, found that particle composition changed from 90 % EC & PAHs in the stratified mode to 65 % EC & PAHs and 25 % ash for homogeneous stoichiometric operation, as PM mass decreased by about two orders of magnitude (Zelenyuk et al., 2017). At 1000 rpm and 1 bar BMEP the EC / ash ratio exhibited an even steeper decline, but particle number increased due to the appearance of a ~ 20 nm size mode attributed to ash particles. This likely occurred as ash nucleated in lieu of condensing onto the small number of soot particles.

As a final example, consider the differences between GDI vehicle PM emissions during the FTP and US06 drive cycles. The aforementioned 80–90 % soot fraction observed for the FTP cycle falls to about 40–70 % on the US06 cycle (Chan et al., 2017, Chang and Shields, 2017, Maricq et al., 2017). Furthermore, the BC/EC ratio decreases from near unity for the FTP cycle to 40–90 % for the US06, which indicates that the soot is less black, that is less mature, under aggressive driving. This likely originates from high temperatures and shorter combustion cycle times associated with high speed / load operation, but the specific engine conditions causing these changes are not known.

Particle size distributions also vary with GDI engine operation (Peckham et al., 2011; Zhang and McMahon, 2012; Hu et al., 2021). This

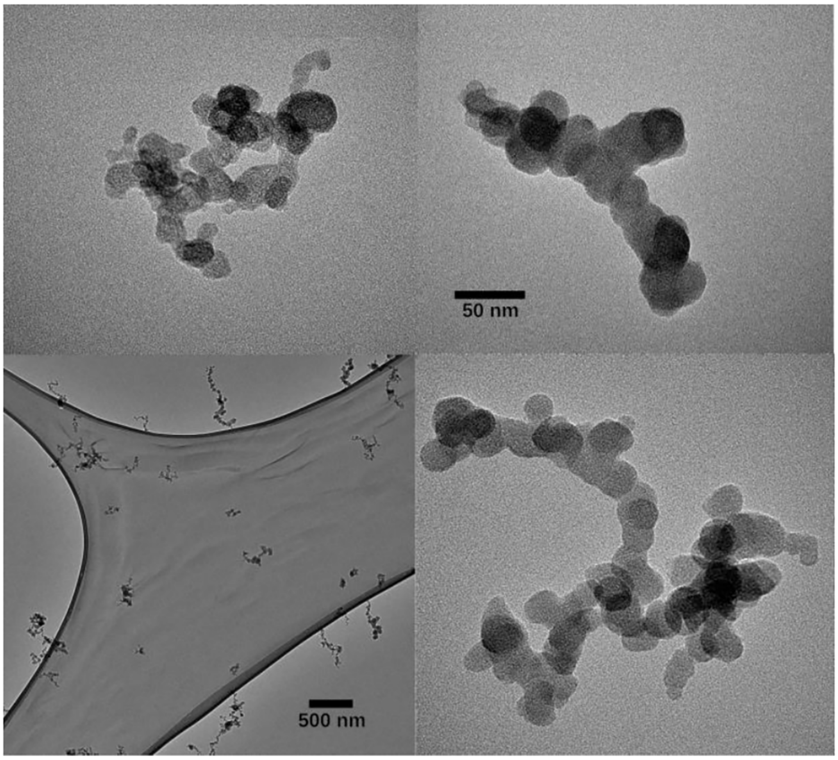

Fig. 13. TEM images of tailpipe PM sampled from a 2.0 L GTDI vehicle (side mounted injectors) over the FTP drive cycle (Maricq unpublished).

is nicely demonstrated by observing the changes in particle size over the FTP + US06 drive cycle. As seen in Fig. 14, the size distribution is unimodal over most of this test. Emissions are relatively high and mean size varies between about 50 and 100 nm early in the cold start as the engine strategy is varied to achieve engine start and catalyst light-off. The emissions rate falls substantially part way through the cold start phase and remains low for the remainder of the FTP cycle. The size distribution broadens, but the peak remains in the 50–100 nm range.

Things change considerably during the US06 portion. At first, emissions increase, but remain unimodal. During the high-speed portion of the US06 cycle a second mode appears at about 10 nm. This coincides with a rise in exhaust temperature, which can reach above 800 °C over this portion of the drive; thus, it is not certain if these particles originate from the engine or from thermal release of material elsewhere in the aftertreatment and exhaust system. The details of the size distribution history in Fig. 14 are specific to the test vehicle used, but the general features of a soot accumulation mode early in the cold start, low emissions during the urban and hot start, followed by an increase in accumulation mode and possible appearance of a strong nucleation mode during the US06, have been observed for many vehicles and tests (Maricq et al., 2017).

The large variability in composition, morphology, and size distribution of GDI vehicle PM emissions is not surprising, since total PM mass can vary from near non DPF diesel emission levels to almost zero. Deviations from soot dominated emissions generally occur at low PM levels under conditions, for example, where ash and/or semi-volatile hydrocarbons nucleate for lack of sufficient surface area on which to condense. At low levels, the presence or lack of a three-way catalyst can also have a large impact on the nature of the PM that is measured. An engine may emit a semi-volatile nucleation mode or an accumulation mode with a high OC/EC ratio without a three-way catalyst, but instead emit no nucleation mode and low OC/EC soot mode when equipped with a catalyst that substantially removes semi-volatile HCs from the exhaust.

3.5. Summary of gasoline engine PM formation

Gasoline vehicle tailpipe PM emissions originate from incomplete combustion and fugitive fuel and lube oil. Under ideal circumstances, gasoline vehicles should not emit PM, namely when: 1) the fuel contains only carbon, hydrogen, and oxygen, 2) the fuel air mixture is stoichiometric and homogeneous, 3) there is no oil leakage into the engine cylinder, and 4) the three-way catalyst is 100 % effective. Under these conditions, soot is not produced, and no semi-volatile HC, ash, or sulfate precursors are present to form PM.

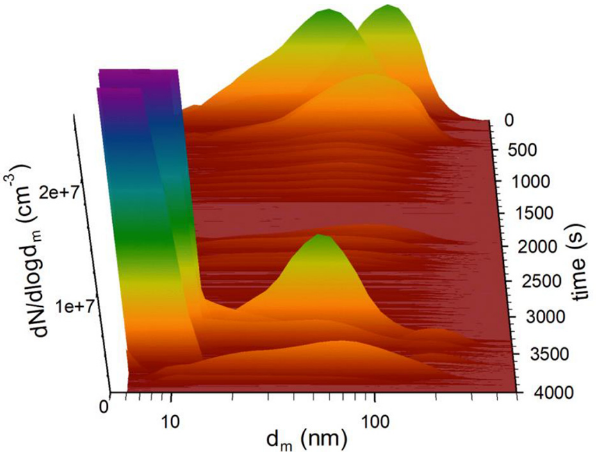

Fig. 14. Tailpipe particle size distributions for a 2.0 L wall guided GTDI vehicle run over the four phase FTP + US06 drive cycle. Measurements from a dilution tunnel are made by an Engine Exhaust Particle Sizer (Maricq unpublished). Analysis uses the soot inversion algorithm (Wang et al., 2016).

In practice, several pathways exist to form PM, either directly in the engine, or indirectly as the exhaust enters the atmosphere. Fig. 15 summarizes the principal sources and pathways for the four major gasoline PM components. The strategies for reducing gasoline vehicle PM emissions depend on component and source. Fuel and fuel additive derived sulfate and ash are produced directly from combustion and negligibly by the soot formation pathways. Thus, their reduction requires removing sulfur, metal, and inorganic containing compounds from the fuel and additives, increasing fuel economy, or adding a sulfur / ash trap to the exhaust system. Lube oil and lube additive derived sulfate and ash can be reduced by removing their precursors or by restricting oil incursion into the engine cylinder via the pathways in Fig. 15. Aside from reducing sulfate and ash emissions, these actions also reduce catalyst poisoning and, thereby, aftertreatment cost.

Soot and semi-volatile organics derive from the hydrocarbons in fuel and lube oil. Since hydrocarbons are essential to both fuel and lube oil, soot and semi-volatile organic PM components cannot be reduced at the source. Instead, they must be controlled by restricting the pathways for their formation, introducing exhaust filters, and formulating lower sooting fuels. The following three sections examine each of these in detail.

4. Gasoline engine technology advances to reduce PM

The major sources of PFI gasoline vehicle tailpipe PM emissions are the presence of HCs in crevice volumes or as liquid films on intake ports and cylinder walls. Gasoline direct injection introduces two additional pathways, namely fuel spray impingement onto the piston and cylinder walls and injector tip wetting. Here we examine these pathways and the means to control them in detail. The emphasis is on GDI vehicles due to their importance for fuel economy and the regulatory concerns over their PM emissions.

4.1. Fuel films from spray impingement

Ideally, direct injection produces an atomized spray of fuel droplets that entrains air and evaporates into a homogeneous stoichiometric fuel air mixture. Droplets that penetrate too far before evaporating impact the piston where a fraction remains as liquid fuel and the remainder bounces onto the cylinder head. The resultant fuel films depend on spray penetration length, distance from injector tip to the piston and walls, and the fuel evaporation rate from these surfaces (Jiao and Reitz, 2015).

These quantities are functions of key engine operating conditions, namely a) injection timing, b) pressure (fuel and cylinder), c) temperature (fuel, piston, and wall), d) injector nozzle design, and e) the number of injections. Fuel injection timing is the dominant factor, which can impact PM emissions by over an order of magnitude (Szybist et al., 2011; He et al., 2012; Oh and Cheng, 2017). It directly controls the distance between injector tip and piston but is not the sole factor in liquid fuel impingement. Intake air motion and time also play critical roles in fuel evaporation and fuel air mixing. Charge air motion is strongest during the intake stroke; thus, advancing the start of injection (SOI) increases the strength and lengthens mixing time prior to ignition (Song and Park, 2015). The trade-off between piston distance and effective fuel air mixing leads to an optimum SOI window, as illustrated by Fig. 16.

These steady state measurements reveal a minimum in PN number, as well as PM mass, emissions in the region of 230–290 ^{o}BTDC of compression. Model calculations by Jiao and Reitz (2015) reproduce the experimental data and reveal a correlation between PM emissions and the amount of liquid fuel that remains on the piston and wall surfaces at the time of spark. Fast thermocouple measurements of piston top temperature show a temperature drop from liquid fuel impingement that decreases with SOI retard (Köpple et al., 2014), providing further evidence for the relationship between SOI, fuel film, and PM emissions. The PM dependence on SOI shown in Fig. 16 holds also for transient and cold start operation, although the specifics vary.

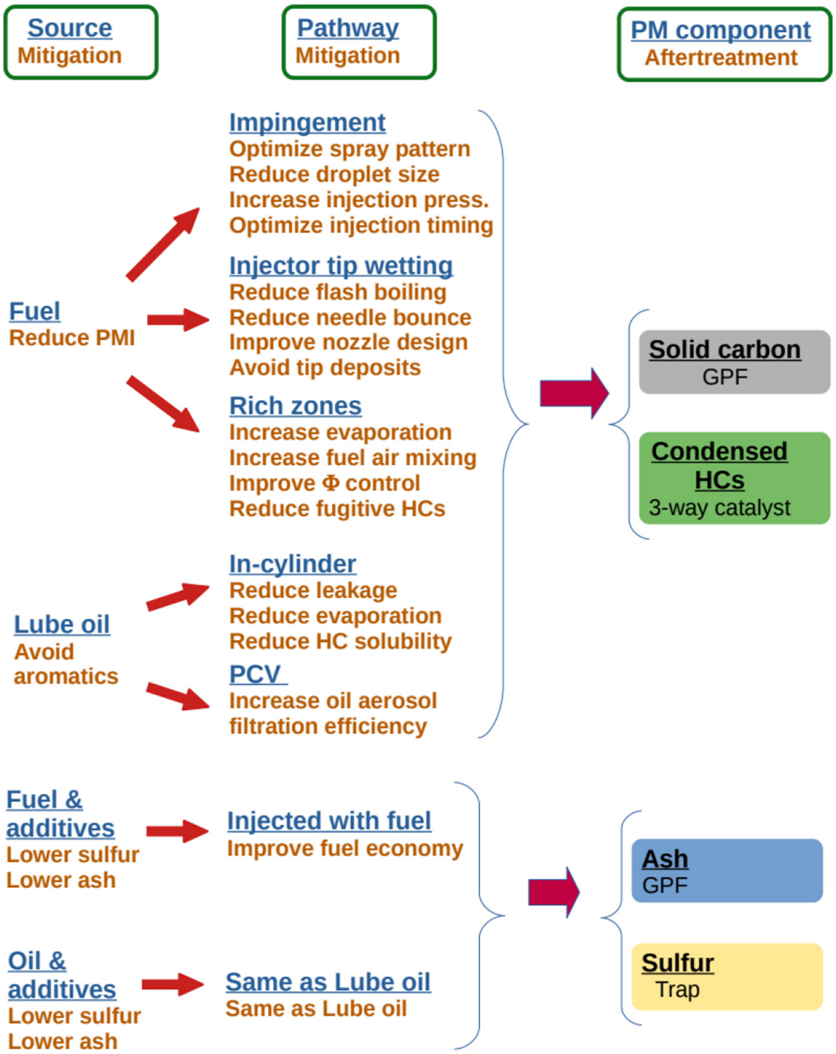

Fig. 15. Gasoline vehicle PM emissions sources, pathways, and mitigation opportunities.

Optimizing fuel system and injector design is critical to reduce fuel films and, thereby, PM emissions (Frottier et al., 2014; Hoffmann et al., 2014). Whereas SOI impacts PM emissions via charge motion, time to spark and distance to piston, the fuel injector controls the spray pattern, fuel droplet size, and liquid penetration length. Pressure and temperature play important roles in these spray characteristics. Engine exhaust data, such as those in Fig. 17, demonstrate how increasing fuel injection pressure reduces PM emissions (Piock et al., 2015; Song et al., 2018). Panel A further shows that enhanced intake air tumble can improve PM emissions and at least partially compensate for the retarded injection timing and, therefore, the reduced mixing time relative to port injection. In panel B, the increase in coolant temperature improves fuel evaporation, which reduces PN emissions. An additional benefit observed from higher injection pressure is a broadening of the optimum fuel injection timing window (Hoffmann et al., 2014).

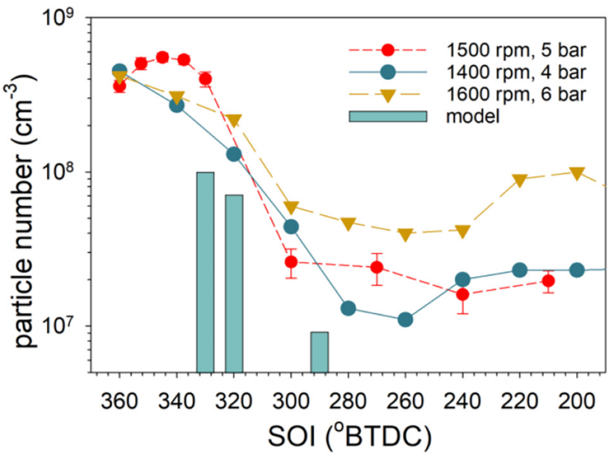

Fig. 16. Particle number concentration dependence on injection timing. 1500 rpm data: Song et al. (2018). 1400 and 1600 rpm data: Oh and Cheng (2017). Model soot predictions from Jiao and Reitz (2015) are scaled to relative PN concentration.

At first glance raising injection pressure might seem to exacerbate soot formation. As fuel pressure increases, so does spray velocity, as seen in Fig. 18. The data show that spray velocity varies with injector design and chamber (engine cylinder) pressure; but the trends with injection pressure follow power law functions close to the Bernoulli square root dependence. Findings that the nozzle flow is multi-phase, with vapor already present in the nozzle, may explain the deviations from incompressible flow (Bornschlegel et al., 2018). Since an increase in velocity shortens the time for the fuel to reach the piston, there must be other important benefits from high pressure injection that lower liquid penetration and, consequently, fuel impingement.

A higher spray velocity increases the aerodynamic forces on the liquid stream, which shortens the breakup time to form droplets (Yamaguchi et al., 2019). Fig. 19 displays breakup time curves from two studies for

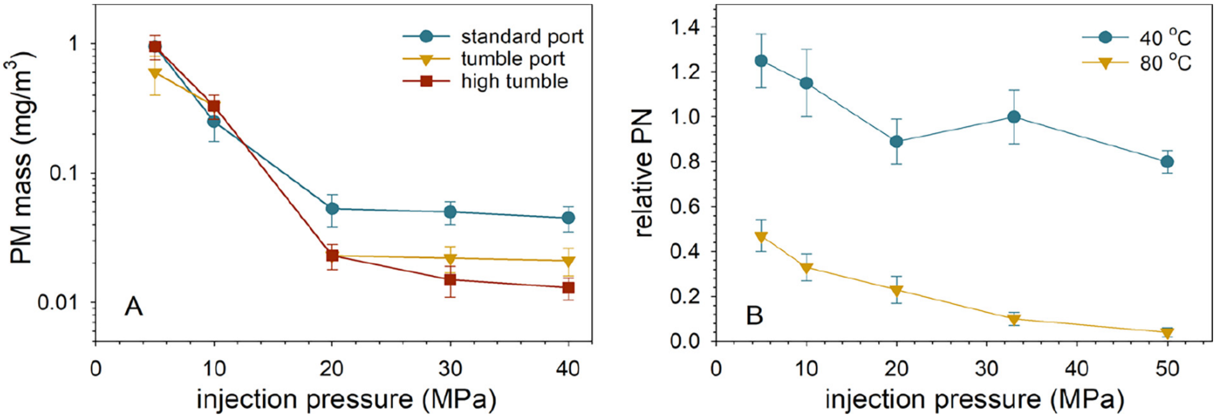

Fig. 17. Dependence of PM emissions on injection pressure, air motion, and temperature. Panel A: PM mass versus injection pressure at tumble numbers of 0.7, 1, & 2 (Piock et al., 2015). Panel B: Relative particle number emissions versus injection pressure at two engine coolant temperatures (Song et al., 2018).

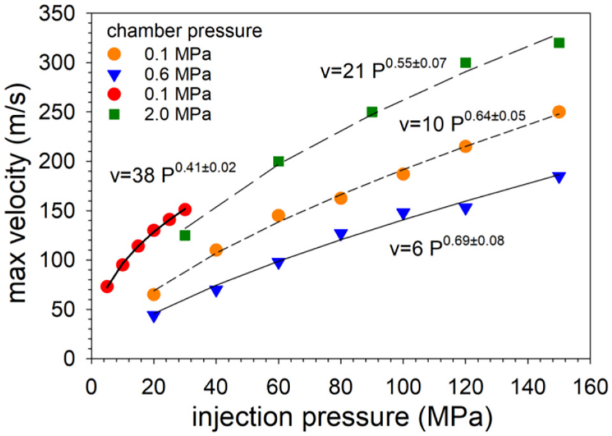

Fig. 18. Spray velocity versus injection pressure. Lines show power law fits. First and second data sets from Yamaguchi et al. (2019), third from Song and Park (2015), and fourth from Medina et al. (2018).

injection pressures up to 150 MPa. Panel A presents data reported by Medina et al. (2018) from a single nozzle injector with a nozzle length to diameter ratio of L/D = 8.2. Panel B shows measurements by Yamaguchi et al. (2019) from a 6-hole diverging nozzle injector with L/D = 5.5. Both reveal a decrease in breakup time with increasing injection pressure. Both also demonstrate that chamber pressure plays a role in breakup time, but interestingly they find opposite trends. Presumably, this arises from the differences between the nozzle geometries in these two studies.

A consequence of the larger forces and shorter liquid breakup times that exist as injection pressure increases is the reduction in size of the droplets that are produced. Fig. 20 illustrates the changes in droplet size distribution that accompany the decrease in breakup time for the 0.1 MPa curve in panel B of Fig. 19. As pressure increases, mean diameter decreases from 17 mm at 20 MPa to 7 mm at 150 MPa, while the width of the distribution narrows from a full width at half maximum of 14 mm to 5 mm. Similar decreases in droplet size are reported in other studies (Hoffmann et al., 2014; Song and Park, 2015). Higher injection pressures also induce greater air entrainment. The combination of smaller droplets and more effective mixing leads to faster fuel evaporation and, thereby, less piston and cylinder impingement (He et al., 2012; Yamaguchi et al., 2019).

The engine cylinder background gas density, or pressure, also plays an important role in the spray dynamics (Yamaguchi et al., 2019; Medina et al., 2020, 2021b). One example is breakup time, as noted in Fig. 19. While chamber pressure has opposite effects in the two studies, its influence decreases with increasing injection pressure in both cases. Other properties are affected as well. Spray penetration decreases with increasing gas density due to the higher aerodynamic drag (Montanaro et al., 2017, 2020). Droplet size increases due to higher drag, since this slows the droplets, which reduces secondary breakup and increases their coalescence rate (Mitroglou et al., 2007).

At low temperatures, under non-evaporative conditions, the spray angle is rather insensitive to both injection and chamber pressure. Fig. 21 illustrates this for a single hole and a 5-hole injector. In both cases the spray angle exhibits less than a 10° change over a range of injection pressures from 30 to 150 MPa and chamber pressures from 0.1 to 2 MPa. The insensitivity to chamber pressure is one of the main advantages of multi-hole

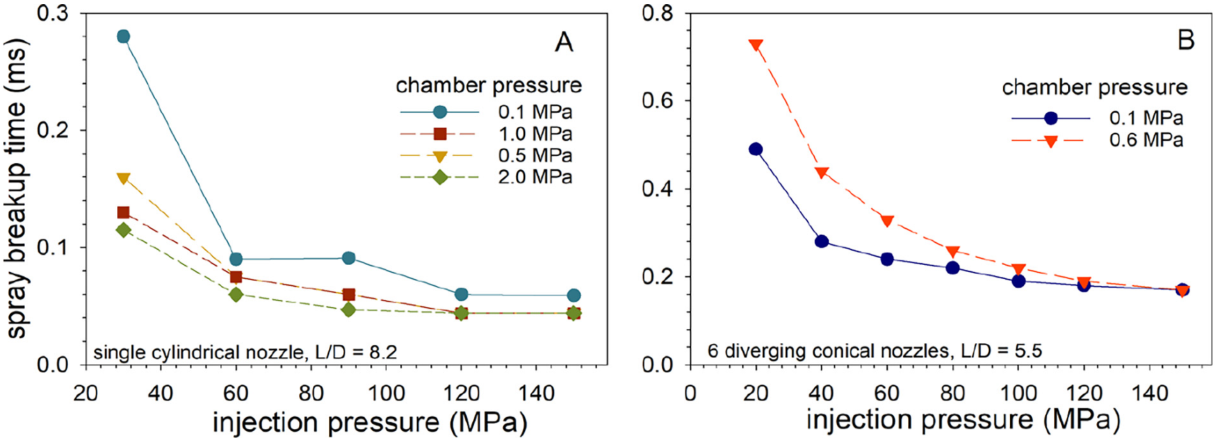

Fig. 19. Spray breakup time versus injection pressure at various chamber pressures. Panel A data - Medina et al. (2018). Panel B data - Yamaguchi et al. (2019).

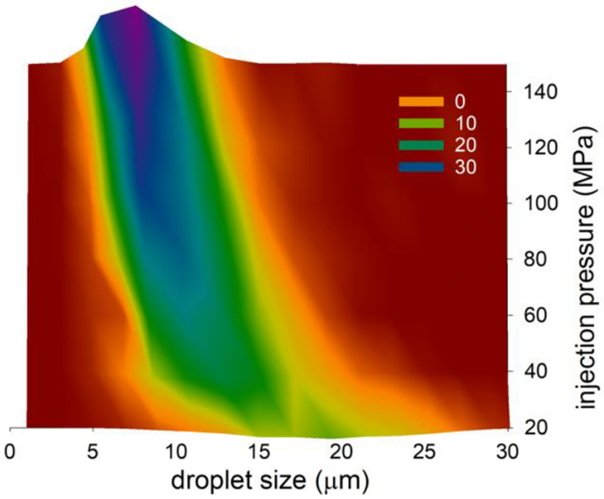

Fig. 20. Spray droplet size distribution as a function of injection pressure (Yamaguchi et al., 2019).

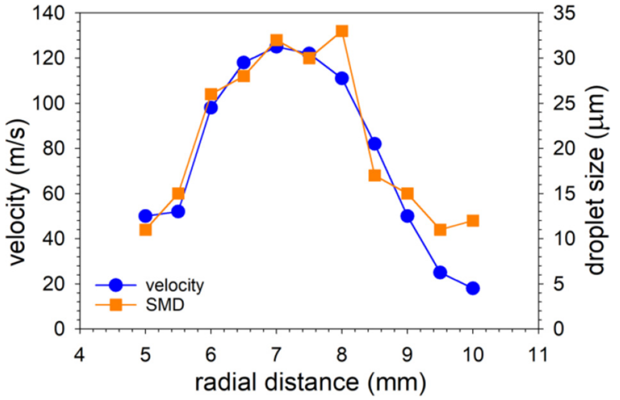

Fig. 22. Spray velocity and droplet Sauter mean diameter (SMD) as a function of distance from the injector axis at 10 mm from the nozzle exit (Mitroglou et al., 2007). Data are for an asymmetric 6-hole injector with nozzle L/D = 2.14.

injectors over earlier generation swirl injectors (Mitroglou et al., 2007). This becomes important in situations where changes in spray shape can affect the fuel air mixture at the spark plug, for example, in spray guided injection and in late injection during the compression stroke.

As liquid spray exits an injector nozzle it develops radial velocity and droplet size profiles where the highest velocity and largest size droplets are in the core and slower, smaller, droplets exist at the spray's periphery (Kale and Banerjee, 2018). Fuel near the orifice wall experiences greater shear forces, first from the wall, and then from the air after it exits the orifice; thus, fuel at the periphery tends to break into smaller droplets than it does in the flow core. Droplets in the core are larger since they are less exposed to entrained air and have more opportunity to coalesce via collisions. Fig. 22 displays examples of these distributions from radially resolved droplet size and velocity measurements by Mitroglou et al. (2007). Similar results are reported by Jiang et al. (2019). Measurements and analysis by Bornschlegel et al. (2018) describe in detail the velocity profile development along the jet axis. The resulting spray momentum is concentrated in the core, giving liquid sprays their characteristic sharp tipped appearance (Kale and Banerjee, 2018). However, this picture changes when the spray droplets begin to evaporate.

Temperature affects spray characteristics primarily through its role in determining fuel's transition from liquid to vapor. Therefore, detailed investigations of fuel injection at elevated temperatures often measure both the liquid and vapor spray components. These studies typically combine two optical techniques, for example schlieren and Mie scattering, or schlieren and shadowgrahy, to record separate images of the vapor and liquid sprays (Allocca et al., 2016; Payri et al., 2017; Kale and Banerjee, 2018). The insets in Fig. 23 provide two examples. The lower left image shows the normal multi-hole spray pattern, with red outline demarking the vapor phase and blue outline highlighting the liquid phase. The image at top right illustrates a collapsed spray due to flash boiling.

As temperature increases, so does the rate of fuel evaporation. This reduces liquid penetration, as the graph in Fig. 23 shows. Evaporation reduces droplet momentum, which slows axial progress, and it increases radial dispersion. The result is an increasingly blunt spray tip with vapor preceding liquid droplets. Rapid evaporation is beneficial since this improves fuel air mixing and reduces impingement. However, high temperatures and high background gas densities can lead to dramatic changes in spray shape.

Flash boiling is an important example of this (Wu et al., 2016; Montanaro et al., 2017, 2020; Kale and Banerjee, 2018) and is the subject of a recent review (Chang et al., 2020). It occurs when the fuel saturation vapor pressure exceeds the engine cylinder pressure (see Section 6.4). Under these conditions the fuel undergoes a phase transition forming bubbles in the liquid spray. When these burst, they break the surrounding liquid into small droplets with high radial as well as axial velocity. This increases the spray width. In multi-hole injectors, the resulting droplet dispersion causes interactions between the individual spray plumes. This inhibits air entrainment, which leads to a low-pressure region along the injector axis that causes the plumes to collapse into a shape such as illustrated in the top right inset of Fig. 23.

Fig. 24 displays the changes in mean droplet size and velocity with increasing fuel temperature as measured in a constant volume spray chamber

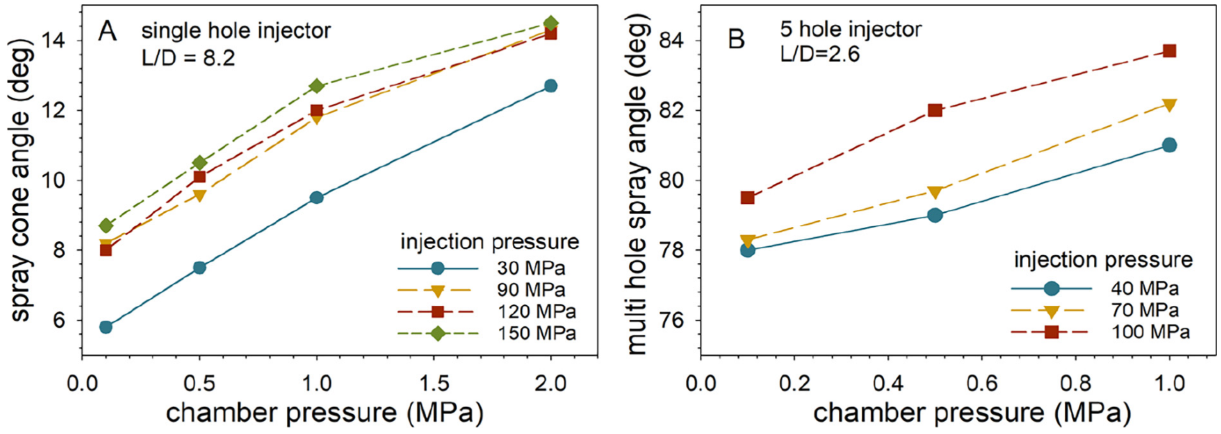

Fig. 21. Dependence of spray angle on chamber pressure at various injection pressures. Panel A: Single hole injector (Medina et al., 2018). Panel B: 5-hole injector (Montanaro et al., 2020).

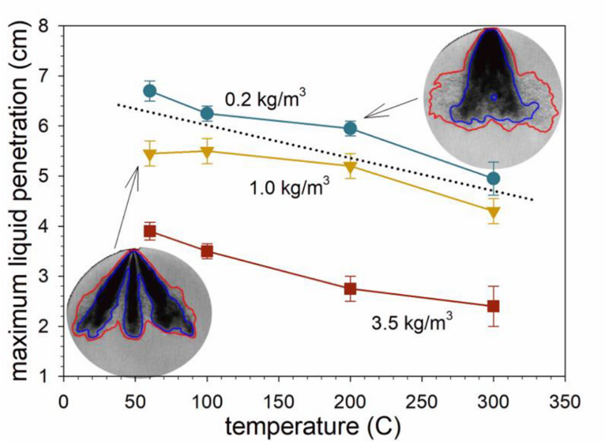

Fig. 23. Liquid fuel penetration versus temperature at various chamber densities (Montanaro et al., 2017). Insets show normal spray pattern (lower left) and collapsed spray pattern due to flash boiling (top right); arrows point to corresponding temperature, density points. The dotted line separates normal and flash boiling regions.

(Kale and Banerjee, 2018). Droplet size decreases from enhanced evaporation. Droplet velocity at first decreases as the evaporating spray loses momentum, but then increases above ~100 °C, which the study attributes to flash boiling. The ability of flash boiling to generate small high velocity droplets at modest injection pressures makes it an attractive potential alternative to high pressure injection (Chang et al., 2020; Sun et al., 2021). However, the spray collapse affects combustion characteristics, such as ignition delay, flame speed, and heat release rate, it can increase liquid penetration, and the extent to which PM emissions are reduced is not clear; these are questions that are just beginning to be investigated (Li et al., 2021). Other potential downsides to injection by flash boiling are that it can lead to local enrichment if a heavy fuel component does not evaporate, and it can exacerbate tip wetting and injector deposits (Huang et al., 2021).

Spray collapse also occurs at high chamber temperature and density, as depicted by Fig. 25. At high temperatures, e.g., above 300 °C, fuel evaporates rapidly. When the chamber gas density is moderate, the spray vapor penetrates more rapidly than the liquid, but maintains approximately the same angle. This changes at high density. With sufficient drag, the fuel vapor's axial velocity slows, causing it to spread radially. This shields the liquid from the hot background gas, which slows evaporation and together with the collapse in spray angle increases penetration. The experimental investigation by Payri et al. (2017) has provided extensive data on the combined effects of high temperature and density on spray characteristics; however, more work is needed to understand the mechanism and implications on GDI engine PM emissions.

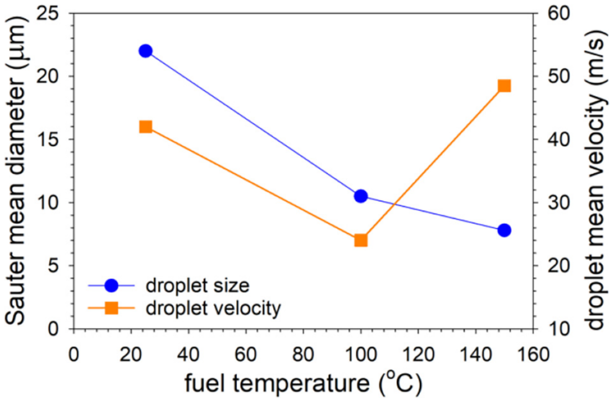

Fig. 24. Dependence of droplet Sauter mean diameter and mean velocity dependence on fuel temperature (Kale and Banerjee, 2018). Chamber density is 0.1 MPa.

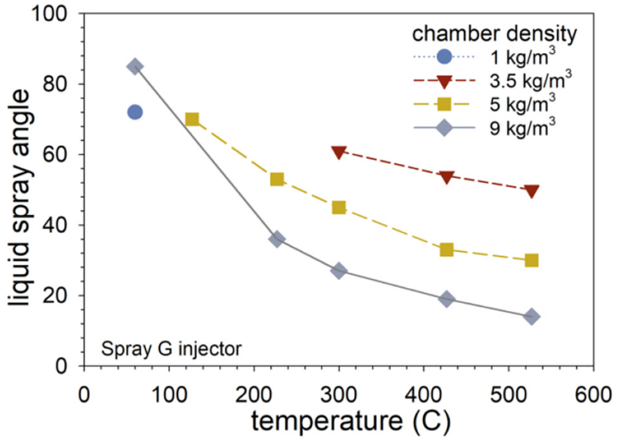

Fig. 25. Liquid spray angle dependence on chamber temperature and gas density (Payri et al., 2017).

There are three main types of GDI fuel injectors: multi-hole, outward opening, and swirl. Multi-hole injectors, such as shown in Fig. 32A, are the most common in current engines. Many factors go into their design. The number of nozzles and their placement vary depending on the desired spray pattern and fuel targeting. The injector can have a symmetric or asymmetric nozzle arrangement, and it can omit or include a central nozzle. The nozzles can be cylindrical, conical diverging, or conical converging, and the length to diameter ratio can vary. Optimal injector design depends on the combustion chamber arrangement, injector placement, and intended intake air motion, among other considerations. While specific spray characteristics vary between different injector designs, as seen in Figs. 18, 19, and 21, its ideal function remains to introduce a fuel spray that yields a homogeneous fuel air mixture at the spark plug with a minimum or no liquid fuel deposition on the piston or walls.

The optimal number and arrangement of nozzles will depend on the specific engine. The nozzle shapes, however, affect spray characteristics in general ways that carry across engine designs. Larger diameter nozzles increase spray penetration and angle, whereas small diameters decrease spray angle (Medina et al., 2020). Divergent nozzles reduce spray penetration and increase angle, whereas straight and converging nozzles produce longer and narrower plumes. The spray tip velocity from a divergent nozzle is lower than from cylindrical and converging nozzles, which results in longer breakup times; however, the differences become less pronounced with increasing injection pressure. Yamaguchi et al. (2019) observed that divergent nozzle sprays decelerate with time after injector opening, whereas sprays from straight and converging nozzles into ambient pressure do not. They attributed this to a decrease in spray angle over time from an initial value enhanced by cavitation during needle opening. Converging nozzles have also been reported to have a greater propensity for spray collapse under flash boiling conditions (Jiang et al., 2019).

The potential for diverging nozzles to reduce fuel impingement has recently been investigated in detail by Moon et al. (2020). They find that this nozzle geometry promotes a consistent hydraulic flip flow structure within the nozzle (flow separation without reattachement to the wall), which promotes a stable exit flow, whereas a straight hole nozzle exhibits unstable flow separation (Pratama et al., 2022). The flow in the diverging nozzle develops a crescent shape, which extends outside the exit where the shape increases air contact and enhances spray breakup. Engine measurements show a factor of three reduction in particle number emissions for the diverging nozzle at 15 MPa injection pressure relative to a cylindrical nozzle; however, by 35 MPa the improvement is minimal.

Other aspects of nozzle design also impact spray characteristics. For example, Medina et al. (2021b) find that inlet rounding increases the mass flow rate compared to a straight cylinder, and Whitaker et al.

(2011) and Behringer et al. (2014) report that laser drilling provides better atomization and spray dispersion than spark eroded nozzles. On the other hand, Duke et al. (2017) observe that small scale features and hole to hole variations can have a relatively large impact on the external flow. The possibility that elliptical nozzles can improve spray quality and mixing is also being investigated (Yu et al., 2021). Thus, work is continuing to identify injector design features and manufacturing processes that help reduce PM emissions.

One of the advantages of direct over port injection is the ability to make multiple injections per cycle. Since spray penetration increases with injection duration, splitting the desired fuel mass into multiple injections, each with shorter penetration, reduces the fraction of fuel that ends up as liquid films. For example, Imaoka et al. (2015) report a 60 % reduction of wall fuel film when splitting a 2.1 ms injection into three 0.7 ms injections and find that the triple injection also improves fuel air mixture homogeneity. Su et al. (2015) report similar results. They compare measured solid particle number exhaust concentrations and computational fluid dynamics simulations of wall fuel film mass for various numbers of injections. As displayed in Fig. 26, the results show an association between solid PN reductions and lower piston and cylinder liner fuel film mass with an increasing number of injections. In each case, lower solid PN emissions are achieved by reducing the fuel mass in the first injection and by keeping the second injection timing roughly within the optimum window shown in Fig. 16 to ensure adequate fuel air mixing.

Although splitting the required fuel into multiple injections can decrease particulate emissions, this introduces additional degrees of freedom into GDI engine calibration; thus, care is needed to ensure that emissions benefits extend across engine operating conditions. Szybist et al. (2011) explored multiple injections as part of their study into PM emissions from ethanol blended gasoline. They saw that double injections lowered PM levels at advanced injection timings but increased them as the timing was retarded. Splitting the fuel into two injections lowers fuel penetration but requires more time to ensure mixture preparation. This is beneficial in early injection, when short penetration lengths are needed to avoid piston impingement, but ample time exists to complete fuel air mixing from both injections. As injection timing is retarded, longer penetration is tolerated, whereas the time available for mixing shortens; thus, splitting the fuel injection eventually increases PM emissions. Szybist et al. (2011) concluded that in some cases a well optimized single injection may be preferred over multiple injections,

Several manufacturers have recently been equipping their gasoline engines with both port and direct fuel injectors, a technology first introduced by Toyota as D—4S injection (Ikoma et al., 2006). This is in essence a split injection strategy that advances the first injection to earlier time, with the port fuel injector providing a “zero” penetration first injection. Port, or port plus direct, injection is typically used at low and medium load and rpm conditions when charge cooling is less needed, and the fuel air mixing benefits of port fuel injection keeps emissions low. Direct injection, or a greater fraction of direct injection, is used at high speed - load conditions so that evaporative cooling in cylinder can help reduce knock. Tests of a 2018 dual injection 2.5 L car revealed a fuel economy of 34 mpg and FTP weighted average PM mass emissions of 0.9 mg/mi (Fanick et al., 2019), with the latter demonstrating the potential to meet the upcoming 2025 LEV III 1 mg/mi PM mass standard.

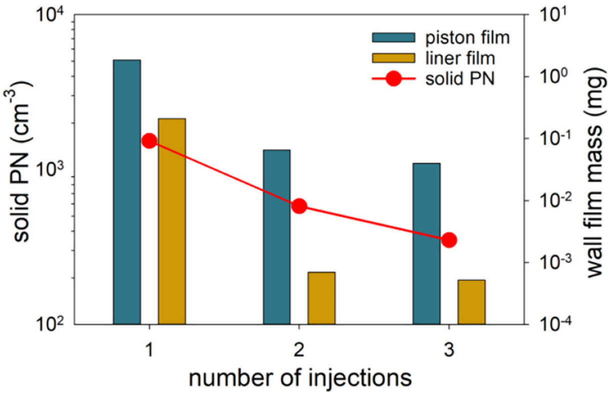

Fig. 26. Impact of multiple fuel injections on solid particle number emissions and wall fuel film mass (Su et al., 2015). Engine operation is steady state at 1000 rpm, 11 bar BMEP. Solid PN values are experimentally measured. Fuel film mass is modeled.

The addition of a port fuel injector may also help reduce the intake valve deposits that have been associated with GDI engines (Guinther and Smith, 2016). These arise over time from a combination of lube oil, partial combustion products, and heat. Port injection helps control deposit buildup by the washing action of fuel injected onto the valve, but this does not occur with direct injection. However, with the development of coalescing filters and impactors to limit the amount of oil aerosol that can enter the engine via the PCV valve, it is not clear to what extent the deposit issue currently motivates adoption of the dual injector technology.

4.2. Injector tip wetting

Injector tip flames provide strong evidence for PM emissions from liquid fuel films on the tip. Imaoka et al. (2019) examined this phenomenon more closely to develop a quantitative relationship between the amount of liquid fuel and the particle number concentration in the exhaust. First, they tested two injectors with different extents of tip wetting. The results show a correlation between the intensity of the injector tip flame and the tip wetted area. Next, they defined a tip wetting index based on the wetted area of the injector tip and the laser induced fluorescence intensity registered by the fuel film produced when testing injectors in a constant volume chamber. More precisely, the wetting index equals wetted area times average LIF intensity. They then installed the injectors in a 1.6 L, 4 cylinder, GDI engine run at 1200 rpm and 700 kPa IMEP. The particle number emissions exhibited the PN drift phenomenon depicted in Fig. 12, rising to a plateau after about 90 min of engine operation. Imaoka et al. (2019) attribute the difference between plateau and initial PN concentrations to particle emissions from the injector tip. Their results, displayed in Fig. 27, show that tip PN emissions from a series of injector designs exhibiting different levels of tip wetting correlate well with wetting index. This index is very likely specific to this engine, operating condition, and fuel, but it does substantiate the causal link between injector tip fuel film mass and the amount of PM emissions. Moreover, it validates measurements of tip wetting as a viable approach to study methods for reducing injector tip related PM emissions.

Tip wetting occurs in general from the start of injection to needle closing and to fuel dribbling from the sac after end of injection (EOI). The main mechanisms involve spray contact with the walls during fuel flow through the nozzle, and the droplet recirculation and ligament contraction

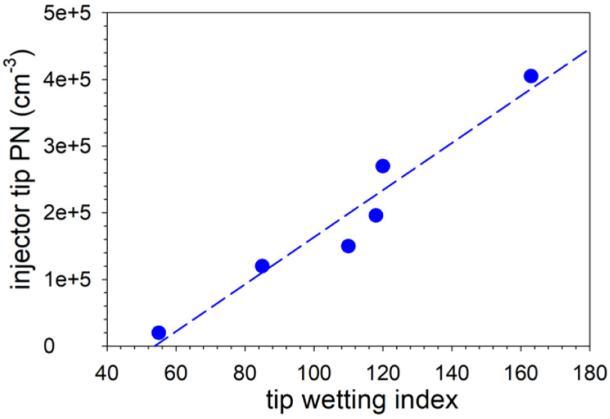

Fig. 27. Correlation between injector tip PN emissions and tip wetting index (Imaoka et al., 2019).

back to the tip that occur upon needle closing (Medina et al., 2021a). Wetting can take place continuously or intermittently during steady state injection when the spray angle exceeds the point at which the spray contracts the nozzle counterbore wall, as depicted by the inset in Fig. 28. This arises from flow instabilities or turbulence, which distort the spray cone (Backes et al., 2020). However, under non-flash boiling conditions, little wetting is generally observed, likely because spray droplets mostly rebound from the wall and are re-entrained into the spray (Backes et al., 2020; Huang et al., 2021).

The most important factor for wetting during injection is flash boiling (Leick et al., 2018; Huang et al., 2021). This occurs when the fuel's saturation vapor pressure exceeds the ambient pressure, for example from fuel heating in a hot injector. Superheated fuel forms bubbles, and their expansion increases the spray angle. Fig. 28 illustrates the spray width at two locations: inside the nozzle counterbore (width 1) and just past the nozzle exit (width 2). Both widths are nearly independent of the saturation to ambient pressure ratio for $P_{sat}/P_{amb} < 1$. When this ratio exceeds unity, width 1 increases slightly, likely because it is constrained by the counterbore, but width 2 diverges substantially from flash boiling.

Bubbles caused by flash boiling also increase droplet radial velocity. This raises their impact energy against the wall, which can shift the collision dynamics into a regime where droplets stick to and spread along the nozzle wall instead of rebounding from it (Huang et al., 2021). Thus, temperature or ambient pressure variations that produce flash boiling conditions increase wetting. Fig. 29 illustrates the dependence of wetted area on saturation to ambient pressure ratio. It remains constant for $P_{sat}/P_{amb} < 1$ but increases sharply as this ratio approaches unity. Spray contact with the wall continues to grow as P_{sat}/P_{amb} increases beyond unity, but so does the fuel evaporation rate, with the net result that wetted area decreases with further superheating. Increasing injection pressure can reduce wetting caused by flash boiling (Leick et al., 2018; Backes et al., 2020). Higher pressure increases the fuel flow rate, which reduces time for flash boiling, shifts its occurrence towards the nozzle exit, and increases droplet entrainment.

The transient effects of nozzle opening and closing represent the other main source of tip wetting. Backes et al. (2020) report wetting at the start of injection, which arises from a higher likelihood of flash boiling when the needle is partially lifted, and the fuel pressure and flow momentum are initially low. However, the larger impact on wetting occurs at the end of injection, when spray dynamics suddenly change and residual fuel empties from the sac. Fig. 30 illustrates the principal fates of fuel after nozzle closure. Panel A shows the state of the fuel just at needle closing. Behind the tail end of the fuel spray are large droplets with low momentum that form by atomization of the low-pressure flow as the needle closes. Fuel in the counterbore forms ligaments that extend away from the nozzle. Panel B shows the fate of these after injector closing. Hélie et al. (2021) observe that the ligaments can exist as cylindrical films that eventually collapse and contract onto the injector tip. Likewise, some large droplets are entrained back to the tip by the air motion around the injector.

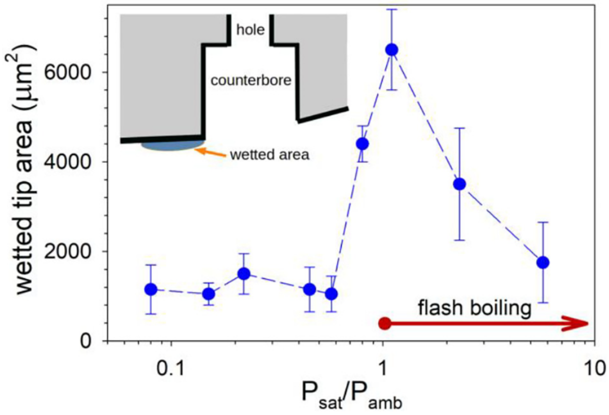

Fig. 29. Size of wetted tip area versus the ratio of saturation to ambient pressure (Huang et al., 2021). Inset shows schematic of wetted area adjacent to nozzle.

A number of factors play a role in EOI wetting (Leach et al., 2018). The decrease in injection pressure during closing can increase the spray angle and exacerbate flash boiling (Backes et al., 2020). Needle bounce allows spurts of low-pressure fuel flow, which generate additional large, low momentum, droplets and ligaments that further wet the injector tip (Huang et al., 2020). There are measures that can lower EOI wetting. Reducing sac volume and increasing needle closing speed can limit the amount of fuel and time available for EOI wetting (Backes et al., 2020; Dober et al., 2020). Increasing injection pressure can attenuate the propensity of needle bounce (Huang et al., 2020).

Nozzle design is another feature of fuel injectors that affects wetting. Several studies have examined wetting behavior for various counterbore dimensions and conical hole shapes, but the results are thus far inconsistent. Huang et al. (2020) investigated tip wetting as a function of counterbore diameter. Their results in Fig. 31A show an initial increase and subsequent decrease in wetting as the diameter is enlarged from 0.25 to 0.55 mm, with the main contribution coming from needle bounce. A lesser amount of wetting occurs during injection, which appears independent of counterbore size, and a small contribution, declining slightly with increasing diameter, arises from end of injection dribble.

In contrast, Dober et al. (2020) report that wetted area increases with counterbore diameter. Their observations, shown in Fig. 31B, indicate that wetting occurs primarily during injection and from residual fuel in the sac, but with little contribution from needle closing. The wetting increase is attributed to more spray - rim contact as the counterbore circumference grows in length. Oh et al. (2017) and Backes et al. (2020) similarly report increased wetting with larger counterbores. Interestingly, although the latter study finds wetting to increase with counterbore diameter, it

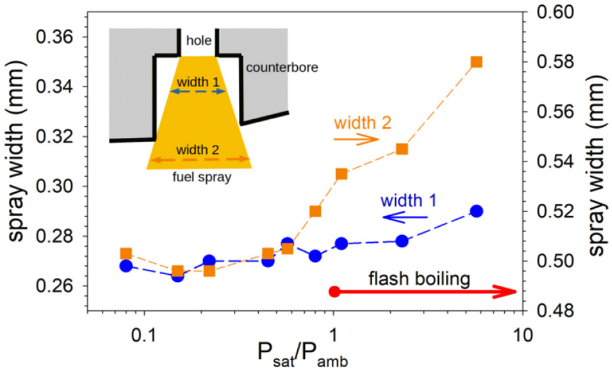

Fig. 28. Variation of spray width versus the ratio of saturation to ambient pressure (Huang et al., 2021). Inset shows schematic of spray in injector nozzle and the positions of the two width measurements.

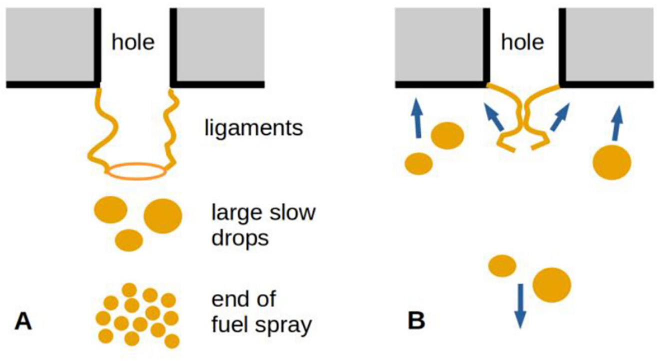

Fig. 30. Schematic depiction of spray dynamics at end of injection (Hélie et al., 2021). Panel A: At needle closing. Panel B: Shortly after EOI.

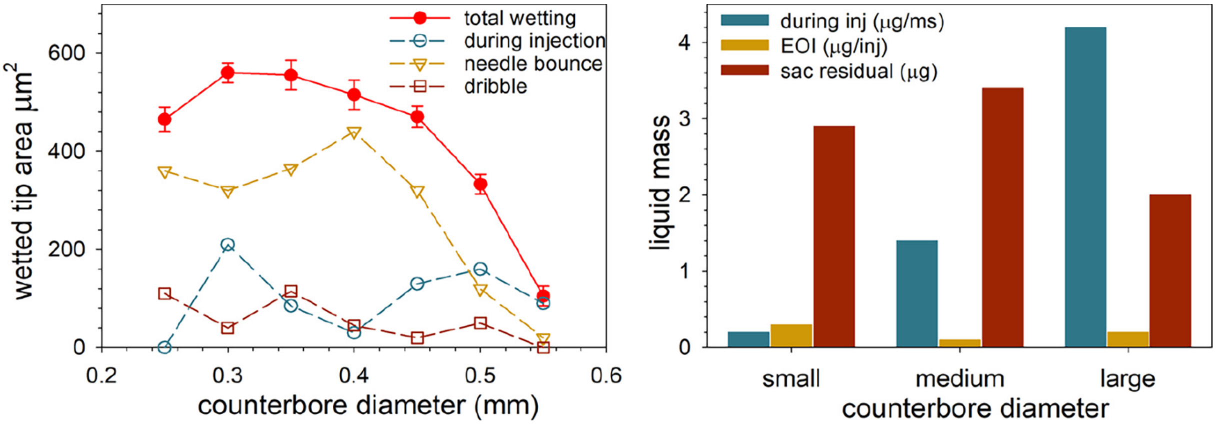

Fig. 31. Wetted tip area versus counterbore diameter. Panel A: 4 MPa injection into ambient (Huang et al., 2020). Panel B: 10 MPa injection (Dober et al., 2020).

agrees with Huang et al. (2020), and not Dober et al. (2020), that the main contribution comes from the end of injection.

These discrepancies likely arise from the wide range of experimental conditions. Backes et al. (2020) conducted their measurements with an 80 °C fuel temperature and 0.04 MPa chamber pressure to promote flash boiling, whereas Huang et al. (2020) carried theirs out at 25 °C and 0.1 MPa. The presence of injector deposits can also affect nozzle design studies. Backes et al. (2020) and Huang et al. (2020) used clean injectors, whereas Dober et al. (2020) investigated tip deposits, but do not state if these affected their results on the impact of counterbore diameter.

Other nozzle designs are also receiving study, such as the use of tapered holes. Recent work by Zhang et al. (2021) compares converging, straight, and diverging nozzle geometries under sub-cooled and flash boiling conditions. They observe significantly worse wetting for straight and converging nozzles under strong flash boiling conditions, but not with diverging nozzles. Consistent with this, Medina et al. (2021a) find lower particle number emissions for diverging versus converging nozzles over a range of engine loads. Zhang et al. (2021) speculate that diverging nozzles may present less resistance to exiting droplets or mitigate choked flow from flash boiling but admit that the reasons for lower wetting are not well understood. It is apparent from these recent publications that injector design remains an area of ongoing research.

4.3. Injector tip deposits

As shown in Fig. 12, PM emissions can increase substantially over time after installing new injectors in a GDI engine owing to tip deposit formation. Fig. 32 compares injector tips before (panel A) and after (panels B & C) 13 h of operation in a 1.6 L GDI engine with a centrally mounted injector. Clearly a significant deposit has formed on the tip, which can lead to a deterioration of PM emissions by enhancing tip wetting or producing spray patterns that exacerbate piston and wall impingement.

The deposits have an irregular porous structure, as seen from the side view in Fig. 32C. Detailed examination via scanning electron microscopy reveals that injector deposits are complex layered materials. Barker et al. (2019) found heavily fouled injectors to be coated mainly by a thin carbonaceous film covered by a porous layer of 60–100 mm roughly spherical particles in some areas and by densely packed smaller globular structures in other areas. Edney et al. (2021) similarly describe tip deposits in terms of a thin film covered with small spherical particles and regions of thicker carbonaceous deposits.

Elemental analysis indicates that GDI injector tip deposits contain primarily carbon and oxygen, which implicates fuel as the primary source (Dearn et al., 2014; Barker et al., 2019). The deposits also include sulfur, calcium, and lesser amounts of other elements derived from lube oil and fuel additives. The recent spatially resolved mass spectrometric studies by Edney et al. (2020b, 2021) have provided new insights into injector deposit composition. Their results, illustrated in Fig. 33, reveal a layered structure with long chain alkylbenzyl sulfonates, and carboxylic acids, at the outer surface and large polyaromatic hydrocarbons (PAHs), and carbonaceous matrix successively below.

Sulfonates presumably arise from lube oil, since calcium dodecyl benzene sulfonate, $Ca^+[C_6H_4(SO_3)(C_{12}H_{25})]^-$, has been evaluated as a detergent for the lube oil additive package (Nassar et al., 2017). Imaging mass spectra across the deposit reveals that these species are non-uniformly distributed, which suggests that they arise from lube oil contamination and are not the main source of deposits. These compounds, as well as the carboxylic acids break down readily by loss of their alkyl chains and, thus, are only seen near the top of the deposit. In contrast, PAH ions up to $C_{66}H_{20}^+$, and carbonaceous ions of the form C_n^- and C_nH^- are found in the bulk, with the latter dominating at lower depths. Based on their uniform spatial distribution across the deposit, Edney et al. (2021) determine that GDI injector deposits are predominantly fuel derived.

Two chemical pathways have been suggested to produce injector deposits: pyrolysis and low temperature auto oxidation (Xu et al., 2015). Based on these mechanisms, and the structural and chemical nature of tip deposits, Slavchov et al. (2018) developed an adsorption - precipitation model for injector external deposit formation. They propose that deposit precursors form in the liquid film on the injector tip via reactive species such as NO_2, O_2, organic peroxy radicals, and alkoxy radicals (Kinoshita et al., 1999). As cylinder pressure decreases during the expansion stroke, the fuel film begins to boil, and any non-volatile residue adsorbs or

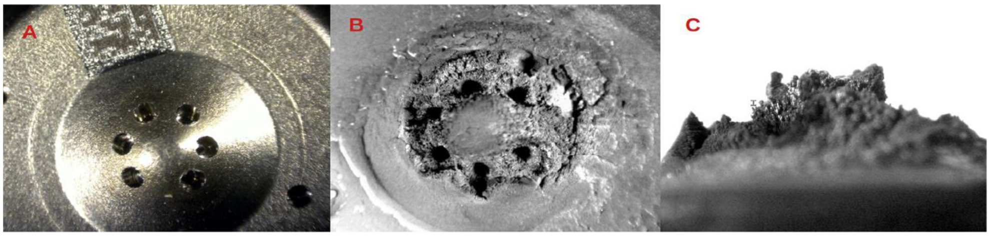

Fig. 32. Fuel injector tip deposits. Panel A: clean injector. Panel B: After 13 h engine operation at 2840 rpm, 6 bar BMEP, and 95 °C engine coolant. Panel C: Side view after deposition. (Images courtesy of T. Han and A. Boehman, University of Michigan).

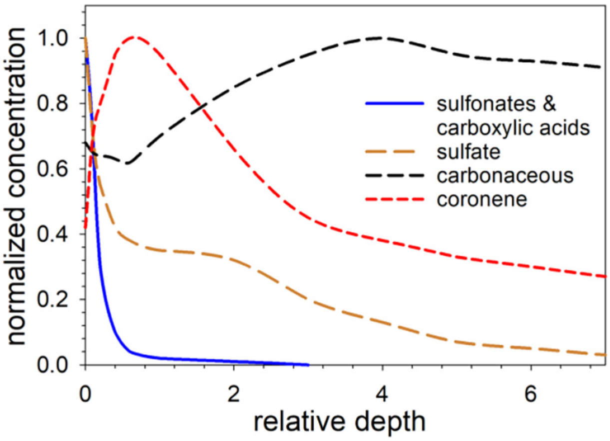

Fig. 33. Deposit composition as a function of depth (Edney et al., 2021).

precipitates onto the injector tip. While this model makes many assumptions regarding the initial steps in deposit formation, it is consistent with observations. Thus, antioxidant additives help reduce deposits by scavenging radicals assumed responsible for fuel degradation in the model and dispersants help by inhibiting the precipitation assumed to produce solid deposits.

Injector deposits can form both externally and internally. Dearn et al. (2014) observed deposits on the tip, counterbore, inner hole, needle and seat. Higher levels of deposits appear in regions closer to the combustion chamber; thus, larger deposits are found in the counterbore than the inner hole. There are chemical differences as well. Edney et al. (2021) found a different layer structure for the needle versus the tip. The PAH and carbonaceous signals from the needle deposits are lower than from the tip, and the largest PAHs in the needle are smaller than those in the tip. This suggests that the conversion of wetted fuel to large aromatics occurs more slowly on the needle, likely due to its lower temperature compared to the external tip. Deposit location can also have a disproportionate impact on injector performance. For example, deposits in the counterbore or hole are more prone to affect spray geometry than external surface deposits, leading Jiang et al. (2017) to suggest injectors be designed without counterbores.

There are steps available to minimize injector deposits. The first is to reduce wetting, for example by increasing injection pressure and avoiding flash boiling conditions. Given that some wetting may be unavoidable, it is important to deter any deposit precursors that may form from attaching to the injector. According to the model proposed by Kinoshita et al. (1999) and Slavchov et al. (2018), these precursors initially form in the liquid film and subsequently deposit when the fuel evaporates. Therefore, keeping the injector tip sufficiently cool that some liquid remains until the next injection can wash the precursors away should suppress deposit formation. This is a function of fuel characteristics; thus, Kinoshita et al. (1999) recommend keeping injector tip temperature below T90 of the fuel. Injectors designs that reduce heat transfer from the combustion gases and increase heat conductivity from the injector can help reduce injector temperature. Raising injection pressure can also help, since this will increase how effectively the injected fuel can wash away deposits and deposit precursors (Jiang et al., 2017).

There have been attempts to add coatings to injectors that deter deposit attachment, but these have not been found effective (Imoehl et al., 2012; Xu et al., 2015). The thinking is that the coating may delay deposit onset, but once deposit formation begins, the coating no longer has any effect. On the other hand, fuel additives offer a potential avenue to control injector deposits (Henkel et al., 2017). Tests by Barker et al. (2019) found that an existing additive designed for PFI engines was ineffective at controlling GDI injector deposits. However, they also tested a new generation additive designed for GDI applications. The results are summarized in Fig. 34. Recent work by Monroe et al. (2021) shows that it is important to optimize the additive concentration to both control deposit formation and yield a minimum in PM emissions.

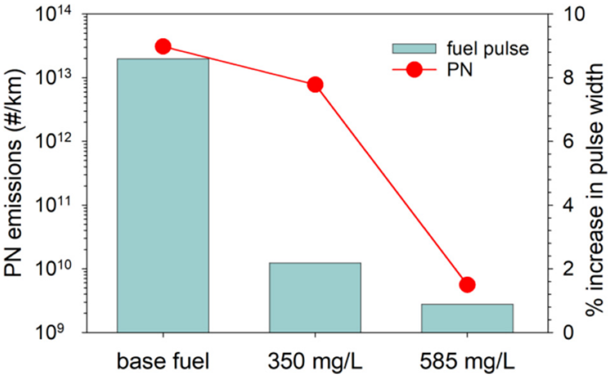

Fig. 34. Effect of deposit control additive on PN emissions and injection pulse width (Barker et al., 2019).

One of the consequences of deposits is a restriction in fuel flow, which is reflected by an increase in pulse width needed to maintain a constant injected fuel mass. The results show that the GDI specific control additive reduces the pulse width increase incurred over a 48-h coking test. At the same time the additive reduces the PN emission rate measured after the 48-h test.

4.4. Controlling cold start and high speed/load PM

The literature on GDI engine PM emissions mechanisms and mitigation, such as discussed in the preceding sections, is largely based on steady state testing. However, it is well known that GDI PM emissions are highly dependent on transient operation and, as Fig. 35 demonstrates, typically dominated by the engine cold start. The figure displays cold start PM mass and solid particle number fractions for the US FTP and EU New European Drive Cycle (NEDC). These are defined here as the phase 1 (cold start) fraction of the three phase FTP cycle and first ECE 15 fraction of the NEDC, respectively. The results are the same in terms of mass and number emissions for both drive cycles. Cold start PM represents 55–75 % of the total for seven of the eight vehicles. Even for Vehicle 7, the ~35 % by mass and ~ 40 % by number fractions are disproportionately large, given that the cold start represents 195 out of the 1180 s NEDC cycle.

Cold start conditions exacerbate PM formation in two ways: First, the cold combustion chamber and limited intake air motion during engine crank slow fuel evaporation and mixing, which increases impingement and condensation onto chamber surfaces. Second, the fuel charge must be enriched above stoichiometric to compensate for slow evaporation and produce an ignitable fuel air mixture at the spark plug. As a result, large quantities of liquid fuel remain after the combustion event and provide a substantial source for PM formation.

Oh and Cheng (2017) provide deeper insight into cold start PM sources. They mimic the cold start by steady state engine testing at fast idle (1200 rpm and 2 bar NIMEP) and maintaining all fluids, fuel, lube oil, and engine coolant, at 25 °C. Then they compare PM emissions for a series of fuels: premixed methane-air, premixed gasoline-air, and various combinations of premixed methane + liquid gasoline - air. The methane-air and premixed gasoline-air mixtures lead to negligible PN emissions compared to normal GDI engine cold fast idle operation. This changes when gasoline is injected directly into the engine. Fig. 36A plots the accumulation mode (soot) particle concentration versus the gasoline fuel fraction. Particle emissions grow slowly with increasing liquid fraction up to a transition point, beyond which they increase rapidly. Greater intake air motion makes the transition less pronounced at higher engine speed.

What this demonstrates is that even in a cold engine, PM emissions arise primarily from liquid fuel, more precisely from a portion of the liquid fuel. This portion, the fraction above the transition point, varies with injection timing. It increases as SOI is advanced, which shortens the injector to piston

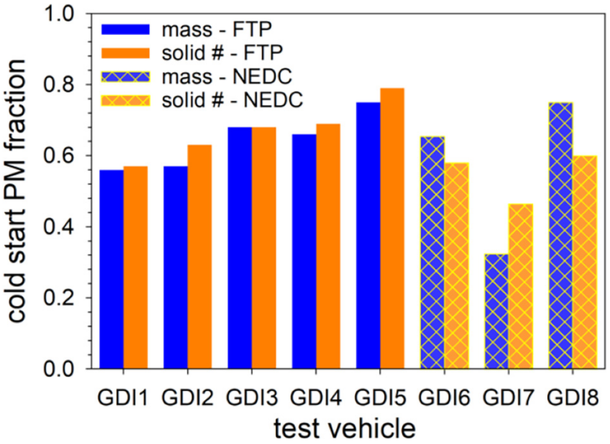

Fig. 35. Cold start fraction of PM emissions from GDI vehicles. FTP data: (Maricq et al., 2017). NEDC data: (Chen et al., 2017).

distance creating more impingement, and as SOI is retarded, which decreases mixing time. The data in Fig. 36B show that PM emissions from the normally fueled engine scale exponentially with the portion of liquid fuel above the transition point. This focuses cold-start strategies to search for conditions best able to tolerate liquid fuel.

The importance of the GDI vehicle's cold start to meeting emissions regulations has been recognized since early after their introduction, will receive increased focus under EU7 and is the subject of a recent comprehensive review that covers both PM and gaseous pollutants (Wooldridge et al., 2022). The EU's decision to extend the solid particle number standard to GDI technology with Euro 6 precipitated searches for engine technology improvements to meet this standard without need for a GPF. The study by Whitaker et al. (2011) favors high fuel pressure to ensure a high-quality injection and reports a three-fold reduction in cumulative PM mass from 15 to 5 mg for a cold start and 60 s idle upon increasing injection pressure from 0.4 to 15 MPa. Higher penetration may limit the ability to raise injection pressure, thus they propose using multiple injections, and show a roughly five-fold decrease in peak particle number emissions when replacing a single injection with four fuel pulses. For catalyst heating, which is an important part of the cold start, they discuss a split injection approach where the second injection occurs during the compression stroke to form a stratified rich mixture at the spark plug, while the overall mixture remains lean to promote exothermic reactions on the catalyst. The study by Piock et al. (2011) arrives at similar conclusions. They, too, find that increasing fuel pressure and using multiple injections lowers cold start PN emissions, and suggest a split injection, stratified charge, strategy to speed catalyst warm-up. Furthermore, they examined valve timing and found that internal exhaust gas recirculation (EGR) by early exhaust valve closure (EVC) was able to reduce cold start PN emissions by nearly 40 % owing to improved fuel evaporation.

A series of publications by Cheng and colleagues presents perhaps the most detailed investigation into GDI engine cold start strategies, in their case employing a side mounted injector. Rodriguez and Cheng (2015) specifically examine the first cycle's impact on particulate and gaseous emissions. They find that a single injection early in the compression stroke works best for the first cycle. A split injection, with a portion of fuel injected late in compression, may require less enrichment, and increase combustion stability, but it substantially increases PM emissions. Spark retard does not improve HC emissions, but it does lower PM, since it reduces the time for post flame pyrolysis.

In a subsequent paper, Rodriguez and Cheng (2016a) extend their analysis to the first three combustion cycles. The extent of fuel enrichment early in the cold start is a key factor in their analysis. Fig. 37 displays their data on exhaust PM mass as a function of enrichment for the first three cycles. As expected from Fig. 36, PM mass increases steeply with the amount of liquid fuel. On the other hand, sufficient fuel is necessary to guard against misfire; thus, the arrows in Fig. 37 mark optimum enrichment factors that ensure combustion but minimize PM emissions. This best enrichment level falls with each successive engine cycle owing to increasing chamber temperature and the residual fuel from the previous cycle. As a result, PM emissions for these three cycles decrease by about an order of magnitude.

Further work by Rodriguez and Cheng (2016b) examined potential cold start PM emissions benefits from adjustments in valve timing. Late intake valve opening reduces cylinder pressure. This increases intake air turbulence and raises the charge temperature at the end of the intake stroke. Rodriguez and Cheng (2016b) estimate that even at cold start the decrease in pressure can be sufficient to promote flash boiling of high volatility gasoline components, which would enhance evaporation and mixing, but they caution that this may also lead to increased piston impingement that can offset the benefit. Their measurements show that delaying intake valve opening results in a 25 % reduction in PM formation. They also examine early exhaust valve closure, but unlike Piock et al. (2011) find that this increases PM for their engine by 48 % over the first 13 cycles. Although the residual gas retained by the early exhaust valve closure may help evaporation, it also reduces the burned gas temperature. This facilitates flame quenching, which leaves larger regions of unburned fuel susceptible to soot formation via pyrolysis.

As mentioned in Section 3, high speed/load engine operation is another operating condition associated with PM emissions owing to the large fuel volumes and reduced evaporation and mixing times involved. High

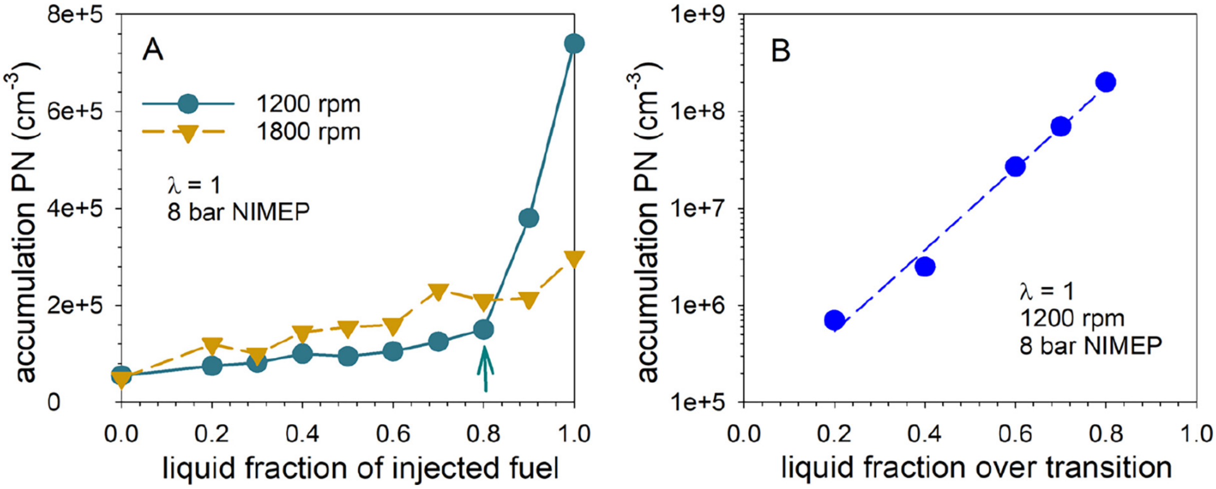

Fig. 36. Liquid fuel impact on PN emissions during cold fast idle (Oh and Cheng, 2017). Panel A: PN versus liquid fraction of gasoline + methane injection. The arrow marks the transition point to high emissions. Panel B: PN emissions under normal fueling versus the liquid portion responsible.

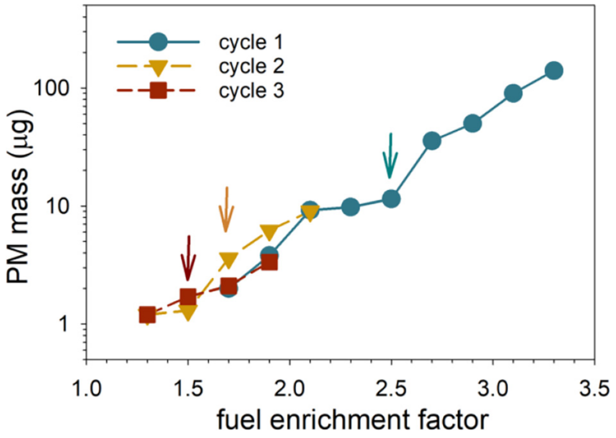

Fig. 37. PM mass emissions as a function of fuel enrichment for the first 3 cycles of engine cold start (Rodriguez and Cheng, 2016a). Arrows mark optimal enrichment for each cycle to minimize CO, HC and PM emissions.

combustion temperature raises soot formation and oxidation rates, but the latter also depends on oxygen availability and, thus, may not keep up. These changes generally lead to modest PM emissions increases under stoichiometric operations. In contrast, much larger increases occur when rich fuel air mixtures, enrichment, is used to reduce engine temperatures and inhibit knock (Wei et al., 2012).

Exhaust gas recirculation (EGR) provides an alternative means to reduce combustion temperature and is often used to lower NO_x emissions (Wei et al., 2012). Internal EGR retains exhaust gas in the engine cylinder by judicious timing of the overlap between intake valve opening and exhaust valve closing. External EGR directs a fraction of exhaust back to the intake port. En route it can be filtered to avoid fouling and cooled to help reduce the intake charge temperature and improve engine power (Fischer et al., 2017).

Hedge et al. (2011) investigated the relationship between EGR and particle emissions from a boosted 1.6 L GDI engine. Increasing EGR from 0 to 25 % lowered PM mass emissions by ~60 % and solid particle number emissions by ~40 % over most operating conditions tested. This was consistent for soot particles, but the number of semivolatile particles increased in some intermediate speed/load cases. They found internal EGR to be the more effective choice under light load, low speed operation. At highway speeds and loads the PM reduction was accompanied by a ~ 3 % improvement in fuel economy. More recently, Fischer et al. (2017) report reductions of 10 % in fuel consumption and 75 % in PM emissions with cleaned and cooled EGR.

4.5. Summary of GDI engine out PM reductions

The recognition of fuel impingement onto the piston and cylinder liner as a major source of GDI engine PM emissions has led to a variety of technical advances over the past decade. There is an optimal window for fuel injection, in which the piston is beyond the fuel spray's penetration length, yet sufficient intake air motion, perhaps augmented by improved intake port design, remains to prepare a homogeneous fuel air mixture by the time of ignition. Increased injection pressure enhances fuel atomization, which reduces impingement and improves mixture preparation. Increasing piston and cylinder wall temperature, especially during cold start, helps evaporate fuel and reduce fuel films. Care is necessary to avoid overheating the fuel or injector, since this can lead to flash boiling and spray collapse conditions that increase penetration and inhibit fuel air mixing. Injector design improvements, such as nozzle geometry, and the adoption of multiple injection strategies have contributed to lower impingement and reduced PM emissions, and research in these areas continues.

Injector wetting occurs from variations in spray width that cause the fuel to contact the nozzle wall and by end of injection spray dynamics whereby ligaments and large droplets formed during needle closing attach to the injector tip. Repeated heat cycling of the fluid film can lead to injector deposits that exacerbate wetting and ultimately deteriorate injection quality. Temperature plays a key role. High temperatures can cause flash boiling which enhances wetting and facilitates evaporative deposition of deposit precursors. High in-cylinder temperatures are desirable to evaporate fuel droplets and fuel film from the piston and cylinder liner, but a relatively cool tip temperature avoids flash boiling and mitigates deposit formation. High injection pressure aids by reducing wetting and flushing deposit precursors. Minimizing sac volume and developing rapid needle open and close mechanisms can reduce EOI wetting. Additives have been, and continue to be, developed that appear capable of controlling deposits. These all help reduce PM formation from injector tip fuel films.

Much has been learned over the past decade or two about optimizing GDI engine cold start for low pollutant emissions. Detailed studies of engine start reveal many avenues to reduce PM by optimizing fuel pressure, enrichment factor, injection timing, intake and exhaust valve timing, spark timing and split injection strategies on a cycle-by-cycle basis to minimize liquid fuel and poor mixtures during engine crank, catalyst heating, and cold acceleration. Translating these opportunities into reality requires tailoring the insights into how these parameters impact PM formation to the specific engine and vehicle under development. The improvements in GDI vehicle PM emissions realized over the past decade attest to the effectiveness of these insights and suggest that future improvements remain possible.

5. Gasoline vehicle PM exhaust aftertreatment

Based on the PM emissions trend displayed by U.S. EPA certification data in Fig. 2, it appears that most new model GDI vehicles can meet the 3 mg/mi Tier 3 and LEV III standards by incorporating engine and fuel injection technology advances described in the preceding section. It remains unclear if these advances will be sufficient to meet the 1 mg/mi LEV III or $6 \cdot 10^{11}$ solid PN/km Euro6 limits, in the latter case particularly with real driving emissions (RDE) testing. Therefore, this section examines PM emissions reduction via exhaust aftertreatment. It begins with gasoline particulate filters (GPF) and examines how this technology has evolved to meet the specific needs of GDI vehicles. It then looks at the three-way catalyst's (TWC) role in mitigating gasoline vehicle emissions impact on ambient PM.

5.1. Gasoline particle filters

With the success DPFs had enabling diesel vehicles to meet the EU's very stringent solid PN standard, it was not surprising that calls to adopt gasoline particulate filters arose soon after extension of this standard to GDI vehicles. Indeed, GPFs are quite effective at reducing GDI PM mass and solid PN emissions (Joshi and Johnson, 2018). Fig. 38 provides an overview of the GPFs impact on PM emissions. It compares particle size distributions along the FTP + US06 drive cycle recorded before and after the GPF. Other comparisons in the literature show similar results (Yang et al., 2018; Liu et al., 2019). Pre GPF PM emissions are dominated by the cold start. In this example, approximately 31 % by number and 43 % by mass of the FTP + US06 engine-out emissions occur during the first 40 s of operation. The GPF greatly reduces these emissions, as well as those during the hot start crank, across the 5–500 nm size range, and nearly eliminates particle emissions for the rest of the drive cycle.

Examples from the literature in Fig. 39 demonstrate the GPF's ability to reduce GDI vehicle PM emissions over a variety of drive cycles. Most such studies utilize separate tests before and after replacing the under body TWC or muffler with a GPF and, thus, may not reflect the efficiency attainable with an OEM designed filter. Nevertheless, these examples reveal ~75 % - 95 % PM mass reductions for the FTP, LA92, and WLTC drive cycles. Most of this variability likely lies with the porosity of the specific GPFs and their state of soot and ash loading.

GPFs have a similar impact on solid particle number emissions. Yang et al. (2018) observed 95 % and 99 % solid PN reductions for two test vehicles on the LA92 cycle, with no impact on fuel economy. Chan et al. (2016) report 84 % - 89 % reductions for the FTP cold start and ~ 95 % reductions

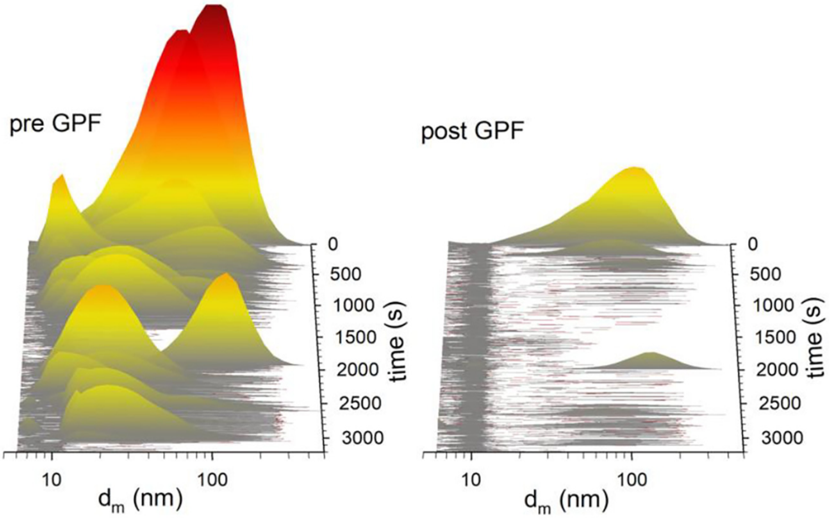

Fig. 38. Pre versus post GPF exhaust particle size distributions during the 3-phase FTP + US06 drive cycle (Maricq unpublished).

in the urban and hot start phases, and interestingly note that the efficiencies are the same using lower size cut points of 3 nm versus 23 nm. GPFs are effective as well for vehicle operation at low ambient temperatures. Chan et al. (2014) measured FTP cold start and weighted average solid PN efficiencies of 75 % and 82 % at 22 °C, 86 % and 90 % at −7 °C, and 68 % and 79& at −18 °C, respectively. While GPFs efficiently remove particles, they have little effect on morphology; soot agglomerates that penetrate the GPF have similar fractal dimension and primary particle sizes as those that enter (Saffaripour et al., 2015).

The situation is different for the US06 drive cycle, and likely other aggressive cycles. The ~30 % to 75 % GPF PM mass efficiencies in Fig. 39B are lower and exhibit wider variability than for the "normal" driving cycles in panel A. Furthermore, efficiency depends on the metric used. Thus, US06 filtration efficiency for vehicle 2 in Yang et al. (2018) is 34 % based on total particle number versus 71 % for solid particle number. Likewise, Chan et al. (2016) report a gravimetric mass-based efficiency of ~21 % versus black carbon (BC) efficiency of 62 % - 88 %.

These differences stem from changes in PM composition. The results indicate that a substantial fraction of US06 PM emissions consists of condensed semi-volatile materials. Indeed, size distribution measurements in these studies reveal strong nucleation mode emissions during the US06 cycle both with and without a GPF. Also, TEM images in a separate study suggest that organic material condenses on post GPF soot aggregates during the US06 cycle (Saffaripour et al., 2015). A bare GPF is ineffective at removing these particles because they are in the gas phase at the ~600 °C GPF temperature during the US06 cycle, whereas a catalyst coated GPF can potentially remove the gaseous precursors.

Passive GPF regeneration can also affect filter efficiency. The US06 cycle solid particle number and BC based efficiencies in the above studies remain a bit lower than their FTP and LA92 counterparts. The high US06 exhaust temperature combined with oxygen available during deceleration fuel cuts cause soot oxidation, which lowers filtration efficiency. Similarly, results from Jang et al. (2018) show significantly higher filtration efficiency when the GPF is mounted underbody as opposed to the close coupled position (~75 % versus ~25 % over the WLTC), presumably because regeneration occurs less frequently at the cooler underbody location.

Beyond laboratory testing, recent studies show that GPF equipped GDI vehicles can meet the solid PN standard during RDE testing, with emissions tests conducted on real world routes that meet a rigorous set of requirements. Demuynck et al. (2017) tested a state of the art, non-GPF, GDI vehicle, which met the $6{\cdot}10^{11}$ solid PN/km standard on the dynamometer and met $9{\cdot}10^{11}$ solid PN/km during on-road tests but increased to $2{\cdot}10^{12}$ solid PN/km at the RDE boundary conditions. After installing a catalyst coated GPF, the emissions were well below the standard during on-road testing and stayed well below $9{\cdot}10^{11}$ solid #/km towards the RDE boundary conditions. McCaffery et al. (2020) tested two GPF retrofitted GDI vehicles over

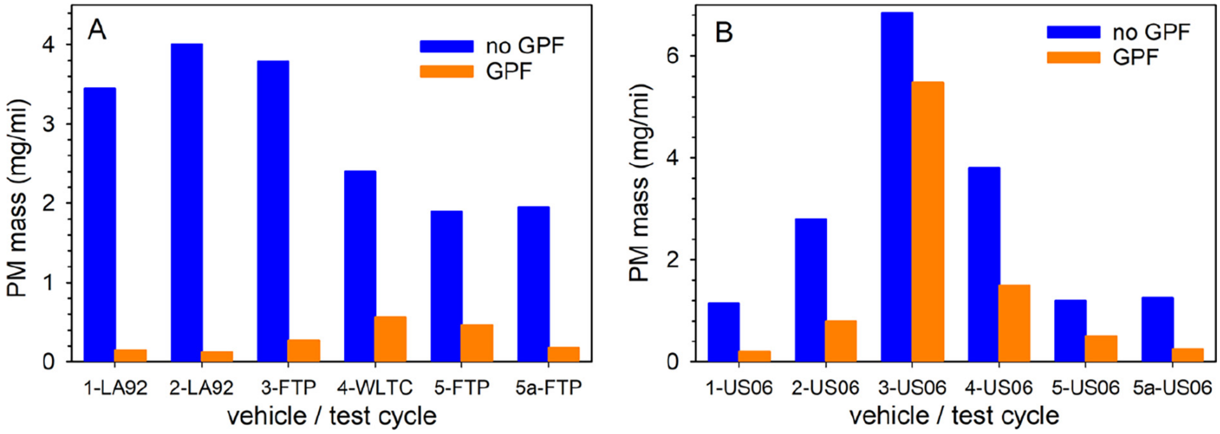

Fig. 39. GPF impact on GDI PM mass emissions. Panel A: "Normal" driving - LA92, WLTC, and FTP drive cycles. Panel B: "Aggressive" driving - US06 cycle. Data for vehicle 1 & 2 (Yang et al., 2018), vehicle 3 (Chan et al., 2016), vehicle 4 (underbody GPF, Jang et al., 2018), and vehicles 5&5a (bare and ash coated GPFs Liu et al., 2019).

four real world routes ranging from urban to altitude and found GPF filtration efficiencies of 44 % - 99 % for PM mass and solid number reductions, with no fuel economy penalty.

In a demonstration of extremely low PM emissions, Suarez-Bertoa et al. (2019) evaluated a 1.4 L OEM GPF equipped vehicle which maintained solid particle emissions below 1/10 of the standard, including particles <23 nm, over all laboratory and RDE testing. This is an important result given that EU7 standards lower the cutpoint from 23 nm to 10 nm. Going beyond RDE testing, Giechaskiel et al. (2022) measured emissions from a GPF equipped GDI vehicle over aggressive drive cycles, hard accelerations, high payload, "bad" fuel (PM index 2.2), and cold temperatures. The solid particle emissions remained below the EU6 limit, except for cold start tests at −9 °C. This condition produced large numbers of particles below 23 nm, which were attributed to semi-volatile particles that were in the gas phase at the GPF temperature. Although more data are required to ascertain GPF full useful life capabilities, the results from these studies are promising for GDI vehicles to meet extremely stringent PM emissions standards.

The main approach to GPF development has followed the ceramic honeycomb wall flow design used for DPFs and illustrated in Fig. 40 (Lambert et al., 2017a). Other filter media, such as metal fibers or metal foam, potentially offer a superior efficiency versus backpressure tradeoff (Ou et al., 2019; Myung et al., 2015), but it is difficult to package such media into filters that compete with the surface area offered by the honeycomb geometry. A high surface area is essential, because it reduces wall flow velocity, which increases filtration efficiency and lowers back pressure. Furthermore, wall flow filters can be constructed from cordierite, which is well suited for gasoline engine exhaust in terms of low thermal conductivity, low thermal mass, low thermal expansion and high thermal shock tolerance (Joshi and Johnson, 2018).

There are three main contributions to backpressure in honeycomb GPFs, namely contraction and expansion at the filter's inlet and outlet, channel friction, and wall permeability. Lambert et al. (2017a) developed a model using the Borda-Carnot equation to describe the contraction and expansion, Poiseuille's equation for channel friction and Darcy's law for the wall loss to examine the impact of various GPF parameters, such as filter length and diameter, wall thickness, and wall permeability, on backpressure. They find that, for clean high porosity filters, channel friction can exceed the wall flow resistance; thus, there is an optimum filter length, which balances the increase in channel friction against the reduction in wall losses as filter length increases. During use, filters collect soot and ash, which restricts flow through the wall and may lead to wall permeability dominating pressure loss through the filter. Raising wall surface area, e.g., via length or diameter, may have a larger impact on alleviating this backpressure than increasing the underlying wall permeability.

Pressure loss measurements by Aleksandrova et al. (2019) show that the flow regime in clean GPFs differs from DPFs, due to the flow rates and temperatures of gasoline engine exhaust and can transition to turbulent flow. Thus, they proposed a backpressure model that includes turbulent flow. Their approach reduces reliance on model parameters but reaches the same conclusion that channel friction can dominate flow resistance and, thus, that shorter, larger diameter filters may be preferable. Optimization of the inlet and outlet cones to the GPF also offers an opportunity to reduce backpressure and improve flow uniformity. Mu et al. (2019a, 2019b) examined cone design by experiment and simulation and found that it can reduce pressure drop by up to ~10 % and improve the particle deposition pattern within the filter.

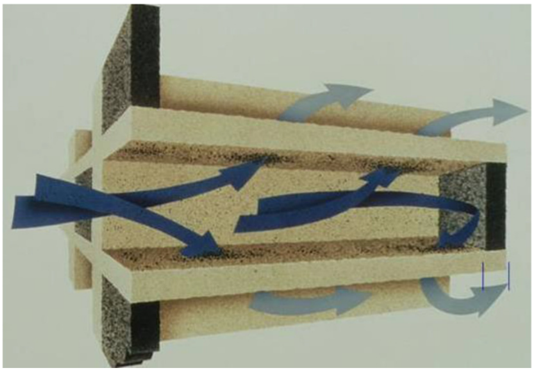

Fig. 40. Wall flow engine exhaust particulate filter (Courtesy Corning, Inc.).

GPF porosity and loading also impact filtration efficiency. In the submicron size range relevant to engine exhaust particles, filtration occurs via the three mechanisms depicted in Fig. 41A, namely diffusion, interception, and impaction (Hinds, 1999). Collection by diffusion occurs when particles deviate from flow streamlines due to Brownian motion and collide with the filter media, e.g., a fiber or pore wall. Since diffusion rate varies inversely with particle size, the efficiency of diffusion filtration increases for smaller particles, as shown by Fig. 41B. As the flow rate increases, there is less time for particles to diffuse to the media and filtration efficiency decreases.

Interception occurs when a particle along a streamline contacts the filter media. Thus, interception efficiency increases with particle size, but is independent of flow rate. Impaction occurs when a particle is unable to follow the streamline because of its momentum and collides with the filter media. This increases with particle momentum; thus, impaction efficiency increases with particle size and flow rate.

Impaction is nearly negligible for most exhaust particle sizes and flow conditions. As Fig. 41B shows, diffusion and interception combine to a net filtration efficiency that exhibits a minimum typically in the vicinity of 100 nm. Fig. 42 displays measured GPF efficiencies, which follow this net efficiency size trend. These are determined from the pre versus post GPF size distributions in Fig. 38, by integrating the size distributions over each test phase and calculating efficiency as one minus the ratio of pre to post GPF time integrated distributions.

Because pre and post GPF measurements were made on separate tests, small variations in instrument offsets introduce some uncertainty into the efficiency calculation in Fig. 42, particularly for the urban and hot start phases when particle concentrations are low. Nevertheless, the results confirm that diffusion is the dominant particle capture mechanism for engine exhaust particles, and they display the efficiency minimum between diffusion and interception mechanisms. The high filtration efficiency at small size in Figs. 41B and 42 explains why Chan et al. (2016) found similar GPF efficiencies with >3 nm and > 23 nm solid particle cutpoints, which was mentioned above.

Soot collected in a GPF must be removed to prevent eventual filter clogging. Stoichiometric gasoline engine exhaust normally contains too little oxygen and NO_2 after combustion for soot oxidation to take place in a GPF, even though the exhaust temperature is often suitably high. However, conditions with sufficient oxygen occur periodically in transient operation, such as fuel cuts during vehicle deceleration, when soot oxidation is feasible. Chan et al. (2016) observed decreases in GPF efficiency during the US06 cycle, as illustrated in Fig. 43A, and suspected that these arose from regeneration events. After instrumenting their test vehicle with oxygen sensors and thermocouples upstream and downstream of the GPF, they identified fuel cuts during the US06 test where the oxygen concentration decreased by >5 % across the GPF, but the outlet temperature did not track the inlet, and attribute this to regeneration. They suggest that only limited regeneration occurs over the FTP drive cycle, based on much lower, ~1 %, oxygen declines during FTP cycle fuel cuts.

Another demonstration of the feasibility for GPF regeneration during fuel cuts comes from the chassis dynamometer experiments by Rathod et al. (2018). They installed pre soot loaded GPFs on a 2.0 L GTDI vehicle, ramped the vehicle to high load, and initiated fuel cuts at a series of GPF temperatures. They infer regeneration from two observations. One is the difference in temperature profiles at the inlet versus rear plane of the GPF, illustrated in Fig. 43B. The inlet temperature immediately falls after the fuel cut, whereas the temperature at the rear continues to rise for an additional ~20 s owing to heat produced by soot oxidation. The second

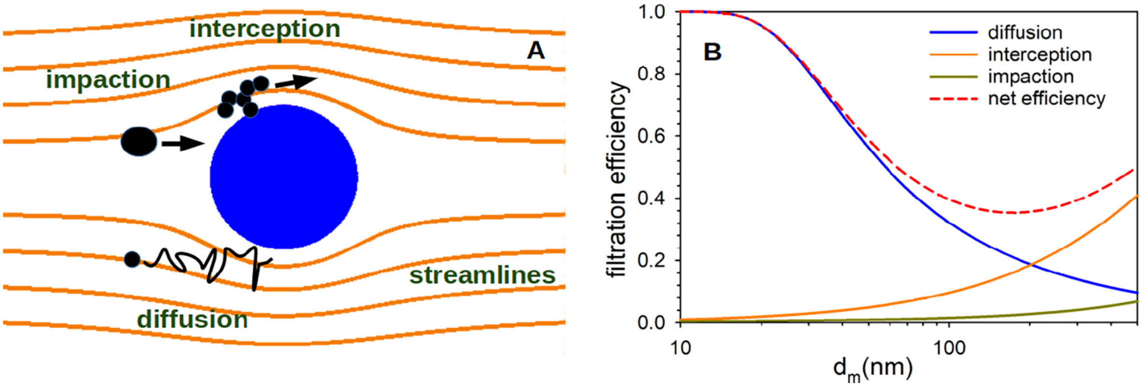

Fig. 41. Filtration mechanisms for particle flow around a barrier. Panel A: Schematic view of the three main mechanisms. Panel B: Generic size trend for each mechanism over the range relevant to engine PM (Hinds, 1999). Actual efficiency depends on flow rate, filter pore structure & surface area, and ash & soot loading.

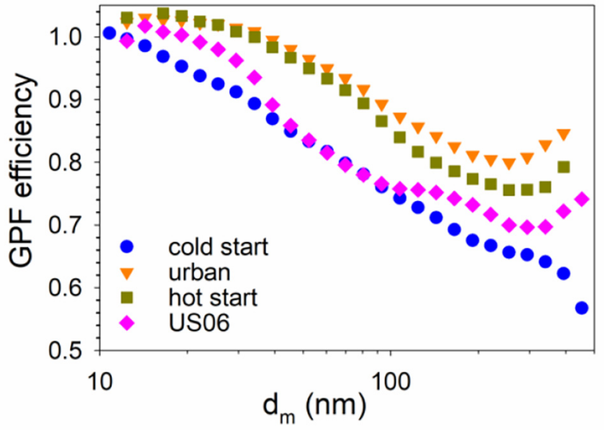

Fig. 42. Particle size dependent GPF efficiency. These are calculated from the pre and post GPF size distributions in Fig. 38.

observation is a small transient CO_2 increase at the GPF exit resulting from soot oxidation.

The above studies demonstrate that passive regeneration occurs in GPFs, but they do not show that this occurs often enough under real world driving conditions to prevent overloading the filter. To address this question, Boger et al. (2015) performed laboratory and vehicle tests with GPFs pre-loaded with Printex U (Degussa) as a surrogate soot to represent the least reactive component of engine out PM. Laboratory reactor measurements established the oxidation kinetics for the surrogate soot and recorded the oxidative capacity of simulated fuel cuts at various temperatures. The latter shows that a single 30 s oxygen pulse at 700 °C can oxidize 50–90 % of the surrogate soot, whereas at 500 °C 140 pulses of 40 s provide 18 % to 30 % regeneration, depending on GPF material. Pre-loaded GPFs that were driven on highway, rural, and city routes exhibit weight loss from soot oxidation when weighed at periodic intervals. As anticipated the weight loss is greater for the highway routes, but the city soot removal rates are high enough, though not conclusive, to suggest that passive regeneration may be sufficient to avoid GPF overloading during ordinary driving.

Yue et al. (2021) conducted a more comprehensive series of on-road tests in various cities in China with the expectation that the congested traffic conditions would provide challenging conditions for passive regeneration. They used temperature and soot accumulation models associated with the powertrain control module along with temperature sensors to record regeneration frequency during these on-road tests. Their results reveal that regeneration happens consistently at GPF temperatures above 600 °C and speeds >30 mph, and that this occurs frequently enough, even in congested traffic, to avoid excessive soot accumulation.

The soot cake that rapidly forms on the walls of DPFs determines efficiency. Because passive regeneration prevents soot cake formation, GPF performance depends on whether it is washcoated (the porous refractive oxide layer that carries the precious metals and oxygen storage compounds for TWC activity) and varies with the soot and ash loading. Lambert et al. (2017a) examined the impact of three washcoat loading levels on the performance of high porosity (>60 %) cordierite filters. When loaded at a typical production TWC level, the GPF backpressure caused warnings of excessive manifold pressure. GPFs loaded at half and one quarter of the TWC level had acceptable backpressure but were curiously found to exhibit lower filtration efficiency.

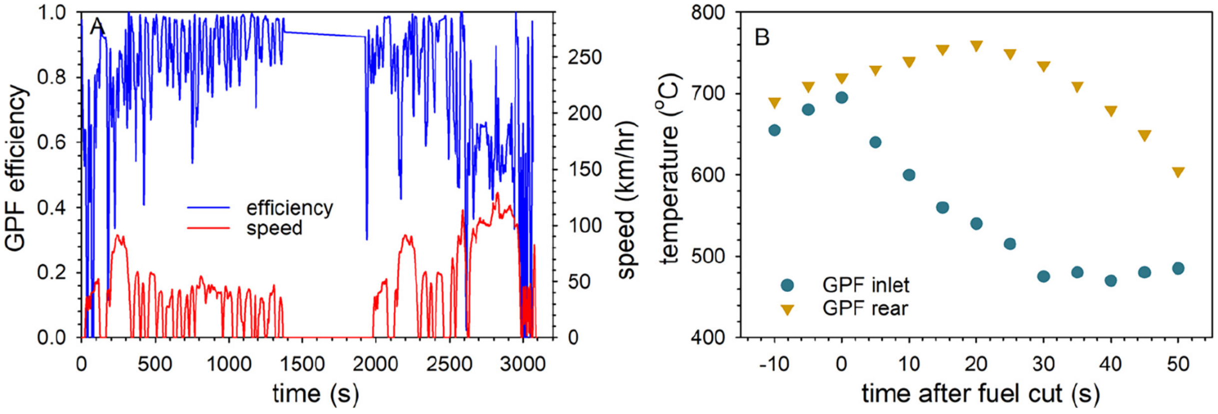

Fig. 43. GPF regeneration. Panel A: GPF efficiency decrease for times >2600 s during the US06 (from the data in Fig. 38). Panel B: GPF temperature increase after a fuel cut (Rathod et al., 2018).

Washcoat material choice introduces an additional factor. A study by Wang et al. (2020a) shows that using high bulk density powders to produce washcoats lowers their volume and reduces the backpressure penalty. They also examined the impact of where the washcoat is applied. They found that applying washcoat on both the inlet and outlet channel walls, but over only 50 % of the channel length, gives an optimum balance between PN filtration efficiency and backpressure, as compared to single sided or other coating patterns.

There have been many studies on ash accumulation in GPFs. Ash is a concern, because it reduces fuel economy and limits the full useful life of the filter. Lube oil additives are a major source of ash. These primarily enter the combustion chamber via oil droplets injected when a large pressure difference occurs between the combustion chamber and piston land and via oil mist transport though the PCV valve into the air intake (Wang et al., 2020b). Combustion converts metals and phosphorous in the additive into oxides. These nucleate and agglomerate with soot particles, which are then trapped by the filter. Regeneration removes the soot and leaves behind the ash. There is also a large non-oil contribution to GPF ash. Analysis of GPFs from two high mileage vehicles, >130 k miles, reveals that ~50 % of the ash derived from lube oil consumption. About 30 % of the ash originates from washcoat lost by the upstream TWC and the remainder is dominated by iron related to engine wear (Lambert et al., 2016).

Ash accumulates both along the inlet channel walls and in the plug area at the downstream end of the GPF. Lambert et al. (2016) find that about 2/3 of the ash deposits on the inlet walls and 1/3 in the plug region of their 150 k mile filter. Interestingly, the wall ash has a density of 1.6 g/cm^3, while the plug ash density is significantly lower at 0.7 g/cm3. Rubino et al. (2017) likewise report a homogeneous ash layer on the inlet channel walls after 200 k km of on-road vehicle operation and note that they see no penetration into the wall. A subsequent study by Lambert et al. (2017b) of ash deposition in GPFs with various aging reveals the formation of a “web-like” network on the inlet wall after 3000 km of on-road operation. Elemental mapping indicates that ash penetrated most of the way into the wall of one 3000 km GPF, but only slightly into the wall of another that had 60 % higher washcoat loading. The x-ray tomography study by Seong et al. (2019) shows an increase in the number of closed pores on the inlet walls of a bare GPF after ash loading, which results from ash partially penetrating into the wall. To complicate matters further, Shao et al. (2016) report that oil formulation chemistry affects ash loading; oils with Ca based detergents exhibit an earlier transition from deep bed filtration to formation of a surface layer than Mg based oils. The reasons for this remain unclear.

Washcoat loading and ash accumulation have contrasting impacts on GPF efficiency. Results from Liu et al. (2018) in Fig. 44 display a decrease in filtration efficiency between blank and washcoated filters, and a subsequent increase to above the blank filter efficiency after ash accumulation from 3000 km of on-road operation (trapped soot was removed by 1 h oxidation at 650 °C). This behavior is explained by the filtration mechanisms in Fig. 41. GDI engine exhaust particles typically peak in the 30–100 nm range. Diffusion is the principal capture mechanism at these sizes. Applying a washcoat to a filter closes some passages and narrows others, which shifts flow to the larger passages. The resulting increase in velocity through these passages reduces the time available for particle diffusion to the wall and, thereby, lowers capture efficiency. When ash accumulates in the GPF, some penetrates into the pores, but it also forms a dendritic network on the wall surface, such as seen in the SEM images in Lambert et al. (2017b) and in Fig. 45 below. This network is essentially a fiber filter in series with the wall filter, which raises the overall filtration efficiency.

The ability of a small ash layer to enhance GPF efficiency suggests a solution to the problem of low initial GPF filtration efficiency, namely apply an artificial fibrous ash layer in lieu of waiting for one to form during vehicle driving. This idea was previously evaluated by Zinola et al. (2013). Looking to mimic a soot cake, they coated and sintered ~20–50 mm SiC particles onto the inlet channel walls of a cordierite filter. This produced a thin packed bed on the surface, which increased filtration efficiency from about 87 % to 96 %.

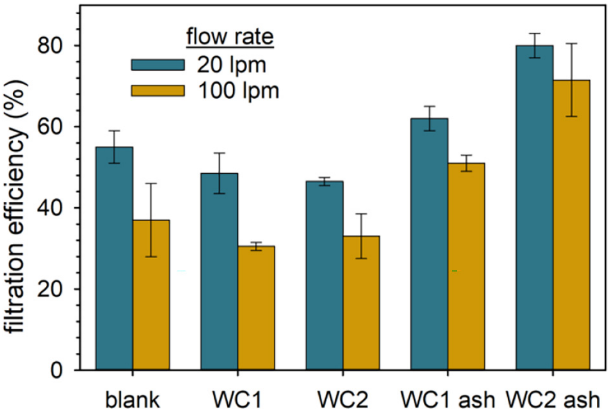

Fig. 44. Impact of flow rate, washcoat, and ash loading on GPF efficiency (Liu et al., 2018).

Liu et al. (2019) explored a different approach. They atomize an alumina suspension to produce an aerosol of spherical, ~80 nm, alumina particles, and flow this through the GPF substrate. These particles are captured by diffusion and, while some undoubtedly reach the deep bed, others over time form a fibrous network across the wall surface, as displayed by the SEM images in Fig. 45. The addition of alumina decreases wall permeability from 2.5 mm^2 for the blank filter to 0.8 mm^2 at 1.2 g/L loading, which raises backpressure by 220 % to 5 kPa.

The effect of the artificial ash layer on filtration efficiency in these experiments is shown in Fig. 46. Even low loading substantially improves efficiency; 0.7 g/L of alumina raises efficiency from ~60 % to 85 % at 80 nm, which is a typical size for engine exhaust soot. The improvement carries over to on-vehicle performance. Loading a GPF with 1.5 g/L alumina raises PM mass filtration efficiency over the FTP drive cycle from 75 % to 90 % and US06 cycle efficiency from 59 % to 80 %.

Much work remains to improve methods to apply a fiber filter over the inlet walls of a honeycomb substrate, develop a manufacturing process to accomplish this, and ensure full useful life reliability of the product. The interaction between an artificial ash, or other, membrane and the washcoat of a coated filter also needs to be studied. However, this is a promising approach that is worth pursuing, since it allows use of high porosity substrates, and the low backpressure penalties these present, without the drawback of low initial filtration efficiency and the variability in efficiency associated with the state of soot and ash accumulation.

5.2. Role of the three-way catalyst

There are in principle three mechanisms by which a TWC can remove particles from the engine exhaust stream. One is by direct trapping and subsequent catalytic oxidation of particles. The second is by catalytic conversion of hydrocarbon precursors of primary organic aerosol (POA). This is particulate matter formed by nucleation or condensation of low volatility exhaust species onto existing particles as vehicle exhaust is diluted and cooled prior to sample collection onto filters for gravimetric mass measurement. The third is catalytic removal of secondary organic aerosol precursors. These are emitted in the gas phase or as POA that later evaporates as vehicle exhaust disperses, but in either case are subsequently oxidized to aerosol in the atmosphere.

A few studies of TWC impact on particle emissions found significant reductions in the 5–30 nm range but disagree on accumulation mode particles. Whelan et al. (2013) report a 90 % reduction in 5–23 nm particles but increases of 40 % to 109 % across the TWC for particles above 50 nm. Bogarra et al. (2017) find a roughly order of magnitude drop in particle number at all sizes across the TWC during engine start, but this removal efficiency quickly declines. After 80 s of engine operation there is a ~ 60 % reduction in <20 nm particles, no effect on 20–50 nm particles, and almost complete removal of particles >100 nm. Results from

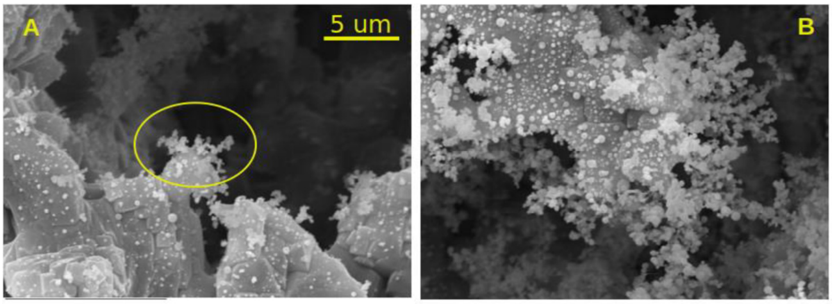

Fig. 45. SEM images of artificial ash on a cordierite wall flow substrate. Panel A: 1 g/L alumina loading. Panel B: 5 g/L alumina. The circled area highlights ash dendrites beginning to grow. These form a more extensive fiberous network at higher loading in panel B. (Images courtesy of X. Liu, Ford Motor Co.).

steady state testing by Liu et al. (2021) are similar; they report TWC removal efficiencies of 30 % - 80 % for 5–30 nm and for >200 nm particles, but much lower efficiency at sizes in between. The studies present observations, but do not give a clear explanation of the removal mechanisms.

Direct removal of particles by a TWC requires that particles contact the walls during flow through the substrate. Thus, the mechanisms in Fig. 41 for GPF particle capture apply also to TWC efficiency in either case that the particle is oxidized or indefinitely trapped. Since the TWC is essentially a coated GPF without end plugs, its capture efficiency can be no better than a GPFs. This leaves diffusion as the primary mechanism for capturing 5–30 nm particles, as also discussed in Bogarra et al. (2017) and Liu et al. (2021).

Diffusion during flow through the TWC channels, simplified here as cylindrical tubes, depends on the dimensionless deposition parameter $\mu = DL/Q$, where D is the particle diffusion constant, L is the TWC length and Q is the volume flow rate through a single channel. For laminar flow, which applies to most exhaust flows, penetration through a tube is given by (Hinds, 1999).

$$P = 1–5.50\ \mu^{2/3} + 3.77\ \mu \quad \text{for } \mu < 0.009$$

$$P = 0.819\ e^{-11.5\mu} + 0.0975\ e^{-70.1\mu} \quad \text{for } \mu \geq 0.009$$

Based on Liu et al.'s (2021) L = 0.2 m catalyst length, 60 cells/cm^2 cell density, 600 °C average exhaust temperature, and 70–170 m^3/h exhaust flow (assumed reported at 20 °C), the efficiency for diffusion particle capture in their TWC is 1 - P = 8 % to 4 % for 10 nm particles and 18 % to 10 % at 5 nm with increasing flow. Thus, the TWC does make a small to modest contribution to filtration at the small size end of GDI particles, but it is considerably less than reported in the above GPF studies.

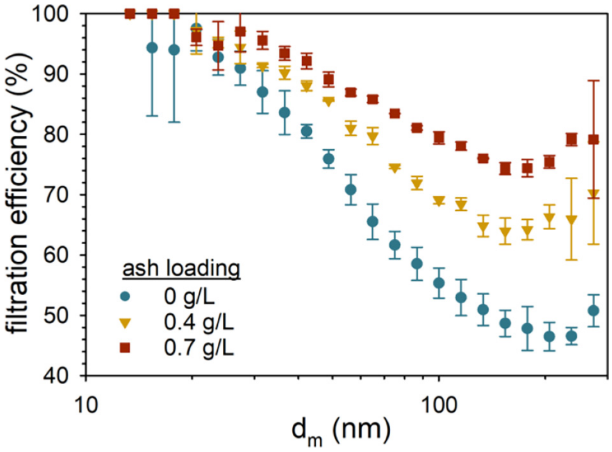

Fig. 46. GPF filtration efficiency for a bare wall flow filter and for two levels of ash coated filter (Liu et al., 2019).

One suspects that the remainder of the observed particle number reduction downstream of the TWC results from catalytic conversion of POA precursors. The size distributions recorded by Whelan et al. (2013), Bogarra et al. (2017), and Liu et al. (2021) exhibit substantial nucleation modes at 5–30 nm. Their experimental procedures used heated sample lines (58–190 °C) and in some cases heated dilution (190 °C) but did not take the standard steps to ensure removal of semivolatile particles; for example, their temperatures were far lower than the 350 °C minimum stipulated in the EU solid particle measurement procedure and lacked an evaporation tube or catalytic stripper (Giechaskiel et al., 2021). Thus, these nucleation modes potentially include a significant contribution from low volatility HCs, which decreases across the TWC. In this case, TWC removal of small particles observed in these studies is real but occurs mainly by removing HCs that later form particles rather than removing the particles themselves (He et al., 2010; Zinola et al., 2013; Liu et al., 2020).

The removal of particles >200 nm reported in these studies approach the efficiency of clean GPFs. This seems unreasonably high given that particles are not forced to flow through the substrate wall in a TWC. The size range above 200 nm lies in the tail of the GDI PM size distribution, where the signal to noise is low; thus, systematic uncertainties, such as instrument drift between pre and post TWC measurements (sometimes performed on different days), may explain these anomalously high efficiencies. In other studies, particle increases in this size range have also been reported post TWC but ascribed to measurement uncertainty (He et al., 2010).

The period between engine cold start and the end of catalyst warmup represents a special case. At engine start the catalyst is cold; thus, thermophoresis becomes another possible mechanism for particle removal. However, thermophoresis is rather insensitive to size over the 5–500 nm range of engine exhaust particles (Hinds, 1999) and, therefore, is inconsistent with size dependence observed for the difference in particle concentrations before versus after the TWC (Whelan et al., 2013; Bogarra et al., 2017). This suggests that thermophoresis is limited to a small role. A cold catalyst is also subject to water condensation, but how this affects exhaust particle concentrations is unknown.

The catalyst also plays an important role in the potential for SOA formation from engine exhaust. There have been many investigations of this process; examples include Odum et al. (1997), Robinson et al. (2007), Bahreini et al. (2012), Gordon et al. (2014b), Karjalainen et al. (2016), Gentner et al. (2017) and Platt et al. (2017). These studies generally show that atmospheric oxidation of organic precursors emitted in the exhaust yields secondary PM that exceeds primary emissions. The atmosphere is an oxidative environment. Sunlight photolytically produces radical species, such as the OH radical. These react with hydrocarbons emitted into the atmosphere initiating a sequence of chemical reactions, which convert HCs to aldehydes, organic acids, and eventually CO_2 (Seinfeld and Pandis, 2016). Small HCs tend to fragment in this process, but large HCs and aromatics follow more complex reaction pathways that can create highly oxygenated species that have very low vapor pressures and partition into the aerosol phase. This secondary aerosol adds to the overall atmospheric PM burden of motor vehicles.

Studies that examine GPF impact on SOA formation are really looking at the effect of the catalytic coating, or lack thereof if a bare filter is used. Pieber et al. (2018) compared SOA formation from standard and GPF retrofitted GDI vehicles. SOA formation from the standard vehicles is dominated by the cold start. The major precursors are benzene, toluene, xylenes, ethylbenzene, and C3-benzenes. SOA formation is 20–50 times lower during the hot running phases of the WLTC and NEDC drive cycles, consistent with precursor removal by a warmed-up TWC. GPF retrofitting had no effect on SOA formation, either during the cold start or warmed-up operation. The bare filters have no catalytic activity to remove precursors, and in the underbody position the catalyst coated GPF added little to the close coupled TWC.

A catalyst's ability to oxidize HCs is important to limit SOA formation, but its performance in NO_x reduction also affects secondary aerosol formation. Fig. 47 compares primary and primary plus secondary PM from two GDI vehicles run over the LA92 drive cycle with and without catalyzed GPFs retrofitted in the underbody location (Roth et al., 2019). Without GPFs, PM emissions are ~75 % black carbon and ~ 25 % POA. The catalyzed GPFs reduce primary PM emissions by >95 % to well below 1 mg/mi, with POA as the main constituent.

Besides SOA, photochemical aging produces ammonium nitrate and other inorganic salts from the ammonia formed in the TWC and the NO_x that remains downstream. This is considerably larger for vehicle 2, due to its nearly 7-fold higher tailpipe NO_x and likely higher NH_3 emissions compared to vehicle 1. Adding a GPF to vehicle 1 reduces SOA formation but increases ammonium and ammonium nitrate levels. The authors believe that the latter increases are exaggerated by the use of lower exhaust dilution when testing vehicle 1 with the GPF, and that the true aged PM emission rate is lower than reported. Retrofitting vehicle 2 led to a substantial reduction in photochemically aged PM, likely due to the fact that the catalyzed GPF reduced NO_x emissions by a factor of ~8 relative to the original aftertreatment configuration. Thus, catalytic NO_x reduction lowers secondary aerosol formation if it is converted to N_2 but can exacerbate the impact of vehicle exhaust on ambient PM when NO_x is converted to NH_3.

5.3. Summary of PM control by gasoline vehicle exhaust aftertreatment

When thinking about the effectiveness of exhaust aftertreatment it is useful to keep in mind that the ~400–800 °C environment in the exhaust system of a gasoline vehicle is vastly different from a test cell dilution tunnel or the real-world atmosphere. Particulate matter at exhaust temperatures consists primarily of soot agglomerates, with some ash and perhaps some high boiling and partially pyrolyzed organic species. The large majority of primary organic aerosol and secondary organic aerosol precursors are in the gas phase. A GPF mechanically removes solid matter, but not gas phase species. The latter are removed by a catalyst, either TWC or active washcoat in a GPF.

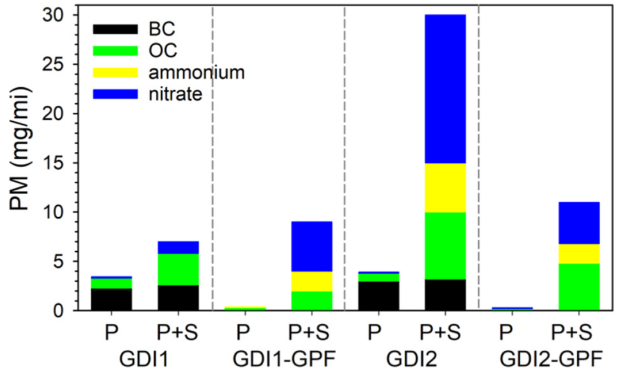

Fig. 47. GPF impact on primary and secondary (photochemically aged) PM emissions from two GDI vehicles (Roth et al., 2019).

GPF technology has evolved a great deal from its diesel counterpart. GPFs operate in a higher temperature and lower soot flux environment. They need to exhibit low backpressure so as not to offset the fuel economy improvement offered by GDI engines, yet have high initial filtration efficiency, since passive regeneration prevents formation of a soot cake on the GPF channel walls. High porosity cordierite substrates have been developed which introduce an imperceptible impact on fuel economy over most driving conditions. Initial tests of OEM GDI vehicles with GPFs show that they can meet the EU solid particle number limit over dynamometer driven regulatory drive cycles as well as on-road RDE testing.

GPF efficiency is affected by soot loading and ash accumulation. Soot loading adds a degree of variability to GPF filtration efficiency and backpressure since its level changes from passive regeneration that depends on exhaust temperature and oxygen availability. Even low amounts of ash accumulation over a few thousand kilometers can improve efficiency with minor impact on backpressure. Work is currently ongoing to develop artificial ash or other membrane technology to design this effect into the GPF instead of relying on accumulation over vehicle operation.

The TWC also reduces gasoline vehicle PM emissions, both primary and secondary. Fig. 48 summarizes the declines in POA emissions and SOA formation from gasoline vehicle exhaust across progressively stringent emissions standards. These results are from a comprehensive evaluation of emissions from 16 light duty gasoline vehicles from California's in-use fleet (Saliba et al., 2017; Zhao et al., 2018). They reveal roughly exponential declines in POA and SOA emissions factors for vehicles meeting certification standards from pre-low emitting vehicle (pre-LEV) to super ultralow emitting vehicle (SULEV). These declines correlate with similar reductions in non-methane organic gas (NMOG). Within vehicle-to-vehicle variability, SOA formation is the same for PFI and GDI vehicles, even though GDI primary PM emissions are typically higher, again reflecting the fact that SOA reductions are a function of catalyst, and not GPF, efficiency.

6. Fuel and lube oil impacts on PM

Gasoline vehicle soot emissions arise largely from liquid fuel films and incompletely evaporated fuel droplets. However, fuels are not created equal. Some contain more low volatility components than others. These fuels have lower droplet evaporation rates, increased fuel impingement, and slower evaporation of fuel films from combustion chamber surfaces. Fuel composition also affects the propensity for soot production by pyrolysis or diffusion combustion. Thus, in addition to engine technology refinements, such as combustion chamber and injection system design, adjustments in fuel composition can help lower gasoline engine PM emissions. This section begins with a look at methods used to rate a fuel's impact on PM emissions. It then examines the effects of fuel and lube oil compositions on gasoline vehicle PM emissions, injector fouling, and GPF performance.

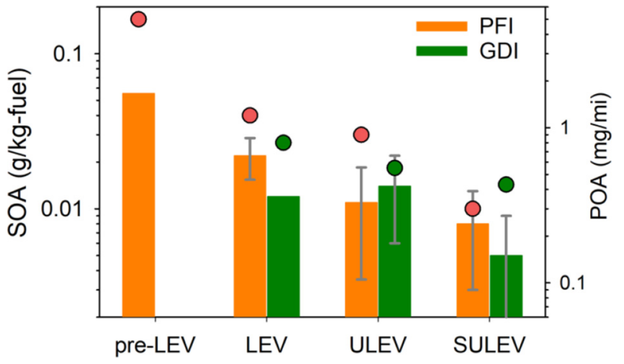

Fig. 48. Gasoline vehicle exhaust POA emissions (circles) and SOA formation (bars) across vehicle certification standards (Saliba et al., 2017, Zhao et al., 2018).

6.1. Fuel PM indices

Understanding soot formation is central to combustion processes. A variety of methods have been developed to rank sooting propensity. Smoke point is one that has received extensive use; for example, it is the basis for ASTM D1322 used to characterize aviation fuels. Smoke point is the flame height at which a diffusion flame transitions from non-sooting to sooting. Fig. 49 compares an 85 % ethanol in gasoline (E85) flame below its smoke point to E50 and E0 flames that are above. An increase in fuel flow lengthens the flame. This increases residence time, which promotes soot formation. But it also speeds up radiative cooling, which lowers the soot oxidation rate. At a threshold fuel flow, and associated flame height, soot formation exceeds its oxidation and the flame transitions into the sooting regime (Santoro et al., 1987).

Smoke point scales inversely with fuel sooting propensity; thus, in Fig. 49, the lower sooting E85 fuel has a higher smoke point than E50 and E0. Since smoke point is apparatus dependent, it is usually converted into the "Threshold sooting index" (TSI), defined as TSI $= a\cdot\mathrm{MW}/h + b$, where h is the flame height at the smoke point, MW is the fuel molecular weight, and a and b are constants determined by calibration with two reference fuels (Calcote and Manos, 1983). An additional benefit is that the TSI for a hydrocarbon fuel blend is the mole fraction weighted sum of its values for each component (Gill and Olson, 1984).

Another approach to soot propensity is the "Yield sooting index" introduced by McEnally and Pfefferle (2007a). This method measures the incremental soot volume fraction when a methane air diffusion flame is doped with a minute fraction of a test compound and standardizes it to a YSI value in the same manner as TSI. In contrast to smoke point, soot volume fraction increases with sooting propensity, which makes this approach more suitable to differentiate between highly sooting fuels. It also decouples soot chemistry from physical flame parameters, since flame temperature, residence time, radical concentrations, etc. are determined by the methane - air flame and, thus, are independent of the test fuel.

An internal combustion engine sooting index is more complicated because the propensity for soot formation in an engine depends on a fuel's tendencies to form both liquid films and produce soot. The first effort was by Aikawa et al. (2010) who proposed the "Particulate matter index" (PMI) defined by

$$\mathrm{PMI} = \sum_i \mathrm{wt}_i \frac{\mathrm{DBE}_i + 1}{\mathrm{VP}_i}$$

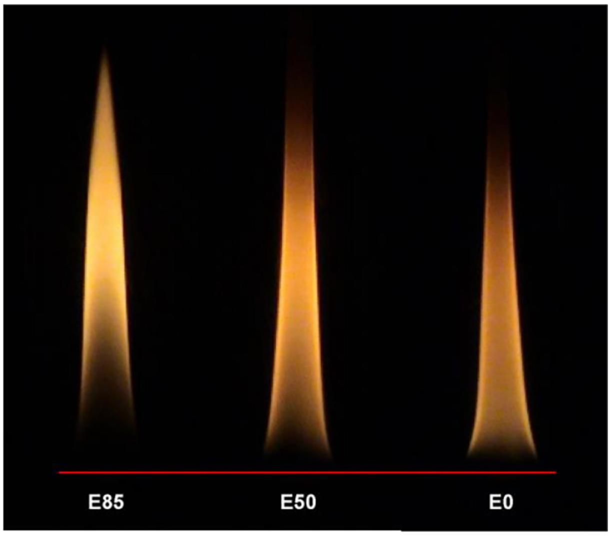

Fig. 49. Comparison of non-sooting (85 % ethanol in gasoline) and sooting (50 % and 0 % ethanol in gasoline) diffusion flames.

Here, $DBE_i = ½\,(2C_i - H_i + 2)$ is the double bond equivalent and C_i and H_i are the numbers of carbon and hydrogen atoms in species i, VP_i is its vapor pressure at 443 K, wt_i is its weight fraction, and i extends over all species in a given fuel. This index differs from the TSI and YSI indices described above. TSI and YSI are based on measured flame properties directly related to soot. In contrast, PMI is an empirical expression based on selected properties of the individual fuel components.

Considering its simplicity and lack of adjustable parameters, PMI has done surprisingly well in correlating hydrocarbon fuels with gasoline vehicle PM emissions (Crawford and Lyons, 2019). Fig. 50 illustrates this for a GDI vehicle tested with 10 fuels. The goodness in fit likely arises for two reasons. One is that DBE and vapor pressure directionally capture the two key aspects of PM formation; DBE_i, which increases from alkanes to alkenes to aromatics, serves as a surrogate for the sooting propensity of species i, while inverse vapor pressure correlates with its propensity to form a fuel film. The second is that by speciating the fuel, these are applied to each fuel component rather than to an average fuel species that may not represent well a fuel's PM forming propensity. The fit to solid PN is better than PM mass likely because of lower measurement uncertainty and, because it is insensitive to semivolatile material that is not directly related to soot formation in the engine.

A variety of alternative indices have been suggested to improve PMI with respect to accuracy, inclusion of oxygenates, avoiding fuel speciation, and particle number emissions (Chapman et al., 2016; Leach et al., 2017). There are currently ~16 indices according to a recent review that describes them in detail (Leach et al., 2022). These fall into two general categories: 1) fuel speciation-based indices and 2) those based on bulk fuel properties.

The latter approach has the allure of simplicity. Bulk measures, such as TSI and YSI, exist to capture the sooting tendency of a composite fuel. Unfortunately, species that contribute most to fuel volatility or vapor pressure have little correlation with those that produce soot, which makes it difficult to construct an accurate index from bulk fuel properties (Barrientos et al., 2016). Still, progress is being made in this direction. Fatouraie et al. (2018) identified the C_{9+} fuel aromatic content as a surrogate for sooting tendency, oxygen content as a measure of ethanol effect, and heat of vaporization, final boiling point, and fraction evaporated at 90 °C to describe liquid film propensity. They used these fuel properties to develop a regression model, which describes well the 6-fold variation in PN emissions over their test fuels.

PM emissions indices determined by speciating the fuel perform well in ranking hydrocarbon fuels, but markedly less so with oxygenated fuels (Crawford and Lyons, 2019). This is especially concerning given the current preponderance of E10 gasoline in the market. Performance declines primarily because adding oxygen functionality to HC molecules introduces abrupt changes in sooting propensity and evaporation trends. In fact, Crawford and Lyons (2019) identified an ethanol bias when applying PMI to a vehicle's emissions across a mixed set of gasoline and ethanol blended gasoline

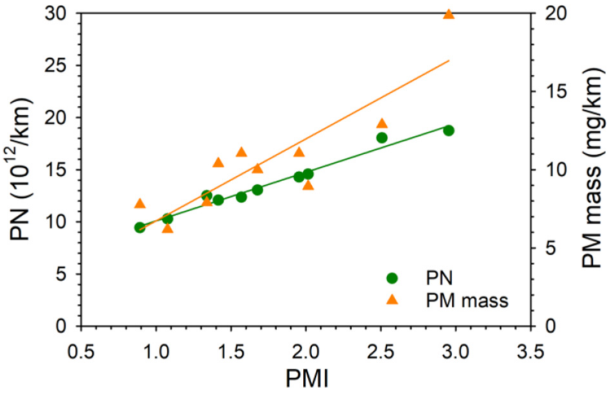

Fig. 50. Solid PN and PM mass emissions versus particulate matter index (PMI). Data are from a 2.4 L naturally aspirated GDI vehicle run over the FTP cold start phase for a set of 10 fuels (Aikawa and Jetter, 2014).

fuels; experimental PM emissions were consistently higher for E10 - E20 fuels, and lower for E0 fuels, than predicted by PMI.

A concern with PM indices is they are generally based on small, disparate data sets. This was addressed by Crawford and Lyons (2019) in an evaluation that combined fuel dependent PM emissions data from three in-depth studies: two from the Coordinating Research Council (Morgan et al. 2017 & 2018) and one from the U.S. EPA (U.S. Environmental Protection Agency, 2013; Butler et al., 2015). During their evaluation of various PM indices against these data sets, Crawford et al. (2021) developed a refinement of PMI, labeled the "Particulate matter emissions" index (PME):

$$\mathrm{PME}=\left(\frac{43.4}{\mathrm{LHV}}\right)\left(N_T\sum_i \mathrm{wt}_i\frac{Y_i}{\mathrm{VP}_i^{\alpha}}\right)^{\beta}$$

Y_i is related to sooting tendency, LHV is the lower heating value of the fuel, N_T varies between PFI and GDI engine technologies, α varies with ethanol level, and β is an additional fitting parameter. The main improvements are the generalization of the vapor pressure term to account for ethanol effects and the replacement of DBEs with sooting propensites $Y_{i.}$ Since YSI values are not available for many species identified in detailed hydrocarbon analyses (DHA) of gasoline fuels, the propensities are derived from statistical extrapolation of YSI values reported in the literature. PME removes the ethanol bias and provides an index that can be used across a range of ethanol blended fuels, but there are a couple of caveats: it requires fuels to have the same Reid vapor pressure (RVP) and it cannot currently be used to guide ethanol blending for achieving PM emissions reductions (Crawford et al., 2021).

The better performing PM emissions indices are based on detailed fuel speciation. These show aromatic components as the main contributors to PM formation, 69 % - 83 % of PMI in the study by Hoekman and Khlystov (2022). C_{10} - C_{12} aromatics are the major source within this group. Unidentified compounds are the second largest contributors to PMI in many fuels, which has prompted efforts to extend DHA capability (Lubkowitz and Meneghini, 2018). However, the the speciation of complex HC mixtures introduces an element of variability into the determination of PMI that needs to be taken into account when defining the DHA method.

Fig. 51 displays PMIs calculated for 8 fuels from DHAs performed by 10 laboratories (Hoekman and Khlystov, 2022). The average PMI across laboratories varies between 1 and 2.3 for the 8 fuels. However, the ±2σ inter laboratory uncertainty extends over most of this range for 6 of the 8 fuels. The data show that the differences are laboratory, and not fuel, related; high and low PMI values are consistently associated with specific laboratories across all fuels. Thus, the lab-to-lab variability originates from their DHA procedures as opposed to random measurement errors. Consequently, fuel-speciated PM indices provide a more useful comparative metric when the fuels under consideration are all analyzed by the same laboratory. However, it is difficult to compare PM indices between different fuel effects studies owing to the large inter laboratory DHA uncertainties. Broader applicability of speciated PM indices requires improved DHA procedures more than extending them to increasingly low concentration fuel species.

6.2. Fuel impact on PM emissions

A great deal of effort has been spent on investigating the impact of ethanol blended gasoline fuels on PM emissions (e.g., Maricq et al., 2012; Sakai and Rothamer, 2019; Yang et al., 2019a, 2019b). This was prompted by the Renewable Fuel Standard, which originated with the Energy Policy Act of 2005 and accelerated the transition from gasoline to the E10 gasoline that presently dominates the U.S. market. Ethanol alters gasoline properties in many ways, including changes to the distillation curve, higher vapor pressure, and an increase in octane rating. High ethanol fractions lead to PM reductions, but the results for E10 and E15 are mixed, with some studies showing reductions and others PM increases. This has led to considerable debate about how fuels are formulated, what are the key fuel properties related to PM emissions, and the role that ethanol plays in these properties (see reviews by Clark et al., 2019, 2021).

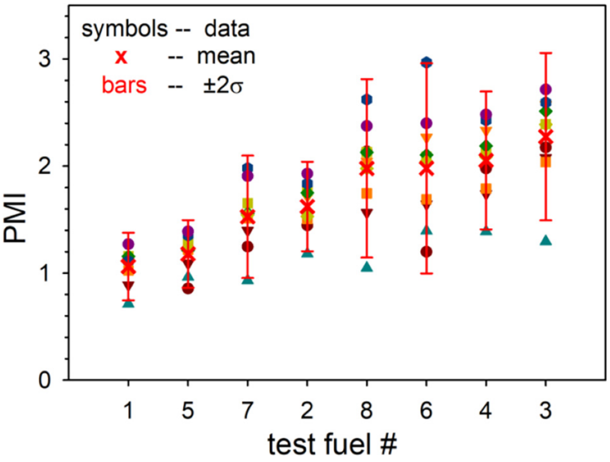

Fig. 51. PMI variability from laboratory differences in detailed HC analysis (Hoekman and Khlystov, 2022).

Ethanol's chemical role in soot formation can be explored via its impact in flames. Premixed ethylene flames exhibit nearly linear declines in soot volume fraction with the addition of 5 % - 20 % ethanol. The effect weakens with increasing equivalence ratio; thus, 10 % ethanol reduces soot by 50 % at $\Phi = 2.01$ versus 17 % at $\Phi = 2.64$ (Salamanca et al., 2012). Chemical models suggest that ethanol is about 50 % less able to contribute carbon to form soot precursors than the ethylene that it displaces (Wu et al., 2006). In contrast, adding 10 % ethanol to ethylene in non-premixed flames increases the maximum soot volume fraction (McEnally and Pfefferle, 2007b). In this study, ethanol decomposes more readily than ethylene to form methyl radical, which enhances reaction pathways to aromatics and, thereby, soot. Ethylene is, however, a special case; larger HCs, such as those in gasoline, decompose more easily to methyl radical, and so are less sensitive to this soot enhancement. Reductions in acetylene and benzene formation observed upon ethanol addition to propane diffusion flames seem to corroborate this assessment (Rubino and Thomson, 1999).

While perhaps not in all flames, ethanol does suppress soot formation in gasoline diffusion flames (Khosousi et al., 2015). As shown by the inset to Fig. 52, the inverse smoke point (1/SP) of a gasoline - ethanol mixture decreases nearly linearly with the volume fraction of ethanol added. Any ethanol contribution to methyl radical soot formation pathways is presumably outweighed by its dilution of aromatic and other higher sooting gasoline components. The vehicle and engine PM emissions displayed in the main figure parallel the 1/SP trend. PM emissions from three GDI vehicles, normalized to E10, and a GDI engine, normalized to E0, decline by roughly half for circa E35 gasoline, and by a factor of ~5 for E85.

Ascertaining ethanol's influence in the practically relevant E10 gasoline proves more difficult. First, extrapolation from Fig. 52 suggests that the effect should be small, 10–20 %, which makes it difficult to measure in vehicle exhaust meeting Tier 2 / 3 standards. The second question is which species in gasoline does ethanol displace? That is, is the E10 splash blended (ethanol added to base fuel), match blended (produced at refinery to specifications), or a market fuel? The third issue is that ethanol also alters gasoline volatility and its distillation curve, which affect fuel evaporation; thus, the sooting propensity noted in flames might not be the determining factor in engines.

An example of measurement uncertainties comes from the CRC E-94-1 project, which found a 20–51 % PM emissions increase for the three-vehicle test fleet between tests with E0 fuel at the beginning versus the end of the project (Morgan et al., 2014). Overcoming such issues requires careful test procedures and a significant database of vehicles and repeat tests. Suitable data sets have been achieved in a few cases, notably the EPAct (U.S. Environmental Protection Agency, 2013, Butler et al., 2015)

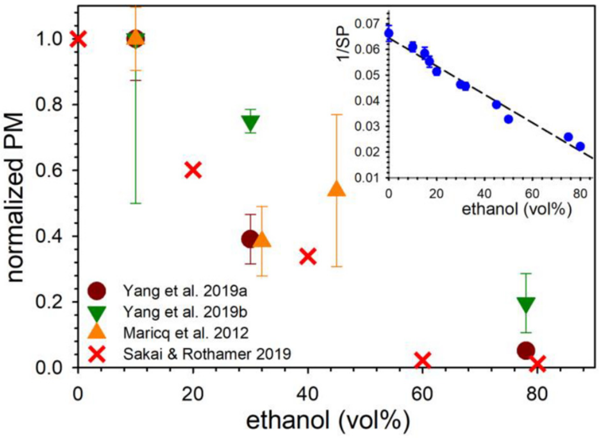

Fig. 52. Reduction in PM emissions with high ethanol - gasoline blends. Emissions are normalized to E0 /E10 fuel. Inset: Inverse smoke point versus ethanol fraction (Barrientos et al., 2016).

and CRC E-94-2 studies (Morgan et al., 2017). The E-94-2 study reveals a roughly 20–50 % increase in PM emissions for E10 versus E0 gasoline over the LA92 drive cycle, consistent with the EPAct results. The fuels in both studies were match blended, meaning that the base fuel composition was altered in ways beyond ethanol addition to maintain select fuel properties, including octane rating, T50, T90, PMI, and aromatic content. In contrast, splash blending alters most fuel properties, for example increasing octane and diluting aromatics. The CRC E-94-3 project compared splash blended to the earlier match blended fuels and found that the former supported an increase in PM emissions from E10 gasoline (Morgan et al., 2018).

The question then is: what causes the PM increase? The opposite ethanol trend displayed by gasoline diffusion flame soot suggests that increased engine emissions arise from fuel evaporation effects, rather than sooting propensity. Chen et al. (2018) and Ratcliff et al. (2019) propose an explanation that cooling by ethanol's latent heat of vaporization lowers the evaporation rates of aromatics, which increases soot produced via their pyrolysis and diffusion combustion. The correlation between PM emissions and fuel droplet aromatic content in Fig. 53A supports this mechanism. The data come from steady state engine measurements using fuels doped with cumene and 4-t-butyltoluene. An evaporation model estimates the aromatic composition of fuel droplets 9 ms after injection. Scaling the droplet aromatic content by the corresponding YSI values correlates well with exhaust PM concentrations.

A fuel study by Yang et al. (2019c) into the combined effects of ethanol and aromatics on PM emissions corroborates the idea that the PM increase from E10 may be due to an interaction between these two fuel components. Fig. 53B displays the relationship between C_{10+} aromatic fuel content and PM emissions. The data fall into two groups: those with 20 % versus 30 % aromatic volume fraction. A roughly 40 % increase in C_{10+} aromatics between these two fuel groups leads to a ~ 2-fold rise in PM emissions that overrides any effects by ethanol level. Within each group, increasing ethanol raises PM emissions, although there is some uncertainty within the 20 % aromatics group. In particular, the 30 % aromatics fuels exhibit an increase in PM emissions with ethanol content, even though the C_{10+} concentration decreases. This suggests an interplay between heavy aromatic and ethanol fuel components in which ethanol's evaporative cooling can offset declining aromatic content and lead to a net increase in PM emissions.

The picture that emerges is that low level ethanol blends increase exhaust PM emissions due to reduced evaporation of high soot propensity gasoline components, whereas high level blends reduce PM by dilution of these species. The ethanol question may be important for air quality and fuel policy decisions, but the impact on gasoline vehicle technology improvements to reduce PM emissions is minimal. The vehicles in the EPAct and CRC E-94 studies are now a decade old. Auto manufacturers have been making progress on reducing PM emissions to below Tier 3 / LEV III standards using E10 certification fuel, which already has a higher PM forming propensity than the older E0 fuel. Meeting real world emissions targets, such as RDE requirements, rely on market fuels. Here, variations in other fuel properties, such as aromatic content, outweigh the effects of ethanol. Design and technology innovations that improve PM emissions robustness to fuel variability, therefore, become important objectives.

6.3. Lube oil impact on PM emissions

Gasoline vehicle PM emissions are often associated with lube oil; the image of blue smoke emanating from an old poorly maintained vehicle comes to mind. However, there is little information about the role of lube oil in current technology gasoline vehicles. Kleeman et al. (2008) used hopanes and PAHs as oil and gasoline tracers to source apportion PM emissions from a fleet of 24 LEV and pre-LEV PFI gasoline vehicles. The results indicate that fuel contributes the majority of elemental carbon PM emissions, but that both fuel and lube oil contribute to the organic carbon fraction. Oil was the dominant PM source for vehicles emitting visible smoke.

More recently, Pirjola et al. (2015) compared PM emissions from a turbocharged GDI vehicle run with five different lube oil formulations. Lubricant choice affected both cold start and hot running operation, primarily

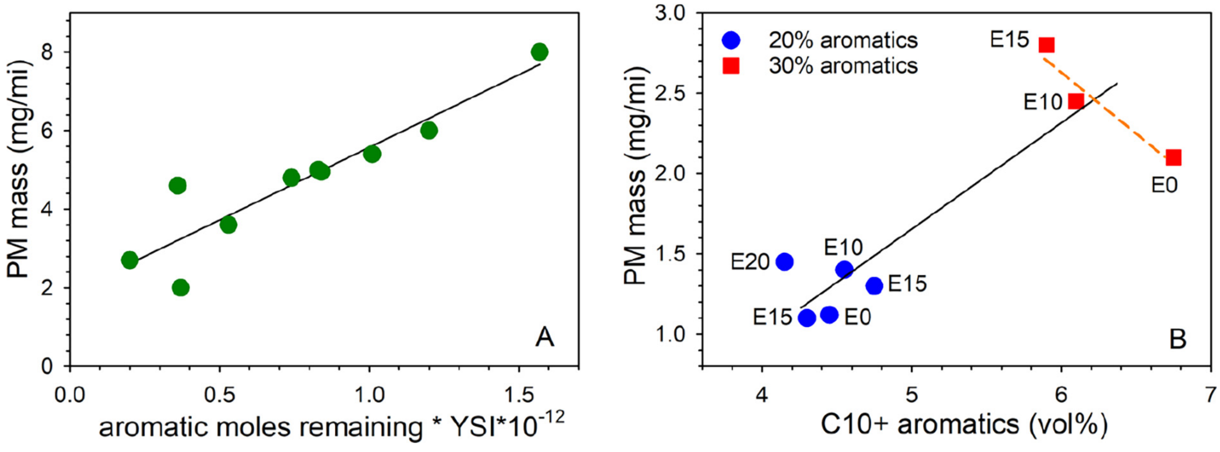

Fig. 53. Aromatics impact on PM emissions. Panel A: Association between droplet evaporation and PM mass emissions (Ratcliff et al., 2019). Panel B: Effects of C_{10+} aromatics versus ethanol content (Yang et al., 2019c). Solid line shows aromatics trend; dashed line depicts ethanol trend.

during acceleration and steady state driving. Oils with greater metal content produced the highest PM emissions; a 10 % reduction in Zn content lowered non-volatile PN by ~12 %. The reduction in volatile particles was larger, about 20 %, consistent with Kleeman et al.'s (2008) finding that oil made a significant contribution to the OC fraction of PM.

Premnath et al. (2018) examined lube oil effects on PM emissions from a GDI vehicle at the cusp of meeting the 2025 LEV III 1 mg/mi standard and found similar results. FTP weighted average emissions dropped by ~20 % from 1.1 mg/mi for a 1.43 % sulfated ash, high volatility, oil to 0.9 mg/mi for a 0.7 % ash, low volatility, oil. Solid particle and ash particle numbers exhibited similar declines. As generally is the case, the cold start dominates PM emissions in this study; urban and hot start phase emissions are 2.4 times lower by gravimetric mass and ~ 25 times lower by size distribution measurements. Soot comprises about 60 % of the cold start emissions by mass and 75 % by particle number, which indicates that fuel derived elemental carbon remains the main PM component even at the ~1 mg/mi emissions rate.

The existence of GDI vehicles that achieve ~1 mg/mi PM emissions, and PFI vehicles with emissions at half this level, implies the ability to engineer vehicles with low levels of lube oil related PM emissions. Auto manufacturers have two reasons besides low PM to reduce oil consumption: namely, improved catalyst function and higher customer satisfaction. Zinc and phosphorous in lube oil poison catalysts (Rokosz et al., 2001). Tighter piston tolerances and the development of filters to recover the oil mist from crankcase vapors (Golkarfard et al., 2019) have increased the typical oil change interval from 3000 to 10,000 miles. This reduces catalyst poisoning and, thereby, precious metal costs, is a customer benefit, and presumably lowers the lube oil contribution to PM emissions.

It remains unclear how universal lower oil consumption is. Consumer Reports has compiled a list of 2010+ model year gasoline vehicles that need an additional quart of oil between oil change intervals (Preston, 2021). Even if this has decreased as a new vehicle issue, there remain concerns that oil consumption and oil derived PM emissions increase with vehicle age. The example in Fig. 54 demonstrates that current technology is available to engineer GDI vehicles with low PM emissions for full useful life. In this very small sample, two vehicles maintain ~3 mg/mi PM emissions over 150 k miles. The extent to which this applies to the gasoline vehicle fleet remains an open question.

6.4. Fuel & lube oil effects on injector deposits

Besides their direct contribution to PM formation, fuel and lube oil also play indirect roles in PM emissions rates via their effects on injector tip deposits and GPF performance. Depth profiling of GDI injector deposits by Edney et al. (2021) indicates that they consist primarily of fuel derived PAHs and progressively dehydrogenated carbonaceous species. Lubricating oil components are found as impurities in the deposits but are not a main contributor (Dearn et al., 2014; Edney et al., 2021). This is consistent with earlier work that associated deposit formation with aromatic and olefin fuel components (Ashida et al., 2001; Carlisle et al., 2001). Organo-sulfur compounds, as well as peroxides that form in aged oil are also associated with deposit formation and are used as additives for accelerated injector fouling (Shanahan et al., 2017; Barker et al., 2019).

These fuel species can accelerate deposit formation and increase the injector tip contribution to PM emissions. Recently, Zhang et al. (2020) performed a fuel study of injector fouling on an engine test bench. They compared a base China gasoline with fuels blended to increase aromatic content, heavy aromatics, and olefins, respectively, in terms of injector performance and PN emissions. Over the course of the fouling tests, the flow rates of initially clean injectors decreased and the engine PN emissions increased, reaching steady states after 30–60 h. Fig. 55 displays the percentage difference between these steady state and initial flow rates and PN emissions. The fuel impacts on injector fuel flow and PN emissions track each other; aromatics have the biggest impact, followed by olefins. Thus, aromatics impact PM emissions both through their contribution to fuel PMI and to injector tip deposit formation.

T90 is another fuel property associated with deposit formation. There are two reasons for this: one is related to flash boiling and the other to the deposit formation mechanism. Flash boiling exacerbates tip wetting; thus, a higher T90 extends the injector operating range to higher temperature before the onset of flash boiling. According to the model of Kinoshita et al. (1999), a wetted tip contains unevaporated fuel and suspended non-volatile deposit precursors. If the fuel does not completely evaporate, the next injection flushes the tip and suppresses deposit formation. If it does, the precursors attach to the tip and grow the deposit. Zhang et al. (2020) added heavy ends to their C_{9+} high aromatic fuel to increase T90 to 182 °C and found that this alleviated the reduction in injector fuel flow and the increase in PN emissions observed with the original C_{9+} fuel (see Fig. 55). This is consistent with Imaoka et al. (2019), who compared three fuels with different T90s and found both injector tip associated PN and total PN to decrease with increasing T90; however, they did not discuss any other fuel differences or how these may have impacted emissions.

Higher T90 is generally associated with higher PMI owing to the presumably lower droplet and fuel film evaporation rates of the high boiling fuel components. This reasoning applies also to fuel condensed on the injector tip; thus, from this perspective a lower T90 reduces PM emissions. However, a lower T90 also exacerbates flash boiling, which increases tip wetting. If this additional wetting exceeds the benefit of faster evaporation, the net result will be higher PM emissions. In this way, it is possible that T90 can have the opposite effect on PM formation from the injector tip versus piston impingement.

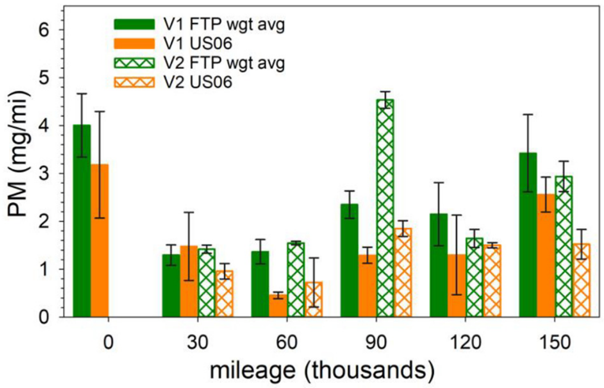

Fig. 54. FTP weighted average and US06 PM mass emissions for two 2010 GTDI vehicles over full useful life (Maricq et al., 2013).

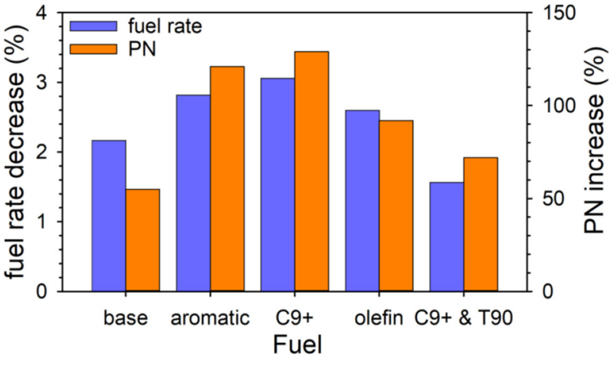

Fig. 55. Fuel impact on the loss of fuel flow rate and increase in PN emissions due to injector fouling (Zhang et al., 2020). “Aromatics” has 9.4 % more small, lower than C_9, aromatics than the base fuel. “C9+” has 8.1 % higher C_9+ aromatics, “olefins” has 6.4 % higher olefin content, and “C9+ & T90” is the “C_9+” fuel with additional heavy components to increase T90 from 165 to 182 °C.

6.5. Fuel & lube oil effects on GPFs

Fuel and oil composition both impact GPF performance. Moses-DeBusk et al. (2020) performed a detailed comparison of GPF soot oxidation for gasoline and alcohol - gasoline blended fuels. They found that soot collected from a GDI engine run on E30 fuel exhibits significantly higher oxidation reactivity than soot from the base E0 gasoline, whereas soots from 24 and 48 % isobutanol blends show progressively lower reactivity. These results corroborate previous reports that ethanol blending lowers the activation energy of soot produced by GDI engines (Luo et al., 2015).

A deeper look into the oxidation of GPF collected soot reveals that it depends on the soot's thermal history, its exposure to oxygen and water vapor, and its location in the GPF (Moses-DeBusk et al., 2020). Furthermore, the oxidation kinetics vary during GPF regeneration. E30 soot has a lower activation energy for oxidation than E0 soot, but both increase as soot is oxidized. E30 soot activation energy increases from 67 to 120 kJ/mol as soot burnout progresses from 0 to 50 %, whereas E0 soot activation energy varies from 82 to 140 kJ/mol over the same range. The thickness of the soot layer along GPF channel walls decreases faster near the GPF inlet and more slowly at the rear; however, the variation in in-wall soot burnout rate along the GPF length is not known.

This behavior is not unexpected. Soot from combustion is not pure carbon; it includes small fractions of hydrogen and oxygen that vary with fuel, combustion conditions, and the post combustion temperature history. Over time, soot undergoes carbonization and oxidation to lose hydrogen and oxygen, respectively, at rates that increase with temperature (Dobbins, 2002). For comparison, the activation energy for oxidation of particles produced in an ethylene diffusion flame was found to be 164 kJ/mol (Higgins et al., 2002), which coincides with the E0 soot activation energy reported at 80 % burnout.

As discussed in Section 5, ash from lube oil can improve GPF performance. Owing to the generally high temperature of gasoline engine exhaust and periodic availability of oxygen, a soot cake does not form on GPF walls, but its role in raising filtration efficiency is instead taken up by ash deposition. Besides laboratory measurements, this has been verified in a field study that employed nine new 1.4 L turbocharged GDI vehicles meeting China 5 emissions regulations (Zhang et al., 2019). The vehicles were retrofitted with GPFs and run with three lubricating oils, which had 0.79, 0.87, and 1.32 % mass sulfated ash, but were otherwise similar. The results show faster ash accumulation in the GPF as oil ash levels increase, along with concomitant increases in GPF backpressure and filtration efficiency. Although ash improves GPF performance, the real-world concern is that it is not controlled, but instead depends on oil formulation and vehicle operating history. Thus, a better approach is to design a GPF that includes ash layer functionality to begin with, and to employ low ash oils in the field to maintain this functionality over full useful life.

6.6. Summary - fuel and lube oil impact on PM emissions

Fuel and lubricating oil composition play both direct and indirect roles in gasoline vehicle PM emissions. Inorganic elements in fuel and oil additives lead to ash particles, but the main source of PM emissions is the soot produced by rich combustion and pyrolysis of poorly mixed fuel and fugitive oil. The amount of soot produced depends on the propensities of various fuel components to form liquid fuel films and the propensity for these films to soot. Fuel based PM indices that account for both propensities generally provide useful indicators of relative PM emissions across different non-oxygenated gasoline formulations.

Including oxygenates makes it more difficult to identify a good PM index. Introducing oxygen functional groups into hydrocarbon compounds interferes with the trends in HC volatility and sooting tendency with HC size and structure. Extending indices to include oxygenates, therefore, generally involves introduction of additional parameters that have less physical and chemical basis than sooting and film forming propensity surrogates, such as DBE and volatility, typically used for HC fuels. These extended indices can perform well and serve a useful purpose in summarizing emissions data for a matrix of fuels but are less reliable for extrapolation outside of the matrix.

Ethanol is an interesting example of how oxygenates can disrupt HC fuel trends. At ~10 % levels its combustion pathways can increase sooting tendency, but its main impact on gasoline engine PM emissions is indirect; its evaporative cooling of highly sooting fuel components, such as heavy aromatics, outweighs its dilution of these compounds relative to the base gasoline. This suggests that concern about ethanol blend fuels increasing the light duty fleet PM emissions is better directed at the heavy aromatic components than ethanol. As illustrated by Fig. 53, the direct benefit of reducing heavy aromatics in gasoline outweighs ethanol's indirect disbenefit in 10 % to 20 % ethanol gasoline-blends. A full assessment of ethanol's benefits also needs to include the impacts on greenhouse gas emissions and the agricultural industry.

Lube oil contributions to PM in properly designed gasoline vehicles should be minimal. This is evident from GDI and PFI vehicles that meet or exceed 1 mg/mi and roughly equivalent $6{\cdot}10^{11}$ solid particle/km emissions standards. It is also consistent with efforts to lower lube oil ash catalyst poisoning and increase oil change intervals. However, there are indications that this may not hold in practice across the light duty fleet.

Fuel and lube oil contribute indirectly to PM emission via injector tip deposits and GPF impact. Fuel components, such as aromatics, that contribute highly to a fuel's PM index generally also exacerbate tip deposit growth. However, fuel physical properties can have an opposite effect on tip deposits than they do on PM indices. Flash boiling is an important enabler of deposit formation; thus, fuels with a high T90 tend to mitigate deposit growth, whereas they exacerbate soot formation in the combustion chamber.

Fuel and lube oil impact on GPFs is more performance than PM emissions related. Lube oil ash can improve GPF efficiency, but it is preferable to engineer this into the filters and not rely on oil consumption. Fuel composition can affect soot oxidation rates and, thereby, GPF regeneration. Thus far it does not appear soot reactivity is a limiting factor for passive GPF regeneration, but this is a potential concern to keep in mind.

7. Non-tailpipe PM emissions

Motor vehicle PM emissions have historically been synonymous with engine exhaust. As exhaust PM levels have declined, other vehicle sources, namely brake and tire wear debris, have become relatively more important. In addition, road wear and resuspended road dust are often included as “non-tailpipe” PM. Fig. 56 provides a rough overview of how these contributions to total motor vehicle PM emissions have changed over time. Whereas engine exhaust constituted about 60 % of the total in the United Kingdom in 2000, it is projected to dwindle to <10 % by 2030 (Ntziachristos and Boulter, 2013; Lewis et al., 2019). The situation is similar in the U.S. The average brake emissions from a recent 6 vehicle study, accounting for the fraction of ~0.66 that escapes from the vehicle, are ~6 mg/mi (U.S. Environmental Protection Agency, 2021d), while light duty vehicle tire emissions are estimated by MOVES2014 at 10 mg/mi (U.S. Environmental Protection Agency, 2014). These are comparable to the Tier 2 /LEV II 10 mg/mi tailpipe standard, but roughly an order of magnitude larger than the upcoming 2025 LEV III 1 mg/mi standard.

Non-exhaust PM has thus far been unregulated; however, newly proposed EU 7 emissions regulations include limits on brake and tire wear emissions (EU Commission, 2022). A PM_{10} brake particle mass standard of 7 mg/km is proposed to begin in 2025 and then fall to 3 mg/km starting in 2035. Tire wear emissions standards as well as brake and tire PM measurement procedures remain to be finalized.

Brake and tire wear PM are very different from the chemically formed fractal-like soot particles and condensed semivolatile organics that constitute tailpipe PM. Brake and tire particles are primarily generated by abrasion under most normal driving conditions, a physical process that generates micron size particles. The chemical composition of these is essentially the same as the parent materials, i.e., brake pads & rotors and tires. In extreme situations, brake and tire temperatures can

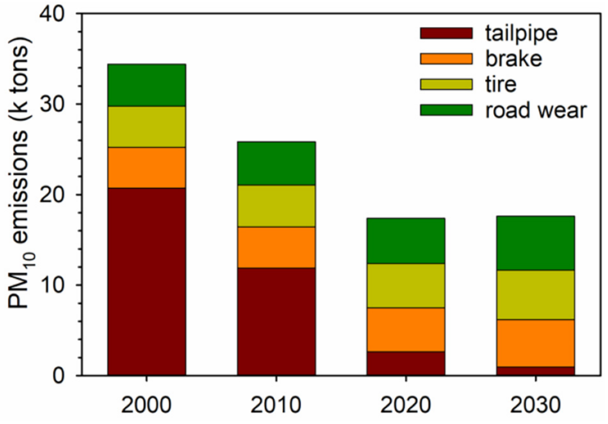

Fig. 56. Changes in tailpipe versus non-tailpipe motor vehicle PM emissions over time in the United Kingdom (Lewis et al., 2019).

rise above their respective smoke points and pyrolytically generate submicron particles, such as seen from smoking brakes or tires. Under these conditions, brake and tire wear have a bimodal distribution, with a submicron mode of 10–500 nm smoke particles and a coarse mode of 1–20 μm wear particles.

The pathways by which brake and tire wear particles enter the environment also differ vastly from engine exhaust PM. The latter is emitted via the tailpipe, a local source that can easily be connected to a dilution tunnel sampling system. Brake and tire emissions come from four non-localized sources. Brake particles must furthermore escape the wheel well, for example passing through the wheel cover, to enter the atmosphere. Tire wear depends not only on vehicle operating conditions, but also on road surface characteristics. Consequently, recording motor vehicle brake and tire wear emissions is significantly more complex than engine exhaust PM.

7.1. Brake wear PM

Brake PM emissions can be conceptualized as taking place in two steps: 1) particle generation and 2) particle escape into the environment. The first step is straightforward to measure; the second is complicated by the complex airflow patterns around the wheel and brake assembly. In principle, brake particle generation can be measured by a simple laboratory apparatus, as illustrated schematically in Fig. 57. The rotor and pads are installed in an enclosure, with the rotor connected via drive shaft to an external motor. Clean air flows past the brake assembly and out through a tunnel. A portion of this flow is sampled for particle measurements.

In practice, several factors need careful consideration. The enclosure must be designed to allow sufficient air flow to capture brake particles but minimize turbulence. The length of the tunnel needs to be long enough for good mixing, but short enough to mitigate gravitational settling of large particles. Isokinetic sampling is required to avoid size biases caused by air velocity differences between tunnel and sample probe. Finally, sample line design needs to avoid impaction losses of large particles through bends and gravitational losses through long horizontal sections. An early adaptation of a commercial brake dynamometer demonstrated the feasibility of this approach, with 70–90 % collection of brake PM relative to the mass lost by rotor and pads (Sanders et al., 2003). Improved brake dynamometers specifically designed for particle emissions measurement have recently appeared (Mamakos et al., 2019; zum Hagen et al., 2019a; U.S. Environmental Protection Agency, 2021d) and are being studied for possible regulatory application in the EU (Grigoratos et al., 2020).

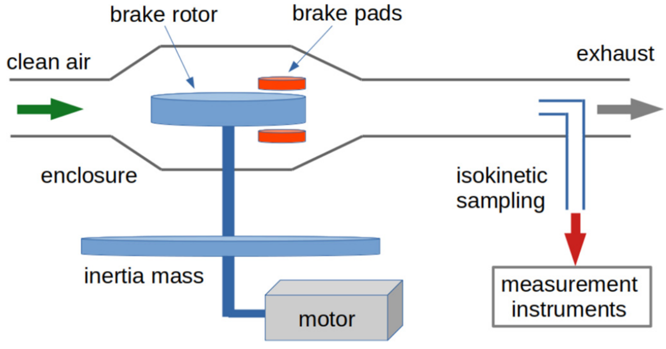

Fig. 57. Schematic diagram of brake dynamometer and sampling system.

Brake PM arises from abrasion and heat caused by compressive forces between brake pads and rotor when brakes are applied. This depends on four parameters: initial rotor speed, initial rotor temperature, pad pressure against rotor, and braking time. Initial temperature varies with the strength of and time since the previous braking event. The latter two parameters derive from the desired deceleration rate and final vehicle speed. These vehicle dependent parameters can be recorded by instrumenting a test vehicle and operating it over the desired drive cycle (Sanders et al., 2003). These are subsequently replayed on the brake dynamometer to reproduce brake wear generation during the drive.

Fig. 58 illustrates brake wear PM generated over stops that occur in the FTP drive cycle, along with vehicle speed prior to each brake event. The largest emissions correlate with initial speed, but because initial brake temperature and deceleration rate also play roles, this correlation does not hold for all stops. The brake wear size distributions in this example are unimodal and extend between 0.5 and 10 μm, with a number weighted peak in the 1–2 mm range. The stops in the FTP cycle are relatively mild and not severe enough to produce significant quantities of sub-micron smoke particles.

At the opposite extreme is the Auto Motor und Sport magazine (AMS) test, a series of ten 7.9 m/s^2 stops from 100 to 0 km/h performed in succession as quickly as possible. Brake particles emitted in this test are very different, as Fig. 59 shows. The stops are identical in terms of initial speed and deceleration rate, but there is a steep increase in particle number that correlates with a rise in initial brake temperature as the test progresses. Most particles in this test fall into the <0.5 mm range. Supra micron particles are emitted at an increasing rate throughout the test at concentrations comparable to and higher than those in Fig. 58 but are not visible due to the vertical scale magnitude in Fig. 59. Cumulative heating by the repetitive high speed decelerations increases brake rotor and pad temperature to the point where binders in the brake linings begin to pyrolyze. The combination of smoke and low volatility organics that nucleate produces a large number of particles in a size range similar to engine exhaust PM.

Neither the FTP cycle nor the AMS test is representative of real-world driving. Longer more sophisticated cycles have been developed to replicate a much broader range of braking and to serve emissions inventory purposes (Mathissen et al., 2018; Perricone et al., 2019; U.S. Environmental Protection Agency, 2021d). Brake temperature is an important consideration in designing braking cycles and measuring brake PM. Several studies

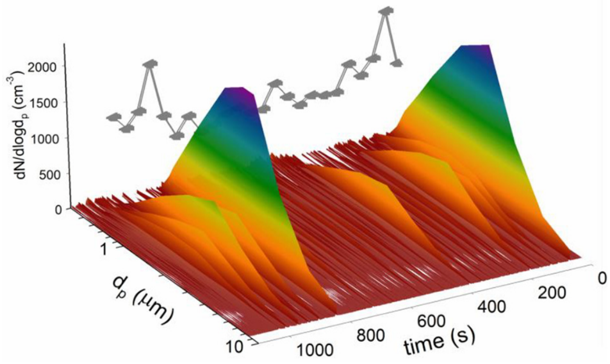

Fig. 58. Brake wear PM emissions during brake events taken from the FTP drive cycle. Symbols display vehicle speed at the start of each braking event. The two highest speeds are 89 km/h (Maricq unpublished).

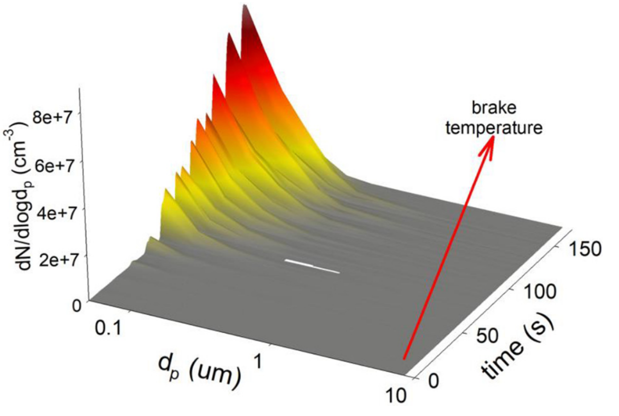

Fig. 59. Brake PM emissions over a rapid series of identical 7.9 m/s^2 stops from 100 to 0 km/h. Brake temperature increases from 25 to 500–600 °C over the test (Maricq unpublished).

have identified a transition temperature of 140–190 °C, above which a sharp, orders of magnitude, increase in submicron particles occurs, such as seen in Fig. 59 (Alemani et al., 2016; zum Hagen et al., 2019a; Niemann et al., 2020). Because of this temperature effect, care must be taken during sampling to ensure proper ventilation of the brake assembly so that the measurement process does not affect brake emissions (zum Hagen et al., 2019b).

There are several possible approaches to reduce brake PM emissions. One is the selection of friction material for brake pads, including non-asbestos organic (NAO), low metallic, and ceramic. These differ in various performance characteristics such as wear resistance, fade, noise, and brake dust. NAO liners replaced asbestos brakes as the latter were phased out. They are quieter than low metallic pads but are more prone to fade. They also produce significantly less wear debris, as demonstrated in Fig. 60. This result is consistent with a recent study by Woo et al. (2022), which reports similar ~4 times lower emissions from NAO versus low metallic liners. Ceramic brake pads can lower PM emissions even further, but have drawbacks of heat dissipation, ambient temperature limitations, and cost. Besides environmental concerns, high wear rates are undesirable, because the dust discolors wheel covers, which results in customer dissatisfaction.

Rotors provide two avenues to reduce brake PM. One is by improving wear resistance. A simple approach is to heat treat the standard cast iron rotor, which can lower PM_{10} emissions by 32 % using the same pad formulation (Perricone et al., 2018). Altering rotor surface morphology can also increase wear resistance. Cai et al. (2020) produced a dimple induced interlocking surface by plasma electrolytic aluminating, which helps establish a thin protective transfer layer that reduces wear. Larger emissions reductions are achieved with tungsten carbide coated and carbon-ceramic rotors. Hesse et al. (2021) measured 55 % and 70 % reductions in PM emissions over the WLTP braking cycle, respectively, for these two rotor designs relative to cast iron. A recent review describes other coating options that may help reduce PM emissions (Aranke et al., 2019). Coated rotors also offer another potential benefit, namely weight reduction. Since brake PM increases strongly with temperature, the second avenue for PM reductions is to improve the rotor's ability to dissipate heat away from the brake pads. Improvements can come from a combination of materials selection, rotor design, and airflow design.

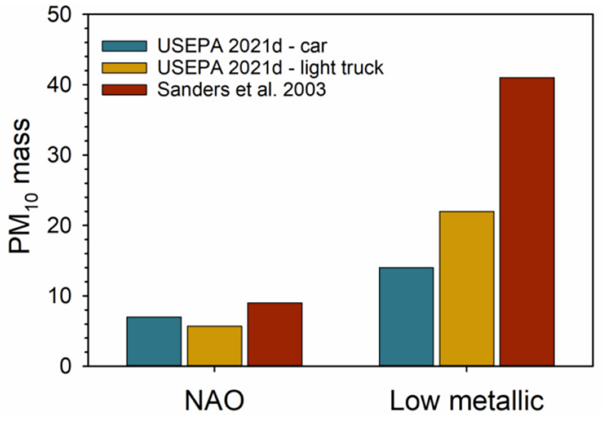

Fig. 60. Comparison of brake wear PM_{10} emissions rates from non-asbestos organic (NAO) versus low metallic pad formulations.

As might be expected, vehicle weight affects brake PM emissions. When weight increases, brakes need to dissipate more kinetic energy for the same stop, some of which goes into heat and some into abrasion. Measurements of brake wear PM from vehicles of different weights suggest a linear increase in wear rates with weight (U.S. Environmental Protection Agency, 2021d; Oroumiyeh and Zhu, 2021), but other differences between brake systems likely affect such comparisons. Another approach is to test the same vehicle at different weights. Fig. 61 shows a consistent increase in brake wear emissions after additional weight is added to two test vehicles. Reducing vehicle weight, therefore, has the dual benefits of lowering brake PM emissions and improving fuel economy.

Regenerative braking also offers an attractive combination to improve fuel economy and reduce brake wear emissions. It can capture up to approximately 60–70 % of braking kinetic energy (Toll, 2018) but can be a much lower ~8 % for hard stops from 60 to 0 mph (Jung, 2020). Reductions in brake wear PM are likely intermediate between these fractions and, thus, significant (Rakov, 2020; Jamadar and Jadhav, 2021). A possible downside is that any vehicle weight increase from the electric drive system will raise brake wear, tire wear, and resuspended road dust, which may offset regeneration benefits to some extent (Timmers and Achten, 2018; Beddows and Harrison, 2021).

The possibility of trapping brake wear particles is also receiving attention. One approach machines a groove into the trailing edge of the brake pad. The groove has an inlet to allow air to enter, and an outlet connected through a filter to a pump. As wear debris moves between the rotor and pads, it falls into the groove before it can escape the pad - rotor interface and is swept into the filter. Hascoët and Adamczak (2020) report 80–85 % number based trapping efficiency from bench testing a production brake assembly over varying braking cycles. The design has the advantage that it does not alter the air flow around the wheel, which plays an important role controlling brake temperature. The disadvantages are that it introduces additional hardware that needs maintenance, e.g., cleaning the filter, and may need on-board diagnostic monitoring.

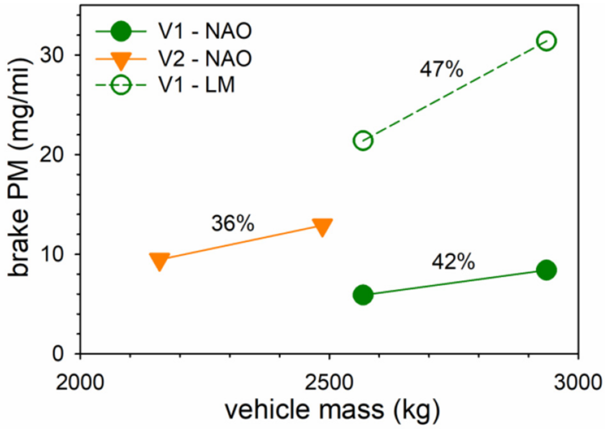

Fig. 61. Effect of vehicle mass on brake PM_{10} emissions (U.S. Environmental Protection Agency, 2021d). Each vehicle is tested at two weights. NAO = original equipment non-asbestos organic liner. LM = aftermarket low metallic liner. Labels indicate percent increases in emissions.

7.2. Tire wear, road wear, and resuspended road dust

The interaction between tire and roadway leads to three inextricably linked sources of particulate matter emissions: tire wear, road wear, and resuspended road dust. In principle, tire and road wear can be distinguished by their chemical characteristics, although in practice this is complicated by the fact that real-world tire wear particles are typically encrusted with road dust during abrasion (Dall'Osto et al., 2014; Sommer et al., 2018). Neither can easily be distinguished from resuspended road dust, since this contains previously generated tire and road wear that has deposited on the road. Collectively, the three sources depend on a great many factors. Road dust is location dependent, since it varies with traffic activity and meteorology. Tire and road abrasion depend on road material, road surface characteristics, road temperature, tire composition, tire construction, tire thread depth, tire pressure, tire temperature, vehicle weight, vehicle linear and angular velocity, vehicle linear and angular acceleration, and weather, among others (Panko et al., 2018).

Owing to the large number of factors involved, it is not surprising that reported tire emissions rates and particle size distributions vary widely. Tire and road wear particles are predominantly larger than 10 μm by volume or mass. They range in size typically from ~5 to >200 μm, with a mass mean of about 75 μm (Kole et al., 2017; Panko et al., 2018; Dalmau et al., 2020). The PM_{10} volume fraction of tire wear is estimated as <1 %, and its contribution to ambient PM_{10} ranges from 0.1 to 10 %. The $PM_{2.5}$ fraction is even smaller; an air sampling study of London, Los Angeles, and Tokyo found a tire and road wear $PM_{2.5}/PM_{10}$ ratio below 20 % and a contribution to total ambient $PM_{2.5}$ of 0.1 to 0.68 % (Panko et al., 2019). Kole et al. (2017) reported a higher, 3–7 % contribution, to airborne $PM_{2.5}$.

Tire and road wear emissions factors are very difficult to determine. One approach is to examine tire wear rates. However, these vary considerably depending on the above-mentioned factors, ranging from 0.04 to 0.4 g/km on a per vehicle basis as complied by Ntziachristos and Boulter (2013), and 0.05 to 0.132 in the review by Kole et al. (2017). Moreover, the majority of wear mass is in particles larger than 10 μm, and wear tests generally do not produce the encrusted tire particles observed in the environment. Measurement of tire emissions via roadside or on-board sampling are other possibilities, but these are confounded by resuspended road dust. A roadside chemical mass balance source apportionment study in Durham NC and Reno NV found no tire wear but recorded resuspended road dust PM10 rates of 40 to 780 mg/mi for light duty spark ignition vehicles (Abu-Allaban et al., 2003). The authors suspected that electrical charge on the rubber tire particles may have biased the collection efficiency of these particles.

There are few immediately apparent avenues to reduce tire wear PM emissions. One obvious way is to lower tire wear rates by material choice and tire construction. The major constraint is vehicle safety, namely the tires must maintain good traction under a large variety of road surface and weather conditions. Improving wear resistance may adversely affect slip and, thereby, safety. It may also raise rolling resistance, which would reduce fuel economy. Even if a more wear resistant tire could be designed without these tradeoffs, it will not necessarily lower road wear PM or resuspended road dust.

Lowering vehicle weight can reduce tire related PM. On-board sampling of tire wear was used by Oroumiyeh and Zhu (2021) to examine tire particles from three vehicles of different weight during real-world driving. The results in Fig. 62 show increases in tire emissions with vehicle weight for braking events that occurred in “low” and “high” deceleration ranges. The results are not corrected for size dependent sampling losses in their probe and sample lines, and they do not distinguish between fresh and resuspended tire particles, but the trend is reasonable. In fact, lowering vehicle weight should also decrease road wear particles and possibly also resuspended road dust, as opposed to just tire wear.

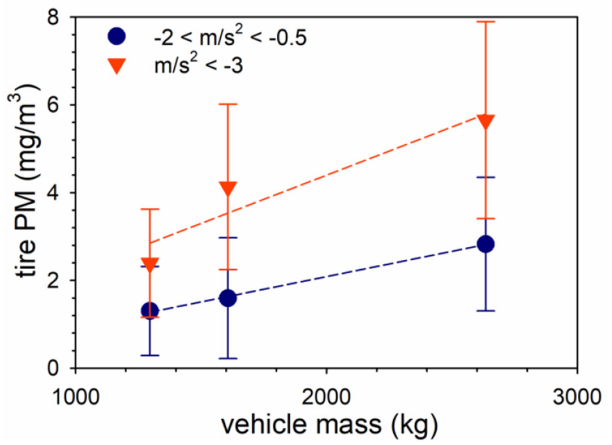

Fig. 62. Tire wear PM emissions from three vehicles of different mass during real world driving (Oroumiyeh and Zhu, 2021). Bars show wear variation over stops in indicated deceleration ranges.

7.3. Summary - non-exhaust PM

Owing to regulatory pressure and technological advances, engine exhaust PM emissions have dwindled from being the major vehicular source to <10 % of total motor vehicle PM emissions under the EU solid particle number standard and the upcoming LEV III 1 mg/mi standard. With the improvements in catalytic aftertreament demanded by progressively more stringent NMHC and NO_x emissions standards, even including tailpipe derived secondary aerosol does not alter the fact that motor vehicle PM emissions are now predominantly non-exhaust in origin. Measuring and quantifying non-exhaust PM is considerably more difficult than engine exhaust particles. Non-exhaust PM does not conveniently exit through a pipe, rather it is generated in the complex airflow environment between the vehicle chassis and road surface. Tire wear measurements are further complicated by its dependence on road surface and weather conditions, and because it occurs simultaneously with road wear and resuspension of road dust.

Non-exhaust PM differs considerably from engine exhaust particles. Under normal driving conditions, brake wear debris falls into the 0.5–10 μm range, whereas tire and road debris can extend to >100 μm. Under harsh driving conditions, for example multiple fast decelerations or mountain decents, brake and tire temperatures can increase to the point where organic components from brake liners and tires volatilize and pyrolyze to form 10–500 nm particles. Because engine exhaust solid particles are unimodal, tailpipe solid number and mass standards both regulate the same thing, namely soot and condensed organics. With respect to non-exhaust PM, however, number and mass regulations apply to two separate subsets of emissions that occur under different conditions.

Besides air pollution, brake and tire wear debris contribute to water pollution. Copper and other metals are washed from the road surface into streams and estuaries (Hulskotte et al., 2007), and tire wear is a source of microplastic contamination in the environment (Kole et al., 2017; Sommer et al., 2018). These, combined with customer satisfaction concerns about wheel dust, provide reasons beyond air quality to lower brake and tire wear rates. In the case of brakes, there are options to reformulate brake pads and adopt advanced rotor designs that reduce wear debris. Regenerative braking adds the dual benefit of friction brake wear debris reduction and energy recovery. Analogous engineering changes to tires are less obvious, and only solve part of the problem, that is they would not reduce road wear and resuspension. Reducing vehicle weight can have multiple benefits; it should lower tire and road wear, as well as reduce brake wear and increase fuel economy. Other means to reduce brake and tire emissions outside of vehicle engineering include traffic management to reduce the amounts of stop and go traffic, which exacerbates brake and tire wear, and street sweeping to reduce dust.

8. Future prospects

Having examined in detail the origins of PM emissions from gasoline vehicles and the advances in engine, aftertreatment, fuel and non-tailpipe technologies that have enabled spark ignition vehicles to keep abreast of declining PM emissions standards, this concluding section takes broader perspective of how they fit into the future transportation fleet. It addresses two topical questions: "Do electrified vehicles offer lower PM emissions than gasoline vehicles?" and "What are the prospects of gasoline vehicles in a 'zero emissions' future?" These questions pertain to several very important motor vehicle environmental and health impacts. To do them justice, a complete discussion needs to include the topics of gaseous pollutants, greenhouse gas emissions, and life cycle analysis. Since these fall outside the scope of the present review, this section has the more modest goal to examine these questions from the narrower perspective of PM emissions with the hope that it will help inform the broader discussion.

8.1. PM emissions from electrified vehicles

Buoyed by rapid progress in Li^+ ion battery technology, a demonstration by Tesla that it is possible to design desirable, high performance, battery electric vehicles (BEV), and realization of potential design and manufacturing simplicities, the auto industry is on the cusp of a potentially major transformation from internal combustion engine (ICE) to electric powertrains. The impetus for this transformation is manifold. It includes elements of climate change, clean air, and scandal induced backlash against ICEs. These have combined to produce a confusing association between BEVs and 'zero emitting vehicles' (ZEV).

The ZEV concept has been around for over thirty years. ZEV requirements were introduced by CARB in 1990 as part of the Low Emission Vehicle regulation because of California's severe air quality problems and the sense that improvements in gasoline vehicle HC and NO_x emissions would prove insufficient for the air quality improvements needed over the long run (Collantes and Sperling, 2008). The view at the time focused narrowly on gaseous pollutants and identified the vehicle as the sole source of these emissions. This led to the designation of ZEV for vehicles, such as BEVs, that do not rely on internal combustion engines for propulsion.

With respect to PM, however, BEVs are not zero emitting vehicles; in fact, they are far from it on the scale of PM emitted from tailpipes of current ICE vehicles. Fig. 63 displays PM_{10} and $PM_{2.5}$ emissions from gasoline, hybrid electric (HEV) and battery electric vehicles that include engine, brake, tire, and road wear emissions. Non-exhaust emissions depend on vehicle weight; thus, the comparison is made for small, medium and large vehicles, with nominal masses of 1200, 1600, and 2000 kg. Adding motors, battery, and other hardware needed for an HEV increases weight by about 7 %, based on a survey of five pairs of comparable 2022 model ICE and HEV vehicles, for which the weight increase ranged from 5 to 9 %. An analogous comparison between pairs of ICE and BEV vehicles by Timmers and Achten (2016) found an average 24 % weight increase. However, a subsequent review paper by them (Timmers and Achten, 2018) lists a 21–24 % range in weight increase. Since future improvements may reduce battery weight, Fig. 63 rounds the BEV weight increase down to 20 %.

Brake, tire, and road wear emissions rates for small, medium, and large vehicles are taken from Simons (2016), and a linear interpolation is used to assign emissions rates for HEVs and BEVs. Finally, the impact of regenerative braking is estimated from the kinetic energy recovery data reported by Jung (2020), which found ~8 % and ~ 54 % recoveries, respectively, for the limiting cases of rapid 60–0 mph braking and 60–10 mph coast downs. Fig. 63 assumes a 50 % recovery near the upper end of this range, which is above the minimums estimated by Beddows and Harrison (2021) for BEVs to maintain brake emissions parity with ICE vehicles in urban and rural driving.

There are two main takeaways from Fig. 63: 1) PM emissions from ICEs, HEVs, and BEVs are essentially the same and 2) at the U.S. 3 mg/mi standard, tailpipe emissions represent a small fraction of vehicle PM emissions in both the PM_{10} and $PM_{2.5}$ size fractions. Several caveats apply to Fig. 63 but do not alter the two principal conclusions. Considerable uncertainties and variabilities exist with respect to brake, tire, and road wear PM rates and their dependencies on vehicle weight. This prevents a PM emissions ranking between the three powertrains, but the conclusion that non-exhaust vehicle PM is considerably larger than tailpipe emissions persists. Resuspended road dust is not included, but this applies to all powertrains and would only heighten the disparity between exhaust and non-exhaust PM.

The comparison does not include displaced tailpipe PM associated with battery charging of BEVs, which increases BEV associated PM emissions in areas that rely on coal fired electricity (Requia et al., 2018; Yang et al., 2021). Secondary aerosol formation is also not included. As shown by Fig. 48, the SOA contribution from gasoline exhaust has dwindled with progressively tighter NMOG standards. On the other hand, BEVs can be responsible for displaced sulfate and nitrate PM emissions depending on electricity source.

These considerations do not alter the fact that non-exhaust sources dominate current vehicle PM emissions, and in this respect BEVs are no different from ICE vehicles. Although not yet commercially available, this conclusion applies to fuel cell vehicles as well. The environmental and health impact

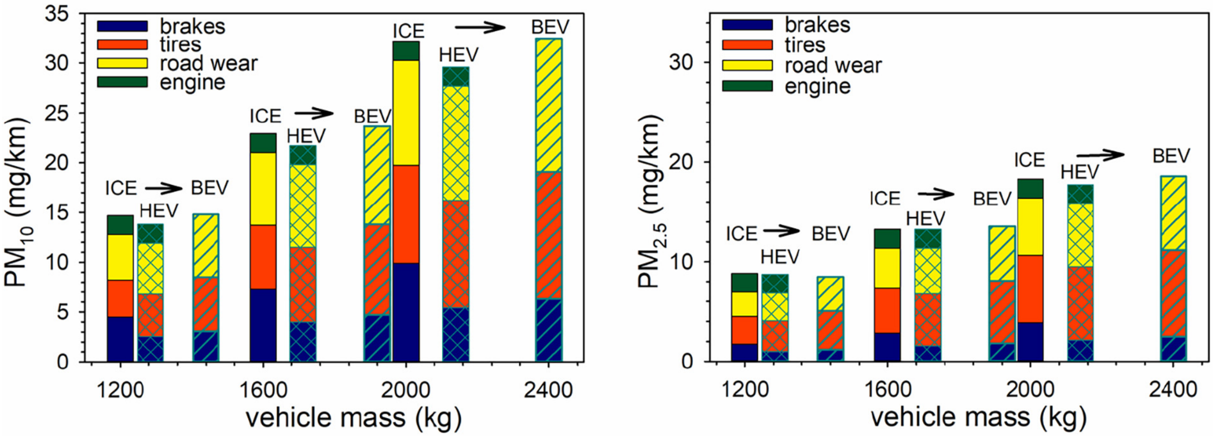

Fig. 63. Total PM emissions from internal combustion engine (ICE) vehicles versus similar model hybrid and battery electric vehicles (BEV). Left panel: PM_{10}. Right panel: $PM_{2.5}$. Brake, tire, and road emissions versus weight from Simons (2016). Hybrid weight increase estimated as 7 %. BEV weight increase is 20 % (Timmers and Achten, 2018). Estimated regenerative brake wear reduction is 50 % (Jung, 2020). Engine PM is set to 3 mg/mi

debate over the preferred powertrain for the future will have to rest on global warming and air quality; PM emissions, if considered for the total vehicle and not just engine exhaust, do not differentiate between ICE and electrified vehicles.

8.2. Gasoline vehicle prospects in a 'zero emissions' future

As mentioned above, the impetus for 'zero emissions' vehicles arose from California's air quality issues regarding smog and ozone formation (Collantes and Sperling, 2008). The exhaust constituents that adversely impact air quality are CO, HCs, NO_x, and soot, which are minor byproducts formed by non-ideal combustion processes. With growing concerns over climate change, 'zero emissions' has evolved over the past two decades to include greenhouse gases, namely CO_2, N_2O, and CH_4. The main culprit in this case is CO_2, which in contrast to pollutant emissions is a primary product of combustion. All of these species are currently subject to government tailpipe emissions regulations.

The history of gasoline engine PM emissions differs from that of the other exhaust constituents. Reigning in CO, HC, and NO_x emissions to meet regulatory standards was accomplished by development of the three-way catalyst (TWC) and replacement of the carburetor with fuel injectors. To function properly, that is to simultaneously oxidize CO and HCs and reduce NO_x, the TWC requires stoichiometric combustion, with an air fuel ratio maintained very close to $\lambda = 1$. In principle, this condition and the premixed fuel air mixture in spark ignition engines leads to soot free combustion. In practice, non-idealities, such as incomplete fuel evaporation and fugitive fuel in crevice volumes, provide mechanisms for soot formation. These mechanisms, however, are also responsible for HC emissions.

As HC emissions standards increased in stringency, the first response by auto manufacturers typically was to improve TWC efficiency, which generally meant an increase in precious metal loadings. Subsequent improvements to lower engine-out HC levels, such as reductions in crevice volumes and improved air - fuel ratio control, provided opportunities to reduce precious metal loadings and, thereby, lower catalyst costs. These improvements synergistically lowered soot emissions. As a result, PFI gasoline vehicles have easily met progressively tighter PM standards as they have been ratcheted down to limit diesel emissions. In fact, PFI gasoline vehicles generally meet the EU solid particle number limit of $6{\cdot}10^{11}$ particles/km, although they are presently not subject to this standard.

This situation changed with the introduction of gasoline direct injection technology. GDI engines were viewed as an efficient, customer acceptable, means to meet regulatory obligations to improve fuel economy and reduce CO_2 emissions. Although they met the U.S. EPA and CARB 10 mg/mi PM standard at the time of their introduction, GDI vehicle emissions were sufficiently higher than those from PFI vehicles to raise concerns among regulators that widespread market penetration would worsen PM air quality (California Air Resources Board, 2010). Subsequently, Tier 3 and LEV III regulations lowered the tailpipe $PM_{2.5}$ standard from 10 to 3 mg/mi. Europe responded likewise and extended the solid particle number standard to include GDI vehicles. Thus, for the first time, gasoline vehicles faced pressure for PM emissions reductions.

Industry reaction to these regulatory changes was swift and successful. GDI engine strategy shifted from stratified combustion to homogeneous combustion, turbocharging, and weight reduction as the means to provide a fuel economy benefit relative to PFI engines, while at the same time limiting PM emissions. Fuel impingement onto the piston and injector tip wetting were identified as principal soot sources. Injection timing was optimized to be sufficiently early for good fuel air mixing but not so early as to risk impingement on the piston. Injection pressure was increased to lower fuel droplet size and promote evaporation. Fuel injectors were redesigned for better targeting, lower fuel dribble, less needle bounce, and lower tip temperature to reduce tip wetting. Multiple injection strategies were adopted to reduce spray penetration and to lower catalyst warm-up times. Combined PFI / DI injection systems were introduced to optimize emissions and fuel economy. As a result, GDI vehicles now meet the U.S. EPA and CARB LEV III 3 mg/mi PM mass standard.

There is evidence that engine and fuel injection technology advances can approach and perhaps meet the upcoming LEV III 1 mg/mi standard as well as the EU solid particle number standard. However, it remains unclear how broadly across GDI vehicle platforms this extends and how confidently it applies to real world driving conditions. Further improvements remain to reduce cold start PM emissions, particularly in cold weather conditions, as well as to limit emissions in aggressive driving situations.

At the same time, GPF technology has evolved to the point that GDI vehicles so equipped are able to pass the EU solid particle number standard under RDE testing and beyond. Further GPF development, for example with artificial ash membranes, can ensure high initial filtration efficiency with minimal backpressure penalty. Since the GPF does not need to warm up for efficient filtration, it is effective in the cold start, even at low ambient temperatures. Laboratory and real-world driving tests show virtually no decrease in fuel economy when replacing an underbody catalyst with a GPF. A measurable backpressure penalty occurs near rated engine power, but this can be reduced with improved entrance and exit cone designs relative to those currently used with TWCs and adapted to GPFs.

In summary, engine and GPF technology advances provide the capability for GDI vehicles, and PFI vehicles, if necessary, to meet the very stringent 2025 LEV III 1 mg/mi mass and EU $6{\cdot}10^{11}$ particles/km engine exhaust particle emissions standards. Relative to the more than order of magnitude larger non-exhaust PM emissions, gasoline vehicle tailpipe PM levels at these standards effectively represent 'zero emissions'.

The future prospects for gasoline vehicles then rest on their ability to achieve 'zero emissions' with respect to gaseous pollutants and greenhouse gases. Roadside measurements in the Chicago area show real-world emissions reductions in fuel specific HC emissions by a factor of ~20 over the past three decades and NO emissions by a factor of ~5 over the past two decades (Bishop and Haugen, 2018). The study also finds that emissions durability has increased to the point where Tier 2 vehicles have nearly eliminated the emissions reductions benefits from fleet turnover. Such declines in vehicle emissions are corroborated by recent investigations of emissions inventories, which reveal that volatile consumer products now constitute half of the fossil fuel volatile organic compound emissions in industrialized cities (McDonald et al., 2018). These trends have led to questions about how low must tailpipe emissions become to have an environmental impact that is indistinguishable from non-ICE powertrains (Winkler et al., 2018). Kawaguchi et al. (2019) provide an example of extremely low emissions from a plug-in hybrid vehicle that achieves emissions levels 1/10 of SULEV30. At such low levels, it no longer makes sense to debate the ICE versus BEV tailpipe emissions difference in the face of larger life cycle emissions related to vehicle manufacture, energy generation, and recycling.

Climate change concerns may, thus, become the major determining factor in gasoline vehicles' future role in transportation. Here it is useful to think of liquid hydrocarbons as an energy storage medium rather than a fuel. In this view, one has the option to use a renewable energy source to charge a battery or to produce liquid hydrocarbons. The latter can be achieved via biofuels (U.S. Department of Energy, 2022), with the sun as energy source, or via efuels (Rothbart, 2020) produced from CO_2 using solar, wind, or hydro power. Thus, it is possible to power ICEs with the same ultimate energy source as it is to power BEVs. The goal, therefore, does not have to be a single winner as the powertrain choice of the future. As noted by Senecal and Leach (2019), there are powerful reasons, including energy independence, resilience to disruptive events, differences in regional needs and the very wide range of vehicle use cases, to embrace diversity in vehicle powertrain options rather than aim for a singular solution. Within the right regulatory framework, the combination of ICE, HEV, BEV, and fuel cell powertrains may lead to a better environmental future than any one by itself.

Author contributions

Maricq, M. Matti: Conceptualization, Formal analysis, Funding acquisition, Investigation, Visualization, Writing- Original draft preparation, Writing- Reviewing and Editing

Data availability

No data was used for the research described in the article.

Declaration of Competing Interest

The authors declare the following financial interests/personal relationships which may be considered as potential competing interests:

M. Matti Maricq reports financial support was provided by Coordinating Research Council Inc. M. Matti Maricq reports a relationship with Coordinating Research Council Inc. that includes: funding grants.

Acknowledgments

This work was funded by the Coordinating Research Council, Alpharetta, GA, USA under Project E-136. I am grateful to Amber Leland and Rebecca Kang (CRC) and project panel leads Nathan Kempema (Ford) and Russ Lewis (Marathon Petroleum) for their help and support during this project. I thank Jim Anderson (Ford), Tak Chan (Environment Canada), Tom Durbin (CE-CERT), Barouch Giechaskiel (JRC), Kent Johnson (CE-CERT), Heejung Jung (UC Riverside), Georgios Karavalakis (CE-CERT), Imad Khalek (SwRI), Leon Ntziachristos (Aristotle University), John Storey (ORNL), and Rainer Vogt (Ford) for sending me their collected works on gasoline vehicle PM emissions, as well as many other authors who were kind enough to forward me reprints of their publications.

References

Abdul-Khalek, I.S., Kittelson, D.B., 1995. Real time measurement of volatile and solid exhaust particles using a catalytic stripper. SAE Trans., 462–478.. https://www.jstor.org/stable/44633232.

Abu-Allaban, M., Gillies, J.A., Gertler, A.W., Clayton, R., Proffitt, D., 2003. Tailpipe, resuspended road dust, and brake-wear emission factors from on-road vehicles. Atmos. Environ. 37 (37), 5283–5293. https://doi.org/10.1016/j.atmosenv.2003.05.005.

Aikawa, K., Jetter, J.J., 2014. Impact of gasoline composition on particulate matter emissions from a direct-injection gasoline engine: applicability of the particulate matter index. Int. J. Engine Res. 15 (3), 298–306. https://doi.org/10.1177/1468087413481216.

Aikawa, K., Sakurai, T., Jetter, J.J., 2010. Development of a predictive model for gasoline vehicle particulate matter emissions. SAE Int. J. Fuels Lubr. 3 (2), 610–622.. https://www.jstor.org/stable/26272963.

Aleksandrova, S., Saul, J., Prantoni, M., Medina, H., Garcia-Afonso, O., Bevan, M., Benjamin, S., 2019. Turbulent flow pressure losses in gasoline particulate filters. SAE Int. J. Engines 12 (4), 455–470.. https://www.jstor.org/stable/26897923.

Alemani, M., Nosko, O., Metinoz, I., Olofsson, U., 2016. A study on emission of airborne wear particles from car brake friction pairs. SAE Int. J. Mater. Manuf. 9 (1), 147–157. https://www.jstor.org/stable/26268814.

Alkidas, A.C., 2007. Combustion advancements in gasoline engines. Energy Convers. Manag. 48 (11), 2751–2761. https://doi.org/10.1016/j.enconman.2007.07.027.

Alkidas, A., El Tahry, S., 2003. Contributors to the Fuel Economy Advantage of DISI Engines Over PFI Engines, SAE Technical Paper 2003-01-3101. https://doi.org/10.4271/2003-01-3101.

Allocca, L., Lazzaro, M., Meccariello, G., Montanaro, A., 2016. Schlieren visualization of a GDI spray impacting on a heated wall: non-vaporizing and vaporizing evolutions. Energy 108, 93–98. https://doi.org/10.1016/j.energy.2015.09.107.

Aranke, O., Algenaid, W., Awe, S., Joshi, S., 2019. Coatings for automotive gray cast iron brake discs: a review. Coatings 9 (9), 552. https://doi.org/10.3390/coatings9090552.

Arnott, W.P., Zielinska, B., Rogers, C.F., Sagebiel, J., Park, K., Chow, J., Palmer, G., 2005. Evaluation of 1047-nm photoacoustic instruments and photoelectric aerosol sensors in source-sampling of black carbon aerosol and particle-bound PAHs from gasoline and diesel powered vehicles. Environ. Sci. Technol. 39 (14), 5398–5406. https://doi.org/10.1021/es049595e.

Ashida, T., Takei, Y., Hosi, H., 2001. Effects of fuel properties on SIDI fuel injector deposit. SAE Technical Paper 2001-01-3694 https://doi.org/10.4271/2001-01-3694.

Ashley, C., 1996. The Mitsubishi... Gasoline direct injection engine (GDI). Automot. Eng. 21 (5).. http://worldcat.org/issn/03076490.

Awad, O.I., Ma, X., Kamil, M., Ali, O.M., Zhang, Z., Shuai, S., 2020. Particulate emissions from gasoline direct injection engines: a review of how current emission regulations are being met by automobile manufacturers. Sci. Total Environ. 718, 137302. https://doi.org/10.1016/j.scitotenv.2020.137302.

Backes, F., Blochum, S., Härtl, M., Wachtmeister, G., 2020. Experimental analysis of gasoline direct injector tip wetting. SAE Int. J. Engines 13 (1), 77–92.. https://www.jstor.org/stable/26926863.

Badami, M., Mallamo, F., Millo, F., Rossi, E.E., 2002. Influence of multiple injection strategies on emissions, combustion noise and BSFC of a DI common rail diesel engine. SAE Trans., 1118–1129.. https://www.jstor.org/stable/44743137.

Bahreini, R., Middlebrook, A.M., De Gouw, J.A., Warneke, C., Trainer, M., Brock, C.A., Parrish, D.D., 2012. Gasoline emissions dominate over diesel in formation of secondary organic aerosol mass. Geophys. Res. Lett. 39 (6). https://doi.org/10.1029/2011GL050718.

Bandel, W., Fraidl, G., Kapus, P., Sikinger, H., et al., 2006. The Turbocharged GDI Engine: Boosted Synergies for High Fuel Economy Plus Ultra-low Emission, SAE Technical Paper 2006-01-1266. https://doi.org/10.4271/2006-01-1266.

Barker, J., Reid, J., Mulqueen, S., Langley, G.J., Wilmot, E.M.J., Vadodaria, S., Castle, J., Whitaker, J., 2019. The Investigation of the Structure and Origins of Gasoline Direct Injection (GDI) Deposits. SAE Technical Paper 2019-01-2356. https://doi.org/10.4271/2019-01-2356.

Barone, T.L., Storey, J.M., Youngquist, A.D., Szybist, J.P., 2012. An analysis of direct-injection spark-ignition (DISI) soot morphology. Atmos. Environ. 49, 268–274. https://doi.org/10.1016/j.atmosenv.2011.11.047.

Barrientos, E.J., Anderson, J.E., Maricq, M.M., Boehman, A.L., 2016. Particulate matter indices using fuel smoke point for vehicle emissions with gasoline, ethanol blends, and butanol blends. Combust. Flame 167, 308–319. https://doi.org/10.1016/j.combustflame.2016.01.034.

Beddows, D.C., Harrison, R.M., 2021. PM10 and PM2. 5 emission factors for non-exhaust particles from road vehicles: dependence upon vehicle mass and implications for battery electric vehicles. Atmos. Environ. 244, 117886. https://doi.org/10.1016/j.atmosenv.2020.117886.

Behringer, M., Aleiferis, P., OudeNijeweme, D., Freeland, P., 2014. Spray formation from spark-eroded and laser-drilled injectors for DISI engines with gasoline and alcohol fuels. SAE Int. J. Fuels Lubr. 7 (3), 803–822.. https://www.jstor.org/stable/26273720.

Bishop, G.A., Haugen, M.J., 2018. The story of ever diminishing vehicle tailpipe emissions as observed in the Chicago, Illinois area. Environ. Sci. Technol. 52 (13), 7587–7593. https://doi.org/10.1021/acs.est.8b00926.

Bishop, I.N., Simko, A., 1968. A new concept of stratified charge combustion—the ford combustion process (FCP). SAE Trans., 93–131.. https://www.jstor.org/stable/44565049.

Bogarra, M., Herreros, J.M., Hergueta, C., Tsolakis, A., York, A.P., Millington, P.J., 2017. Influence of three-way catalyst on gaseous and particulate matter emissions during gasoline direct injection engine cold-start. Johnson Matthey Technol. Rev. 61 (4), 329–341.

Boger, T., Rose, D., Nicolin, P., Gunasekaran, N., Glasson, T., 2015. Oxidation of soot (Printex® U) in particulate filters operated on gasoline engines. Emiss. Control Sci. Technol. 1 (1), 49–63. https://doi.org/10.1007/s40825-015-0011-1.

Bolte, G., Pauli, A., Hornberg, C., 2011. Environmental justice: Social disparities in environmental exposures and health: overview. Encyclopedia of Environ. Health , pp. 459–470.. https://pub.uni-bielefeld.de/record/2910158.

Bornschlegel, S., Conrad, C., Durst, A., Wang, J., Wensing, M., 2018. Multi-hole gasoline direct injection: in-nozzle flow and primary breakup investigated in transparent nozzlesand with X-ray. Int. J. Engine Res. 19 (1), 67–77. https://doi.org/10.1177/1468087417746860.

Butler, A.D., Sobotowski, R.A., Hoffman, G.J., Machiele, P., 2015. Influence of fuel PM Index and ethanol content on particulate emissions from light-duty gasoline vehicles. SAE Technical Paper 2015-01-1072 https://doi.org/10.4271/2015-01-1072.

Cai, R., Zhang, J., Nie, X., Tjong, J., Matthews, D.T.A., 2020. Wear mechanism evolution on brake discs for reduced wear and particulate emissions. Wear 452, 203283. https://doi.org/10.1016/j.wear.2020.203283.

Calcote, H.F., Manos, D.M., 1983. Effect of molecular structure on incipient soot formation. Combust. Flame 49 (1–3), 289–304. https://doi.org/10.1016/0010-2180(83)90172-4.

California Air Resources Board, 2010. Preliminary Discussion Paper: Proposed Amendments to California's Low Emission Vehicle Regulations—Particulate Matter Mass, Ultrafine Solid Particle Number, and Black Carbon Emissions. https://ww2.arb.ca.gov/sites/default/files/2020-02/pm_disc_paper_v6_ac.pdf.

Carlisle, H.W., Frew, R.W., Mills, J.R., Aradi, A.A., Avery, N.L., 2001. The effect of fuel composition and additive content on injector deposits and performance of an air-assisted direct injection spark ignition (DISI) research engine. SAE Trans., 1549–1565.. https://www.jstor.org/stable/44742755.

Chan, T.W., Meloche, E., Kubsh, J., Brezny, R., 2014. Black carbon emissions in gasoline exhaust and a reduction alternative with a gasoline particulate filter. Environ. Sci. Technol. 48 (10), 6027–6034. https://doi.org/10.1021/es501791b.

Chan, T.W., Saffaripour, M., Liu, F., Hendren, J., Thomson, K.A., Kubsh, J., Rideout, G., 2016. Characterization of real-time particle emissions from a gasoline direct injection vehicle equipped with a catalyzed gasoline particulate filter during filter regeneration. Emiss. Control Sci. Technol. 2 (2), 75–88. https://doi.org/10.1007/s40825-016-0033-3.

Chan, T.W., Lax, D., Gunter, G.C., Hendren, J., Kubsh, J., Brezny, R., 2017. Assessment of the fuel composition impact on black carbon mass, particle number size distributions, solid particle number, organic materials, and regulated gaseous emissions from a light-duty gasoline direct injection truck and passenger car. Energy Fuel 31 (10), 10452–10466. https://doi.org/10.1021/acs.energyfuels.7b01345.

Chang, M.C.O., Shields, J.E., 2017. Evaluation of solid particle number and black carbon for very low particulate matter emissions standards in light-duty vehicles. J. Air Waste Manage. Assoc. 67 (6), 677–693. https://doi.org/10.1080/10962247.2016.1268548.

Chang, M., Lee, Z., Park, S., Park, S., 2020. Characteristics of flash boiling and its effects on spray behavior in gasoline direct injection injectors: a review. Fuel 271, 117600. https://doi.org/10.1016/j.fuel.2020.117600.

Chapman, E., Winston-Galant, M., Geng, P., Latigo, R., Boehman, A., 2016. Alternative fuel property correlations to the Honda Particulate Matter Index (PMI). SAE Technical Paper 2016-01-2250 https://doi.org/10.4271/2016-01-2250.

Chen, L., Liang, Z., Zhang, X., Shuai, S., 2017. Characterizing particulate matter emissions from GDI and PFI vehicles under transient and cold start conditions. Fuel 189, 131–140. https://doi.org/10.1016/j.fuel.2016.10.055.

Chen, Y., Zhang, Y., Cheng, W., 2018. Effects of ethanol evaporative cooling on particulate number emissions in gdi engines. SAE Technical Paper 2018-01-0360 https://doi.org/10.4271/2018-01-0360.

Cheng, W.K., Hamrin, D., Heywood, J.B., Hochgreb, S., Min, K., Norris, M., 1993. An Overview of Hydrocarbon Emissions Mechanisms in Spark-Ignition Engines, SAE Technical Paper 932708. https://doi.org/10.4271/932708.

Choi, S., Myung, C.L., Park, S., 2014. Review on characterization of nano-particle emissions and PM morphology from internal combustion engines: part 2. Int. J. Automot. Technol. 15, 219–227. https://doi.org/10.1007/s12239-014-0023-9.

Clark, N., Klein, T., Higgins, T., McKain, D.L., 2019. Emissions From Low-and Mid-level Blends of Anhydrous Ethanol in Gasoline. SAE Technical Paper 2019-01-0997. https://doi.org/10.4271/2019-01-0997.

Clark, N.N., McKain Jr., D.L., Klein, T., Higgins, T.S., 2021. Quantification of gasoline-ethanol blend emissions effects. J. Air Waste Manage. Assoc. 71 (1), 3–22. https://doi.org/10.1080/10962247.2020.1754964.

Code of Federal Regulations, 2022a. Title 40 Part 50, National Primary and Secondary Ambient Air Quality Standards. https://www.ecfr.gov/current/title-40/chapter-I/subchapter-C/part-50?toc=1.

Code of Federal Regulations, 2022b. Title 40 Part 86, Control of emissions from new and in-use highway vehicles and engines. Subpart S § 86.1811–04 https://www.ecfr.gov/current/title-40/chapter-I/subchapter-C/part-86/subpart-A?toc=1.

Code of Federal Regulations, 2022c. Title 40 Part 1065, Engine testing procedures. https://www.ecfr.gov/current/title-40/chapter-I/subchapter-U/part-1065.

Code of Federal Regulations, 2022d. Title 40 Part 1066, Vehicle testing procedures. https://www.ecfr.gov/current/title-40/chapter-I/subchapter-U/part-1066.

Collantes, G., Sperling, D., 2008. The origin of California's zero emission vehicle mandate. Transp. Res. A Policy Pract. 42 (10), 1302–1313. https://doi.org/10.1016/j.tra.2008.05.007.

Commodo, M., Kaiser, K., De Falco, G., Minutolo, P., Schulz, F., D'Anna, A., Gross, L., 2019. On the early stages of soot formation: molecular structure elucidation by high-resolution atomic force microscopy. Combust. Flame 205, 154–164. https://doi.org/10.1016/j.combustflame.2019.03.042.

Crawford, R., Lyons, J., 2019. Assessment of the relative accuracy of the pm index and related methods, Coordinating Research Council Project RW-107. http://crcsite.wpengine.com/wp-content/uploads/2019/05/CRC-RW-107-Final-Report_2019-04-15.pdf.

Crawford, R., Snoeberger, J., Lyons, J., 2021. An improved index for particulate matter emissions (PME), Coordinating Research Council Project RW-107-2. https://3mpm51mqb7ryj2j12n04r01b-wpengine.netdna-ssl.com/wp-content/uploads/2021/03/CRC_RW107-2_2021.03.26.pdf.

Dahlander, P., Hemdal, S., 2015. High-speed photography of stratified combustion in an optical GDI engine for different triple injection strategies. SAE Technical Paper 2015-01-0745 https://doi.org/10.4271/2015-01-0745.

Dall'Osto, M., Beddows, D.C., Gietl, J.K., Olatunbosun, O.A., Yang, X., Harrison, R.M., 2014. Characteristics of Tyre dust in polluted air: studies by single particle mass spectrometry (ATOFMS). Atmos. Environ. 94, 224–230. https://doi.org/10.1016/j.atmosenv.2014.05.026.

Dalmau, M.E., Augsburg, K., Wenzel, F., Ivanov, V., 2020. Tire particle emissions: demand on reliable characterization. Tire Sci.Technol. 48 (2), 107–122. https://doi.org/10.2346/tire.19.170181.

Davis, R.S., Mandrusiak, G.D., Landenfeld, T., 2009. Development of the combustion system for general motors' 3.6 L DOHC 4V V6 engine with direct injection. SAE Int. J. Engines 1 (1), 85–100.. https://www.jstor.org/stable/26308263.

De Filippo, A., Maricq, M.M., 2008. Diesel nucleation mode particles: semivolatile or solid? Environ. Sci. Technol. 42 (21), 7957–7962. https://doi.org/10.1021/es8010332.

Dearn, K., Xu, J., Ding, H., Xu, H., Weall, A., Kirkby, P., Krueger-Venus, J., 2014. An investigation into the characteristics of DISI injector deposits using advanced analytical methods. SAE Int. J. Fuels Lubr. 7 (3), 771–782.. https://www.jstor.org/stable/26273717.

Dec, J.E., 1997. A conceptual model of DL diesel combustion based on laser-sheet imaging. SAE Trans., 1319–1348.. https://www.jstor.org/stable/44730758.

Dec, J.E., 2009. Advanced compression-ignition engines—understanding the in-cylinder processes. Proc. Combust. Inst. 32 (2), 2727–2742. https://doi.org/10.1016/j.proci.2008.08.008.

Dec, J.E., Kelly-Zion, P.L., 2000. The effects of injection timing and diluent addition on late-combustion soot burnout in a DI diesel engine based on simultaneous 2-D imaging of OH and soot. SAE Technical Paper 2000-01-0238 https://doi.org/10.4271/2000-01-0238.

Demuynck, J., Favre, C., Bosteels, D., Hamje, H., Andersson, J., 2017. Real-world emissions measurements of a gasoline direct injection vehicle without and with a gasoline particulate filter. SAE Technical Paper 2017-01-0985 https://doi.org/10.4271/2017-01-0985.

DieselNet, 2021. Engine and Emission Technology Online. https://dieselnet.com.

Dobbins, R.A., 2002. Soot inception temperature and the carbonization rate of precursor particles. Combust. Flame 130 (3), 204–214. https://doi.org/10.1016/S0010-2180(02)00374-7.

Dober, G., Karimi, K., Lemaitre, B., Majerus, C., Guerrassi, N., 2020. Advanced measurement techniques for the characterization of GDI injector tip wetting and a phenomenological model of the wetting process. THIESEL 2020 Conference on Thermo- and Fluid Dynamic Processes in Direct Injection Engines.

Dockery, D.W., Pope III, A., Xu, X., et al., 1993. An association between air pollution and mortality in six U. S. cities. New Eng. J. Med. 329, 1753–1759. https://doi.org/10.1056/NEJM199312093292401.

Dominici, F., 2004. Time-series analysis of air pollution and mortality: A statistical review. Health Effects Institute, Research Report 123 PMID: 15757000.

Drake, M.C., Fansler, T.D., Solomon, A.S., Szekely Jr., G.A., 2003. Piston fuel films as a source of smoke and hydrocarbon emissions from a wall-controlled spark-ignited direct-injection engine. SAE Trans., 762–783.. https://www.jstor.org/stable/44741311.

Duke, D.J., Kastengren, A.L., Matusik, K.E., Swantek, A.B., Powell, C.F., Payri, R., Pickett, L.M., 2017. Internal and near nozzle measurements of engine combustion network “Spray G” gasoline direct injectors. Exp. Thermal Fluid Sci. 88, 608–621. https://doi.org/10.1016/j.expthermflusci.2017.07.015.

Edney, M.K., Barker, J., Reid, J., Scurr, D.J., Snape, C.E., 2020a. Recent advances in the analysis of GDI and diesel fuel injector deposits. Fuel 272, 117682. https://doi.org/10.1016/j.fuel.2020.117682.

Edney, M.K., Lamb, J.S., Spanu, M., Smith, E.F., Steer, E., Wilmot, E., Scurr, D.J., 2020b. Spatially resolved molecular compositions of insoluble multilayer deposits responsible for increased pollution from internal combustion engines. ACS Appl. Mater. Interfaces 12 (45), 51026–51035. https://doi.org/10.1021/acsami.0c14532.

Edney, M.K., Smith, E.F., Wilmot, E., Reid, J., Barker, J., Alexander, M.R., Scurr, D.J., 2021. The Effect of Temperature on the Molecular Compositions of External and Internal Gasoline Direct Injection Deposits. SAE Technical Paper, 2021-01-1188. https://doi.org/10.4271/2021-01-1188.

EU Commission, 2022. Document 52022PC0586. Proposal for a REGULATION OF THE EUROPEAN PARLIAMENT AND OF THE COUNCIL on type-approval of motor vehicles and engines and of systems, components and separate technical units intended for such vehicles, with respect to their emissions and battery durability (Euro 7) and repealing Regulations (EC) No 715/2007 and (EC) No 595/2009. https://eur-lex.europa.eu/legal-content/EN/ALL/?uri=COM:2022:586:FIN.

Fan, L., Li, G., Han, Z., Reitz, R.D., 1999. Modeling fuel preparation and stratified combustion in a gasoline direct injection engine. SAE Trans., 105–119.. https://www.jstor.org/stable/44743356.

Fang, T., Wang, L., Wang, Z., 2017. Particulate matter emissions from gasoline direct injection engines: research review. J. Autom. Saf. Energy 8, 226–238. https://doi.org/10.3969/j.issn.1674-8484.2017.03.002.

Fanick, R., Kroll, S., Swarts, A., Quarderer, S., 2019. Effects of Dual Port Injection and Direct-injection Technology on Combustion Emissions from Light-Duty Gasoline Vehicles. SAE Technical Paper 2019-01-0999. https://doi.org/10.4271/2019-01-0999.

Fatouraie, M., Frommherz, M., Mosburger, M., Chapman, E., Li, S., McCormick, R., Fioroni, G., 2018. Investigation of the impact of fuel properties on particulate number emission of a modern gasoline direct injection engine. SAE Technical Paper 2018-01-0358 https://doi.org/10.4271/2018-01-0358 PMID: 15757000.

Fischer, M., Kreutziger, P., Sun, Y., Kotrba, A., 2017. Clean EGR for gasoline engines – innovative approach to efficiency improvement and emissions reduction simultaneously. SAE Technical Paper 2017-01-0683 https://doi.org/10.4271/2017-01-0683.

Forestieri, S.D., Collier, S., Kuwayama, T., Zhang, Q., Kleeman, M.J., Cappa, C.D., 2013. Real-time black carbon emission factor measurements from light duty vehicles. Environ. Sci. Technol. 47 (22), 13104–13112. https://doi.org/10.1021/es401415a.

Fraser, N., Blaxill, H., Lumsden, G., Basett, M., 2009. Challenges for increased efficiency through gasoline engine downsizing, SAE Technical Paper 2009–01-1063. https://www.jstor.org/stable/26308449.

Frenklach, M., 2002. Reaction mechanism of soot formation in flames. Phys. Chem. Chem. Phys. 4 (11), 2028–2037. https://doi.org/10.1039/B110045A.

Frottier, C., Sens, M., Rieß, M., Wigger, M., Benz, A., Maekawa, N., Machida, K., 2014. Achieving very low PN emissions with an advanced multi-hole injector functionality and adapted spray targeting under high fuel pressure conditions. SAE Int. J. Engines 7 (4), 1744–1751.. https://www.jstor.org/stable/26277885.

Fulper, C.R., Kishan, S., Baldauf, R.W., Sabisch, M., Warila, J., Fujita, E.M., Cantrell, B., 2010. Methods of characterizing the distribution of exhaust emissions from light-duty, gasoline-powered motor vehicles in the US fleet. J. Air Waste Manage. Assoc. 60 (11), 1376–1387. https://doi.org/10.3155/1047-3289.60.11.1376.

Fung, K., Chow, J.C., Watson, J.G., 2002. Evaluation of OC/EC speciation by thermal manganese dioxide oxidation and the IMPROVE method. J. Air Waste Manage. Assoc. 52 (11), 1333–1341. https://doi.org/10.1080/10473289.2002.10470867.

Gagné, S., Couillard, M., Gajdosechova, Z., Momenimovahed, A., Smallwood, G., Mester, Z., Corbin, J.C., 2021. Ash-decorated and ash-painted soot from residual and distillate-fuel combustion in four marine engines and one aviation engine. Environ. Sci. Technol. 55 (10), 6584–6593. https://doi.org/10.1021/acs.est.0c07130.

Gentner, D.R., Jathar, S.H., Gordon, T.D., Bahreini, R., Day, D.A., El Haddad, I., Robinson, A.L., 2017. Review of urban secondary organic aerosol formation from gasoline and diesel motor vehicle emissions. Environ. Sci. Technol. 51 (3), 1074–1093. https://doi.org/10.1021/acs.est.6b04509.

Giechaskiel, B., Dilara, P., Andersson, J., 2008. Particle measurement programme (PMP) light-duty inter-laboratory exercise: repeatability and reproducibility of the particle number method. Aerosol Sci. Technol. 42, 528–543. https://doi.org/10.1080/02786820802220241.

Giechaskiel, B., Melas, A., Martini, G., Dilara, P., 2021. Overview of vehicle exhaust particle number regulations. Processes 9 (12), 2216. https://doi.org/10.3390/pr9122216.

Giechaskiel, B., Melas, A., Valverde, V., Otura, M., Martini, G., 2022. Challenging conditions for gasoline particulate filters (GPFs). Catalysts 12 (1), 70. https://doi.org/10.3390/catal12010070.

Gill, R.J., Olson, D.B., 1984. Estimation of soot thresholds for fuel mixtures. Combust. Sci. Technol. 40 (5–6), 307–315. https://doi.org/10.1080/00102208408923814.

Golkarfard, V., Subramaniam, R., Broughton, J., King, A., Mullins, B., 2019. Comparative performance of 12 crankcase oil mist separators. SAE Int. J. Engines 12 (1), 5–14.. https://www.jstor.org/stable/26745560.

Gordon, T.D., Presto, A.A., Nguyen, N.T., Robertson, W.H., Na, K., Sahay, K.N., Robinson, A.L., 2014a. Secondary organic aerosol production from diesel vehicle exhaust: impact of aftertreatment, fuel chemistry and driving cycle. Atmos. Chem. Phys. 14 (9), 4643–4659. https://doi.org/10.5194/acp-14-4643-2014.

Gordon, T.D., Presto, A.A., May, A.A., Nguyen, N.T., Lipsky, E.M., Donahue, N.M., Robinson, A.L., 2014b. Secondary organic aerosol formation exceeds primary particulate matter emissions for light-duty gasoline vehicles. Atmos. Chem. Phys. 14 (9), 4661–4678. https://doi.org/10.5194/acp-14-4661-2014.

Grigoratos, T., Agudelo, C., Grochowicz, J., Gramstat, S., Robere, M., Perricone, G., Mathissen, M., 2020. Statistical assessment and temperature study from the interlaboratory application of the WLTP–brake cycle. Atmosphere 11 (12), 1309. https://doi.org/10.3390/atmos11121309.

Guerrassi, N., Dupraz, P., 1998. A common rail injection system for high speed direct injection diesel engines. SAE Technical Paper 980803 https://doi.org/10.4271/980803.

Guinther, G., Smith, S., 2016. Formation of intake valve deposits in gasoline direct injection engines. SAE Int. J. Fuels Lubricants 9 (3), 558–566.. https://www.jstor.org/stable/26273486.

Harris, S.J., Weiner, A.M., 1985. Chemical kinetics of soot particle growth. Annu. Rev. Phys. Chem. 36 (1), 31–52. https://doi.org/10.1146/annurev.pc.36.100185.000335.

Hascoët, M., Adamczak, L., 2020. At source brake dust collection system. Results Eng. 5, 100083. https://doi.org/10.1016/j.rineng.2019.100083.

He, X., Ireland, J.C., Zigler, B.T., Ratcliff, M.A., Knoll, K.E., Alleman, T.L., Tester, J.T., 2010. Impacts of Mid-level Biofuel Content in Gasoline on SIDI Engine-out and Tailpipe Particulate Matter Emissions. https://doi.org/10.4271/2010-01-2125.

He, X., Ratcliff, M.A., Zigler, B.T., 2012. Effects of gasoline direct injection engine operating parameters on particle number emissions. Energy Fuel 26 (4), 2014–2027. https://doi.org/10.1021/ef201917p.

Hedge, M., Weber, P., Gingrich, J., Alger, T., Khalek, I., 2011. Effect of EGR on particle emissions from a GDI engine. SAE Int. J. Engines 4 (1), 650–666.. https://www.jstor.org/stable/26278177.

HEI Review Panel on Ultrafine Particles, 2013. Understanding the Health Effects of Ambient Ultrafine Particles. HEI Perspectives 3. Health Effects Institute, Boston, MA.

Hélie, J., Lamarque, N., Fremaux, J.L., Serrecchia, P., Khosravi, M., Berkemeier, O., 2021. The process of tip wetting at the spray injection end. Int. J. Engine Res. 22 (1), 125–139. https://doi.org/10.1177/1468087419840842.

Hemdal, S., Andersson, M., Dahlander, P., Ochoterena, R., Denbratt, I., 2011. In-cylinder soot imaging and emissions of stratified combustion in a spark-ignited spray-guided direct-injection gasoline engine. Int. J. Engine Res. 12 (6), 549–563. https://doi.org/10.1177/1468087411418167.

Henkel, S., Hardalupas, Y., Taylor, A., Conifer, C., Cracknell, R., Goh, T.K., Rieß, M., 2017. Injector fouling and its impact on engine emissions and spray characteristics in gasoline direct injection engines. SAE Int. J. Fuels Lubricants 10 (2), 287–295.. https://www.jstor.org/stable/26274112.

Hesse, D., Hamatschek, C., Augsburg, K., Weigelt, T., Prahst, A., Gramstat, S., 2021. Testing of alternative disc brakes and friction materials regarding brake wear particle emissions and temperature behavior. Atmosphere 12 (4), 436. https://doi.org/10.3390/atmos12040436.

Heywood, J.B., 2018. Internal Combustion Engine Fundamentals. McGraw-Hill Education.

Higgins, K.J., Jung, H., Kittelson, D.B., Roberts, J.T., Zachariah, M.R., 2002. Size-selected nanoparticle chemistry: kinetics of soot oxidation. J. Phys. Chem. A 106 (1), 96–103. https://doi.org/10.1021/jp004466f.

Hinds, W.C., 1999. Aerosol Technology: Properties, Behavior, and Measurement of Airborne Particles. John Wiley & Sons.

Hoekman, S.K., Khlystov, A., 2022. Effect of detailed hydrocarbon analysis (DHA) development on particulate matter index (PMI) variability. Coordinating Research Council Project AVFL-29-2. https://3mpm51mqb7ryj2j12n04r01b-wpengine.netdna-ssl.com/wp-content/uploads/2022/01/CRC-Project-AVFL-29-2-Final-Report_January-2022.pdf.

Hoffmann, G., Befrui, B., Berndorfer, A., Piock, W.F., Varble, D.L., 2014. Fuel system pressure increase for enhanced performance of GDi multi-hole injection systems. SAE Int. J. Engines 7 (1), 519–527.. https://www.jstor.org/stable/26277782.

Hooftman, N., Messagie, M., Van Mierlo, J., Coosemans, T., 2018. A review of the european passenger car regulations–Real driving emissions vs local air quality. Renew. Sust. Energ. Rev. 86, 1–21. https://doi.org/10.1016/j.rser.2018.01.012.

Hu, Z., Lu, Z., Song, B., Quan, Y., 2021. Impact of test cycle on mass, number and particle size distribution of particulates emitted from gasoline direct injection vehicles. Sci. Total Environ. 762, 143128. https://doi.org/10.1016/j.scitotenv.2020.143128.

Huang, W., Moon, S., Wang, J., Murayama, K., Arima, T., Sasaki, Y., Arioka, A., 2020. Nozzle tip wetting in gasoline direct injection injector and its link with nozzle internal flow. Int. J. Engine Res. 21 (2), 340–351. https://doi.org/10.1177/1468087419869774.

Huang, W., Gong, H., Moon, S., Wang, J., Murayama, K., Taniguchi, H., Sasaki, Y., 2021. Nozzle tip wetting in GDI injector at flash-boiling conditions. Int. J. Heat Mass Transf. 169, 120935. https://doi.org/10.1016/j.ijheatmasstransfer.2021.120935.

Hulskotte, J.H.J., Denier van der Gon, H.A.C., Visschedijk, A.J.H., Schaap, M., 2007. Brake wear from vehicles as an important source of diffuse copper pollution. Water Sci. Technol. 56 (1), 223–231. https://doi.org/10.2166/wst.2007.456.

Ikoma, T., Abe, S., Sonoda, Y., Suzuki, H., Suzuki, Y., Basaki, M., 2006. Development of V-6 3.5-liter engine adopting new direct injection system. SAE Technical Paper 2006-01-1259 https://doi.org/10.4271/2006-01-1259.

Imaoka, Y., Shouji, K., Inoue, T., Noda, T., 2015. A study of a multistage injection mechanism for improving the combustion of direct-injection gasoline engines. SAE Int. J. Engines 8 (3), 1080–1087.. https://www.jstor.org/stable/26278007.

Imaoka, Y., Hashizume, Y., Inoue, T., Shiraishi, T., 2019. A study of particulate emission formation mechanism from injector tip in direct-injection gasoline engines. SAE Int. J. Adv. Curr.Pract. Mobil. 2, 376–384. https://doi.org/10.4271/2019-01-2244 2019–01-2244.

Imoehl, W., Gestri, L., Maragliulo, M., Del-Frate, L., Klepatsch, M., Wildeson, R., 2012. A DOE approach to engine deposit testing used to optimize the design of a gasoline direct injector seat and orifice. SAE Int. J. Fuels Lubricants 5 (3), 1078–1095.. https://www.jstor.org/stable/26272831.

International Council on Clean Transportation, 2018. European vehicle market statistics 2018/2019. https://theicct.org/publications/european-vehicle-market-statistics-20182019.

IPCC, 2014. In: Pachauri, R.K., Meyer, L.A. (Eds.), Climate Change 2014: Synthesis Report. Contribution of Working Groups I, II and III to the Fifth Assessment Report of the Intergovernmental Panel on Climate Change. IPCC, Geneva, Switzerland 151 pp.

Iwamoto, Y., Noma, K., Nakayama, O., Yamauchi, T., Ando, H., 1997. Development of gasoline direct injection engine. SAE Trans., 777–793.. https://www.jstor.org/stable/44730720.

Jamadar, N.M., Jadhav, H.T., 2021. A case study on effective reduction in friction brake dust by adopting electric braking system. Life Cycl. Reliabil. Saf. Eng. 10 (1), 91–97. https://doi.org/10.1007/s41872-020-00154-9.

Jang, J., Lee, J., Choi, Y., Park, S., 2018. Reduction of particle emissions from gasoline vehicles with direct fuel injection systems using a gasoline particulate filter. Sci. Total Environ. 644, 1418–1428. https://doi.org/10.1016/j.scitotenv.2018.06.362.

Jeong, C.H., Hopke, P.K., Kim, E., Lee, D.W., 2004. The comparison between thermal-optical transmittance elemental carbon and aethalometer black carbon measured at multiple monitoring sites. Atmos. Environ. 38 (31), 5193–5204. https://doi.org/10.1016/j.atmosenv.2004.02.065.

Jiang, C., Xu, H., Srivastava, D., Ma, X., Dearn, K., Cracknell, R., Krueger-Venus, J., 2017. Effect of fuel injector deposit on spray characteristics, gaseous emissions and particulate matter in a gasoline direct injection engine. Appl. Energy 203, 390–402. https://doi.org/10.1016/j.apenergy.2017.06.020.

Jiang, C., Parker, M.C., Helie, J., Spencer, A., Garner, C.P., Wigley, G., 2019. Impact of gasoline direct injection fuel injector hole geometry on spray characteristics under flash boiling and ambient conditions. Fuel 241, 71–82. https://doi.org/10.1016/j.fuel.2018.11.143.

Jiao, Q., Reitz, R.D., 2015. The effect of operating parameters on soot emissions in GDI engines. SAE Int. J. Engines 8 (3), 1322–1333.. https://www.jstor.org/stable/26278030.

Johansson, K.O., Head-Gordon, M.P., Schrader, P.E., Wilson, K.R., Michelsen, H.A., 2018. Resonance-stabilized hydrocarbon-radical chain reactions may explain soot inception and growth. Science 361 (6406), 997–1000. https://doi.org/10.1126/science.aat3417.

Johnson, T., Joshi, A., 2018. Review of vehicle engine efficiency and emissions. SAE Int. J. Engines 11 (6), 1307–1330.. https://www.jstor.org/stable/26649163.

Joshi, A., Johnson, T.V., 2018. Gasoline particulate filters—a review. Emiss. Control Sci. Technol. 4 (4), 219–239. https://doi.org/10.1007/s40825-018-0101-y.

Jung, H., 2020. Fuel economy of plug-in hybrid electric and hybrid electric vehicles: effects of vehicle weight, hybridization ratio and ambient temperature. World Electr. Veh. J. 11 (2), 31. https://doi.org/10.3390/wevj11020031.

Jung, H., Kittelson, D.B., Zachariah, M.R., 2005. The influence of a cerium additive on ultrafine diesel particle emissions and kinetics of oxidation. Combust. Flame 142 (3), 276–288. https://doi.org/10.1016/j.combustflame.2004.11.015.

Kale, R., Banerjee, R., 2018. Investigation of macroscopic as well as microscopic spray behavior of multi-hole GDI injector under engine like hot injector body conditions. SAE Technical Paper 2018-01-0280 https://doi.org/10.4271/2018-01-0280.

Kamimoto, T., Uchida, N., Aizawa, T., Kondo, K., Kuboyama, T., 2017. Diesel flame imaging and quantitative analysis of in-cylinder soot oxidation. Int. J. Engine Res. 18 (5–6), 422–435. https://doi.org/10.1177/1468087416629282.

Karavalakis, G., Durbin, T.D., Yang, J., Ventura, L., Xu, K., 2018. Fuel Effects on PM Emissions From Different Vehicle/Engine Configurations: A Literature Review. SAE Technical Paper 2018-01-0349. https://doi.org/10.4271/2018-01-0349.

Karjalainen, P., Pirjola, L., Heikkilä, J., Lähde, T., Tzamkiozis, T., Ntziachristos, L., Rönkkö, T., 2014. Exhaust particles of modern gasoline vehicles: a laboratory and an on-road study. Atmos. Environ. 97, 262–270. https://doi.org/10.1016/j.atmosenv.2014.08.025.

Karjalainen, P., Timonen, H., Saukko, E., Kuuluvainen, H., Saarikoski, S., Aakko-Saksa, P., Rönkkö, T., 2016. Time-resolved characterization of primary particle emissions and secondary particle formation from a modern gasoline passenger car. Atmos. Chem. Phys. 16 (13), 8559–8570. https://doi.org/10.5194/acp-16-8559-2016.

Karl, G., Kemmler, R., Bargende, M., Abthoff, J., 1997. Analysis of a direct injected gasoline engine. SAE Trans., 835–847.. https://www.jstor.org/stable/44730725.

Kawaguchi, B., Umemoto, K., Misawa, S., Hirooka, S., Kawai, T., 2019. ICE vehicle challenge toward zero emissions: future technology harmonization in electrified powertrain system. SAE Technical Paper 2019-01-2217 https://doi.org/10.4271/2019-01-2217.

Kayes, D., Hochgreb, S., 1999. Mechanisms of particulate matter formation in spark-ignition engines. 1. Effect of engine operating conditions. Environ. Sci. Technol. 33 (22), 3957–3967. https://doi.org/10.1021/es9810991.

Ketterer, J.E., Cheng, W.K., 2014. On the nature of particulate emissions from DISI engines at cold-fast-idle. SAE Int. J. Engines 7 (2), 986–994.. https://www.jstor.org/stable/26277817.

Khair, M.K., 2003. A review of diesel particulate filter technologies. SAE Technical Paper 2003-01-2303 https://doi.org/10.4271/2003-01-2303.

Khalek, I., 2005. E-66 - Phase 1. Diesel particulate measurement research. Final Report. Coordinating Research Council . http://crcsite.wpengine.com/wp-content/uploads/2019/05/Final-Rport-10415-Project-E-66-Phase-1-R3.pdf.

Khalek, I.A., Bougher, T.L., Merritt, P.M., Zielinska, B., 2011. Regulated and unregulated emissions from highway heavy-duty diesel engines complying with US Environmental Protection Agency 2007 emissions standards. J. Air Waste Manage. Assoc. 61 (4), 427–442. https://doi.org/10.3155/1047-3289.61.4.427.

Khosousi, A., Liu, F., Dworkin, S.B., Eaves, N.A., Thomson, M.J., He, X., Wang, J., 2015. Experimental and numerical study of soot formation in laminar coflow diffusion flames of gasoline/ethanol blends. Combust. Flame 162 (10), 3925–3933. https://doi.org/10.1016/j.combustflame.2015.07.029.

Kim, C.H., Perry, K., Viola, M., Li, W., Narayanaswamy, K., 2011. Three-way catalyst design for urealess passive ammonia SCR: lean-burn SIDI aftertreatment system. SAE Technical Paper 2011-01-0306 https://doi.org/10.4271/2011-01-0306.

Kinoshita, M., Saito, A., Matsushita, S., Shibata, H., Niwa, Y., 1999. A method for suppressing formation of deposits on fuel injector for direct injection gasoline engine. SAE Trans., 2177–2184.. https://www.jstor.org/stable/44716836.

Kleeman, M.J., Riddle, S.G., Robert, M.A., Jakober, C.A., 2008. Lubricating oil and fuel contributions to particulate matter emissions from light-duty gasoline and heavy-duty diesel vehicles. Environ. Sci. Technol. 42 (1), 235–242. https://doi.org/10.1021/es071054c.

Kole, P.J., Löhr, A.J., Van Belleghem, F.G., Ragas, A.M., 2017. Wear and tear of tyres: a stealthy source of microplastics in the environment. Int. J. Environ. Res. Public Health 14 (10), 1265. https://doi.org/10.3390/ijerph14101265.

Köpple, F., Seboldt, D., Jochmann, P., Hettinger, A., Kufferath, A., Bargende, M., 2014. Experimental investigation of fuel impingement and spray-cooling on the piston of a GDI engine via instantaneous surface temperature measurements. SAE Int. J. Engines 7 (3), 1178–1194.. https://www.jstor.org/stable/26277834.

Kosaka, H., Aizawa, T., Kamimoto, T., 2005. Two-dimensional imaging of ignition and soot formation processes in a diesel flame. Int. J. Engine Res. 6 (1), 21–42. https://doi.org/10.1243/146808705X7347.

Kuwahara, K., Ueda, K., Ando, H., 1998. Mixing control strategy for engine performance improvement in a gasoline direct injection engine, SAE Technical Paper 980158. https://www.jstor.org/stable/44736524.

Lambert, C.K., Bumbaroska, M., Dobson, D., Hangas, J., Pakko, J., Tennison, P., 2016. Analysis of high mileage gasoline exhaust particle filters. SAE Int. J. Engines 9 (2), 1296–1304.. https://www.jstor.org/stable/26284898.

Lambert, C., Chanko, T., Dobson, D., Liu, X., Pakko, J., 2017a. Gasoline particle filter development. Emiss. Control Sci. Technol. 3 (1), 105–111. https://doi.org/10.1007/s40825-016-0055-x.

Lambert, C.K., Chanko, T., Jagner, M., Hangas, J., Liu, X., Pakko, J., Kamp, C.J., 2017b. Analysis of ash in low mileage, rapid aged, and high mileage gasoline exhaust particle filters. SAE Int. J. Engines 10 (4), 1595–1603.. https://www.jstor.org/stable/26422550.

Leach, F., Stone, R., Fennell, D., Hayden, D., Richardson, D., Wicks, N., 2017. Predicting the particulate matter emissions from spray-guided gasoline direct-injection spark ignition engines. Proc. Inst. Mech. Eng. D 231 (6), 717–730. https://doi.org/10.1177/0954407016657453.

Leach, F., Knorsch, T., Laidig, C., Wiese, W., 2018. A review of the requirements for injection systems and the effects of fuel quality on particulate emissions from GDI engines. SAE Technical Paper 2018-01-1710 https://doi.org/10.4271/2018-01-1710.

Leach, F., Chapman, E., Jetter, J., Rubino, L., Christensen, E., St John, P., McCormick, R., 2022. A review and perspective on particulate matter indices linking fuel composition to particulate emissions from gasoline engines. SAE Int. J. Fuels Lubricants 15 (1). https://doi.org/10.4271/04-15-01-0001.

Leick, P., Bork, B., Geiler, J.N., 2018. Experimental characterization of tip wetting in gasoline DI injectors. 14th Triennial International Conference on Liquid Atomization and Spray Systems.

Lewis, A., Moller, S.J., Carslaw, D., 2019. Non-exhaust emissions from road traffic. Research Report. Defra , United Kingdom. https://eprints.whiterose.ac.uk/156628/.

Li, X., Sun, Z., Yang, S., Wang, H., Nour, M., 2021. Flash boiling combustion of isomeric butanol and gasoline surrogate blends using constant volume spray chamber and GDI optical engine. Fuel 286, 119328. https://doi.org/10.1016/j.fuel.2020.119328.

Liggio, J., Gordon, M., Smallwood, G., Li, S.M., Stroud, C., Staebler, R., Brook, J.R., 2012. Are emissions of black carbon from gasoline vehicles underestimated? Insights from near and on-road measurements. Environ. Sci. Technol. 46 (9), 4819–4828. https://doi.org/10.1021/es2033845.

Liu, X., Chanko, T., Lambert, C., Maricq, M., 2018. Gasoline particulate filter efficiency and backpressure at very low mileage. SAE Technical Paper 2018-01-1259 https://doi.org/10.4271/2018-01-1259.

Liu, X., Szente, J., Pakko, J., Lambert, C., Maricq, M., 2019. Using artificial ash to improve GPF performance at zero mileage. SAE Technical Paper. 2019-01-0974 https://doi.org/10.4271/2019-01-0974.

Liu, H., Li, Z., Xu, H., Ma, X., Shuai, S., 2020. Nucleation mode particle evolution in a gasoline direct injection engine with/without a three-way catalyst converter. Appl. Energy 259, 114211. https://doi.org/10.1016/j.apenergy.2019.114211.

Liu, H., Li, Z., Zhang, M., Xu, H., Ma, X., Shuai, S., 2021. Exhaust non-volatile particle filtration characteristics of three-way catalyst and influencing factors in a gasoline direct injection engine compared to gasoline particulate filter. Fuel 290, 120065. https://doi.org/10.1016/j.fuel.2020.120065.

Lowry, D., Lanoiselle, M.E., Fisher, R.E., et al., 2016. Marked long-term decline in ambient CO mixing ratio in SE England, 1997–2014: evidence of policy success in improving air quality. Sci. Rep. 6, 25661. https://doi.org/10.1038/srep25661.

Lubkowitz, J., Meneghini, R., 2018. Enhanced speciation of gasoline. Coordinating Research Council Project AVFL-29. http://crcsite.wpengine.com/wp-content/uploads/2019/05/CRC-Project-AVFL-29-Final-Report_June-2018-1.pdf.

Luo, Y., Zhu, L., Fang, J., Zhuang, Z., Guan, C., Xia, C., Huang, Z., 2015. Size distribution, chemical composition and oxidation reactivity of particulate matter from gasoline direct injection (GDI) engine fueled with ethanol-gasoline fuel. Appl. Therm. Eng. 89, 647–655. https://doi.org/10.1016/j.applthermaleng.2015.06.060.

Mamakos, A., Arndt, M., Hesse, D., Augsburg, K., 2019. Physical characterization of brake-wear particles in a PM10 dilution tunnel. Atmosphere 10 (11), 639. https://doi.org/10.3390/atmos10110639.

Maricq, M.M., 2014. Examining the relationship between black carbon and soot in flames and engine exhaust. Aerosol Sci. Technol. 48, 620–629. https://doi.org/10.1080/02786826.2014.904961.

Maricq, M.M., Podsiadlik, D.H., Brehob, D.D., Haghgooie, M., 1999. Particulate emissions from a direct-injection spark-ignition (DISI) engine. SAE Technical Paper 1999-01-1530 https://doi.org/10.4271/1999-01-1530.

Maricq, M.M., Podsiadlik, D.H., Chase, R.E., 1999b. Examination of the size-resolved and transient nature of motor vehicle particle emissions. Environ. Sci. Technol. 33, 1618–1626. https://doi.org/10.1021/es9808806.

Maricq, M.M., Harris, S.J., Szente, J.J., 2003. Soot size distributions in rich premixed ethylene flames. Combust. Flame 132 (3), 328–342. https://doi.org/10.1016/S0010-2180(02)00502-3.

Maricq, M.M., Szente, J.J., Jahr, K., 2012. The impact of ethanol fuel blends on PM emissions from a light-duty GDI vehicle. Aerosol Sci. Technol. 46 (5), 576–583. https://doi.org/10.1080/02786826.2011.648780.

Maricq, M.M., Szente, J.J., Adams, J., Tennison, P., Rumpsa, T., 2013. Influence of mileage accumulation on the particle mass and number emissions of two gasoline direct injection vehicles. Environ. Sci. Technol. 47 (20), 11890–11896. https://doi.org/10.1021/es402686z.

Maricq, M.M., Szente, J.J., Harwell, A.L., Loos, M.J., 2017. Impact of aggressive drive cycles on motor vehicle exhaust PM emissions. J. Aerosol Sci. 113, 1–11. https://doi.org/10.1016/j.jaerosci.2017.07.005.

Martinez, J., 2021. Great smog of London, encyclopedia britannica. https://www.britannica.com/event/Great-Smog-of-London.

Mathissen, M., Grochowicz, J., Schmidt, C., Vogt, R., zum Hagen, F.H.F., Grabiec, T., Grigoratos, T., 2018. A novel real-world braking cycle for studying brake wear particle emissions. Wear 414, 219–226. https://doi.org/10.1016/j.wear.2018.07.020.

Mazzoleni, C., Moosmüller, H., Kuhns, H.D., Keislar, R.E., Barber, P.W., Nikolic, D., Watson, J.G., 2004. Correlation between automotive CO, HC, NO, and PM emission factors from on-road remote sensing: implications for inspection and maintenance programs. Transp. Res. Part D: Transp. Environ. 9 (6), 477–496. https://doi.org/10.1016/j.trd.2004.08.006.

McCaffery, C., Zhu, H., Li, C., Durbin, T.D., Johnson, K.C., Jung, H., Karavalakis, G., 2020. On-road gaseous and particulate emissions from GDI vehicles with and without gasoline particulate filters (GPFs) using portable emissions measurement systems (PEMS). Sci. Total Environ. 710, 136366. https://doi.org/10.1016/j.scitotenv.2019.136366.

McDonald, B.C., De Gouw, J.A., Gilman, J.B., Jathar, S.H., Akherati, A., Cappa, C.D., Trainer, M., 2018. Volatile chemical products emerging as largest petrochemical source of urban organic emissions. Science 359 (6377), 760–764. https://doi.org/10.1126/science.aaq0524.

McDuffie, E., Martin, R.V., Yin, H., Brauer, M., 2021. Global burden of disease from major air pollution sources (GBD maps): A global approach. Health Effects Institute, Research Report. 210.

McEnally, C.S., Pfefferle, L.D., 2007a. Improved sooting tendency measurements for aromatic hydrocarbons and their implications for naphthalene formation pathways. Combust. Flame 148 (4), 210–222. https://doi.org/10.1016/j.combustflame.2006.11.003.

McEnally, C.S., Pfefferle, L.D., 2007b. The effects of dimethyl ether and ethanol on benzene and soot formation in ethylene nonpremixed flames. Proc. Combust. Inst. 31 (1), 603–610. https://doi.org/10.1016/j.proci.2006.07.005.

Medina, M., Fatouraie, M., Wooldridge, M., 2018. High-speed imaging studies of gasoline fuel sprays at fuel injection pressures from 300 to 1500 bar. SAE Technical Paper 2018-01-0294 https://doi.org/10.4271/2018-01-0294.

Medina, M., Zhou, Y., Fatouraie, M., Wooldridge, M., 2020. High-speed imaging study on the effects of internal geometry on high-pressure gasoline sprays. SAE Technical Paper 2020-01-2111 https://doi.org/10.4271/2020-01-2111.

Medina, M., Alzahrani, F.M., Fatouraie, M., Wooldridge, M.S., Sick, V., 2021a. Mechanisms of fuel injector tip wetting and tip drying based on experimental measurements of engine-out particulate emissions from gasoline direct-injection engines. Int. J. Engine Res. 22 (6), 2035–2053. https://doi.org/10.1177/1468087420916052.

Medina, M., Bautista, A., Wooldridge, M., Payri, R., 2021b. The effects of injector geometry and operating conditions on spray mass, momentum and development using high-pressure gasoline. Fuel 294, 120468. https://doi.org/10.1016/j.fuel.2021.120468.

Meyer, R., Yilmaz, E., Heywood, J.B., 1998. Liquid fuel flow in the vicinity of the intake valve of a port-injected SI engine. SAE Trans., 1070–1090.. https://www.jstor.org/stable/44746518.

Mitroglou, N., Nouri, J.M., Yan, Y., Gavaises, M., Arcoumanis, C., 2007. Spray structure generated by multi-hole injectors for gasoline direct-injection engines. SAE Technical Paper, 2007-01-1417 https://doi.org/10.4271/2007-01-1417.

Miyashita, K., Tsukamoto, T., Fukuda, Y., Kondo, K., Aizawa, T., 2016. High-speed UV and visible laser shadowgraphy of GDI in-cylinder pool fire. SAE Technical Paper, 2016-01-2165 https://doi.org/10.4271/2016-01-2165.

Monroe, R., Studzinski, W., Parsons, J., La, C., et al., 2021. Engine particulate emissions as a function of gasoline deposit control additive. SAE Int. J. Fuels Lubr. 14 (1), 3–11. https://doi.org/10.4271/04-14-01-0001.

Montanaro, A., Allocca, L., Lazzaro, M., 2017. Iso-octane spray from a GDI multi-hole injector under non-and flash boiling conditions. SAE Technical Paper 2017-01-2319 https://doi.org/10.4271/2017-01-2319.

Montanaro, A., Allocca, L., Meccariello, G., 2020. Effects of Ultra-High Injection Pressures up to 100 MPa on Gasoline Spray Morphology. SAE Technical Paper. 2020-01-0320. https://doi.org/10.4271/2020-01-0320.

Moon, S., Huang, W., Wang, J., 2020. Spray formation mechanism of diverging-tapered-hole GDI injector and its potentials for GDI engine applications. Fuel 270, 117519. https://doi.org/10.1016/j.fuel.2020.117519.

Morgan, P., Lobato, P., Premnath, V., Kroll, S., 2014. Evaluation and investigation of gaseous and particulate emissions on sidi in-use vehicles with higher ethanol blend fuels. Coordinating Research Council Project E-94-1. http://crcsite.wpengine.com/wp-content/uploads/2019/05/03-17589_CRC-E94-1_Final-Report_6-2-2014_Lobato_Morgan.pdf.

Morgan, P., Smith, I., Premnath, V., Kroll, S., Crawford, R., 2017. Evaluation and investigation of fuel effects on gaseous and particulate emissions on sidi in-use vehicles. Coordinating Research Council Project E-94-2. http://crcsite.wpengine.com/wp-content/uploads/2019/05/CRC_2017-3-21_03-20955_E94-2FinalReport-Rev1b.pdf.

Morgan, P., Lobato, P., Premnath, V., Kroll, S., Brunner, K., Crawford, R., 2018. Impacts of splash-blending on particulate emissions for sidi engines. Coordinating Research Council Project E-94-3. http://crcsite.wpengine.com/wp-content/uploads/2019/05/CRC-E-94-3_Final-Report_2018-06-26.pdf.

Moses-DeBusk, M., Storey, J.M., Eibl, M.A., Thomas, J.F., Toops, T.J., Finney, C.E., Gregor, J., 2020. Nonuniform oxidation behavior of loaded gasoline particulate filters. Emiss. Control Sci. Technol. 6 (3), 301–314. https://doi.org/10.1007/s40825-020-00166-y.

Mu, M., Sjöblom, J., Ström, H., Li, X., 2019a. Analysis of the flow field from connection cones to monolith reactors. Energies 12 (3), 455. https://doi.org/10.3390/en12030455.

Mu, M., Sjöblom, J., Sharma, N., Ström, H., Li, X., 2019b. Experimental study on the flow field of particles deposited on a gasoline particulate filter. Energies 12 (14), 2701. https://doi.org/10.3390/en12142701.

Myung, C.L., Park, S., 2012. Exhaust nanoparticle emissions from internal combustion engines: a review. Int. J. Automot. Technol. 13, 9. https://doi.org/10.1007/s12239-012-0002-y.

Myung, C.L., Ko, A., Park, S., 2014. Review on characterization of nano-particle emissions and pm morphology from internal combustion engines: part 1. Int. J. Auto. Technol. 15, 203–218. https://doi.org/10.1007/s12239-014-0022-x.

Myung, C.L., Kim, J., Jang, W., Jin, D., Park, S., Lee, J., 2015. Nanoparticle filtration characteristics of advanced metal foam media for a spark ignition direct injection engine in steady engine operating conditions and vehicle test modes. Energies 8 (3), 1865–1881. https://doi.org/10.3390/en8031865.

Nassar, A.M., Ahmed, N.S., El-shazly, R.I., 2017. Preparation and evaluation of the mixtures of sulfonate and phenate as lube oil additives. Int. J. Ind. Chem. 8 (4), 383–395. https://doi.org/10.1007/s40090-017-0128-x.

Niemann, H., Winner, H., Asbach, C., Kaminski, H., Frentz, G., Milczarek, R., 2020. Influence of disc temperature on ultrafine, fine, and coarse particle emissions of passenger car disc brakes with organic and inorganic pad binder materials. Atmosphere 11 (10), 1060. https://doi.org/10.3390/atmos11101060.

Ntziachristos, L., Boulter, P., 2013. Road vehicle tyre and brake wear. Road surface wear. EMEP/EEA Emission Inventory Guidebook.

O'Connor, J., Musculus, M., 2014. In-cylinder mechanisms of soot reduction by close-coupled post-injections as revealed by imaging of soot luminosity and planar laser-induced soot incandescence in a heavy-duty diesel engine. SAE Int. J. Engines 7 (2), 673–693.. https://www.jstor.org/stable/26277795.

Odum, J.R., Jungkamp, T.P.W., Griffin, R.J., Flagan, R.C., Seinfeld, J.H., 1997. The atmospheric aerosol-forming potential of whole gasoline vapor. Science 276 (5309), 96–99. https://doi.org/10.1126/science.276.5309.96.

Oh, C., Cheng, W.K., 2017. Assessment of gasoline direct injection engine cold start particulate emission sources. SAE Int. J. Engines 10 (4), 1556–1565.. https://www.jstor.org/stable/26422545.

Oh, H., Lee, J., Han, S., Park, C., Bae, C., Lee, J., Kim, S.J., 2017. Effect of injector nozzle hole geometry on particulate emissions in a downsized direct injection gasoline engine. SAE Technical Paper 2017-24-0111 https://doi.org/10.4271/2017-24-0111.

Oroumiyeh, F., Zhu, Y., 2021. Brake and tire particles measured from on-road vehicles: effects of vehicle mass and braking intensity. Atmos. Environ. X 12, 100121. https://doi.org/10.1016/j.aeaoa.2021.100121.

Ou, Q., Maricq, M.M., Pakko, J., Chanko, T.B., Pui, D.Y., 2019. Design and evaluation of a sintered metal fiber filter for gasoline direct injection engine exhaust aftertreatment. J. Aerosol Sci. 133, 12–23. https://doi.org/10.1016/j.jaerosci.2019.04.003.

Panko, J., Kreider, M., Unice, K., 2018. Review of tire wear emissions: a review of tire emission measurement studies: identification of gaps and future needs. Non-exhaust Emiss. 147–160. https://doi.org/10.1016/B978-0-12-811770-5.00007-8.

Panko, J.M., Hitchcock, K.M., Fuller, G.W., Green, D., 2019. Evaluation of tire wear contribution to PM2. 5 in urban environments. Atmosphere 10 (2), 99. https://doi.org/10.3390/atmos10020099.

Park, C., Kook, S., Bae, C., 2004. Effects of multiple injections in a HSDI diesel engine equipped with common rail injection system. SAE Technical Paper 2004-01-0127 https://doi.org/10.4271/2004-01-0127.

Park, C., Kim, S., Kim, H., Moriyoshi, Y., 2012. Stratified lean combustion characteristics of a spray-guided combustion system in a gasoline direct injection engine. Energy 41 (1), 401–407. https://doi.org/10.1016/j.energy.2012.02.060.

Pauly, T., Franoschek, S., Hoyer, R., Eckhoff, S., 2010. Cost and fuel economy driven aftertreatment solutions-for lean GDI. SAE Technical Paper 2010-01-0363 https://doi.org/10.4271/2010-01-0363.

Payri, R., Salvador, F.J., Martí-Aldaraví, P., Vaquerizo, D., 2017. ECN spray G external spray visualization and spray collapse description through penetration and morphology analysis. Appl. Therm. Eng. 112, 304–316. https://doi.org/10.1016/j.applthermaleng.2016.10.023.

Peckham, M.S., Finch, A., Campbell, B., Price, P., Davies, M.T., 2011. Study of particle number emissions from a turbocharged gasoline direct injection (GDI) engine including data from a fast-response particle size spectrometer. SAE Technical Paper 2011-01-1224 https://doi.org/10.4271/2011-01-1224.

Perricone, G., Matějka, V., Alemani, M., Valota, G., Bonfanti, A., Ciotti, A., Ibrahim, M., 2018. A concept for reducing PM10 emissions for car brakes by 50%. Wear 396, 135–145. https://doi.org/10.1016/j.wear.2017.06.018.

Perricone, G., Alemani, M., Wahlström, J., Olofsson, U., 2019. A proposed driving cycle for brake emissions investigation for test stand. Proc. Inst. Mech. Eng. Part D 234 (1), 122–135. https://doi.org/10.1177/0954407019841222.

Petzold, A., Ogren, J.A., Fiebig, M., Laj, P., Li, S.M., Baltensperger, U., Zhang, X.Y., 2013. Recommendations for reporting" black carbon" measurements. Atmos. Chem. Phys. 13 (16), 8365–8379. https://doi.org/10.5194/acp-13-8365-2013.

Pickett, L.M., Siebers, D.L., 2004. Soot in diesel fuel jets: effects of ambient temperature, ambient density, and injection pressure. Combust. Flame 138 (1–2), 114–135. https://doi.org/10.1016/j.combustflame.2004.04.006.

Pieber, S.M., Kumar, N.K., Klein, F., Comte, P., Bhattu, D., Dommen, J., Prévôt, A.S., 2018. Gas-phase composition and secondary organic aerosol formation from standard and particle filter-retrofitted gasoline direct injection vehicles investigated in a batch and flow reactor. Atmos. Chem. Phys. 18 (13), 9929–9954. https://doi.org/10.5194/acp-18-9929-2018.

Pilbeam, J.J., Thomson, A.R., Sahu, A.B., Liu, H., Xu, H., 2020. Study of Effects of Deposit Formation on GDi Injector and Engine Performance. SAE Technical Paper 2020-01-2099. https://doi.org/10.4271/2020-01-2099.

Piock, W., Hoffmann, G., Berndorfer, A., Salemi, P., Fusshoeller, B., 2011. Strategies towards meeting future particulate matter emission requirements in homogeneous gasoline direct injection engines. SAE Int. J. Engines 4 (1), 1455–1468.. https://www.jstor.org/stable/26278235.

Piock, W.F., Befrui, B., Berndorfer, A., Hoffmann, G., 2015. Fuel pressure and charge motion effects on GDi engine particulate emissions. SAE Int. J. Engines 8 (2), 464–473.. https://www.jstor.org/stable/26277960.

Pirjola, L., Karjalainen, P., Heikkila, J., Saari, S., Tzamkiozis, T., Ntziachristos, L., Ronkko, T., 2015. Effects of fresh lubricant oils on particle emissions emitted by a modern gasoline direct injection passenger car. Environ. Sci. Technol. 49 (6), 3644–3652. https://doi.org/10.1021/es505109u.

Platt, S.M., El Haddad, I., Pieber, S.M., Zardini, A.A., Suarez-Bertoa, R., Clairotte, M., Prévôt, A.S.H., 2017. Gasoline cars produce more carbonaceous particulate matter than modern filter-equipped diesel cars. Sci. Rep. 7 (1), 1–9. https://doi.org/10.1038/s41598-017-03714-9.

Pope III, C.A., 1989. Respiratory disease associated with community air pollution and a steel mill, Utah Valley. AJPH 79, 623–628. https://doi.org/10.2105/AJPH.79.5.623.

Pratama, R.H., Huang, W., Moon, S., Wang, J., Murayama, K., Taniguchi, H., Arioka, A., 2022. Hydraulic flip in a gasoline direct injection injector and its effect on injected spray. Fuel 310, 122303. https://doi.org/10.1016/j.fuel.2021.122303.

Premnath, V., Khalek, I., Morgan, P., Michlberger, A., Sutton, M., Vincent, P., 2018. Effect of Lubricant Oil on Particle Emissions From a Gasoline Direct Injection Light-duty Vehicle. SAE Technical Paper 2018-01-1708. https://doi.org/10.4271/2018-01-1708.

Preston, B., 2021. Some newer cars can burn lots of oil. Consumer Reports (see also August 2015 issue). https://www.consumerreports.org/car-maintenance/some-newer-cars-can-burn-lots-of-oil-a1065338868/.

Qian, Y., Li, Z., Yu, L., Wang, X., Lu, X., 2019. Review of the state-of-the-art of particulate matter emissions from modern gasoline fueled engines. Appl. Energy 238, 1269–1298. https://doi.org/10.1016/j.apenergy.2019.01.179.

Rakov, V., 2020. Determination of optimal characteristics of braking energy recovery system in vehicles operating in urban conditions. Transp. Res. Procedia 50, 566–573. https://doi.org/10.1016/j.trpro.2020.10.068.

Ratcliff, M.A., Windom, B., Fioroni, G.M., John, P.S., Burke, S., Burton, J., McCormick, R.L., 2019. Impact of ethanol blending into gasoline on aromatic compound evaporation and particle emissions from a gasoline direct injection engine. Appl. Energy 250, 1618–1631. https://doi.org/10.1016/j.apenergy.2019.05.030.

Rathod, D., Onori, S., Filipi, Z., Hoffman, M., 2018. Experimental investigation of soot accumulation and regeneration in a catalyzed Gasoline Particulate Filter utilizing particulate quantification and gas speciation measurements. Internal Combustion Engine Division Fall Technical Conference. 51999. American Society of Mechanical Engineers. https://doi.org/10.1115/ICEF2018-9627.

Raza, M., Chen, L., Leach, F., Ding, S., 2018. A review of particulate number (PN) emissions from gasoline direct injection (GDI) engines and their control techniques. Energies 11 (6), 1417. https://doi.org/10.3390/en11061417.

Requia, W.J., Mohamed, M., Higgins, C.D., Arain, A., Ferguson, M., 2018. How clean are electric vehicles? Evidence-based review of the effects of electric mobility on air pollutants, greenhouse gas emissions and human health. Atmos. Environ. 185, 64–77. https://doi.org/10.1016/j.atmosenv.2018.04.040.

Ristovski, Z.D., Morawska, L., Bofingeer, N.D., Hitchins, J., 1998. Submicrometer and supermicrometer particulate emission from spark ignition vehicles. Environ. Sci. Technol. 32, 3845–3852. https://doi.org/10.1021/es980102d.

Robert, M.A., VanBergen, S., Kleeman, M.J., Jakober, C.A., 2007. Size and composition distributions of particulate matter emissions: part 1—Light-duty gasoline vehicles. J. Air Waste Manage. Assoc. 57 (12), 1414–1428. https://doi.org/10.3155/1047-3289.57.12.1414.

Robinson, A.L., Donahue, N.M., Shrivastava, M.K., Weitkamp, E.A., Sage, A.M., Grieshop, A.P., Pandis, S.N., 2007. Rethinking organic aerosols: semivolatile emissions and photochemical aging. Science 315 (5816), 1259–1262. https://doi.org/10.1126/science.1133061.

Rodriguez, J.F., Cheng, W.K., 2015. Effect of operation strategy on first cycle CO, HC, and PM/PN emissions in a GDI engine. SAE Int. J. Engines 8 (3), 1098–1106.. https://www.jstor.org/stable/26278009.

Rodriguez, J.F., Cheng, W.K., 2016a. Cycle-by-cycle analysis of cold crank-start in a GDI engine. SAE Int. J. Engines 9, 1210–1219.. https://www.jstor.org/stable/26284890.

Rodriguez, J.F., Cheng, W.K., 2016b. Reduction of cold-start emissions through valve timing in a GDI engine. SAE Int. J. Engines 9 (2), 1220–1229.. https://www.jstor.org/stable/26284891.

Rokosz, M.J., Chen, A.E., Lowe-Ma, C.K., Kucherov, A.V., Benson, D., Peck, M.P., McCabe, R.W., 2001. Characterization of phosphorus-poisoned automotive exhaust catalysts. Appl. Catal. B Environ. 33 (3), 205–215. https://doi.org/10.1016/S0926-3373(01)00165-5.

Rönkkö, T., Virtanen, A., Kannosto, J., Keskinen, J., Lappi, M., Pirjola, L., 2007. Nucleation mode particles with a nonvolatile core in the exhaust of a heavy duty diesel vehicle. Environ. Sci. Technol. 41 (18), 6384–6389. https://doi.org/10.1021/es0705339.

Roth, P., Yang, J., Fofie, E., Cocker III, D.R., Durbin, T.D., Brezny, R., Karavalakis, G., 2019. Catalyzed gasoline particulate filters reduce secondary organic aerosol production from gasoline direct injection vehicles. Environ. Sci. Technol. 53 (6), 3037–3047. https://doi.org/10.1021/acs.est.8b06418.

Rothbart, M., 2020. E-fuel production via renewables and the impact on the in-use CO2 performance. SAE Technical Paper 2020-01-2139 https://doi.org/10.4271/2020-01-2139.

Rubino, L., Thomson, M.J., 1999. The effect of oxygenated additives on soot precursor formation in a counterflow diffusion flame. SAE Technical Paper 1999-01-3589 https://doi.org/10.4271/1999-01-3589.

Rubino, L., Thier, D., Schumann, T., Guettler, S., Russ, G., 2017. Fundamental study of GPF performance on soot and ash accumulation over artemis urban and motorway cycles-comparison of engine bench results with GPF durability study on road. SAE Technical Paper, 24-0127 https://doi.org/10.4271/2017-24-0127.

Saffaripour, M., Chan, T.W., Liu, F., Thomson, K.A., Smallwood, G.J., Kubsh, J., Brezny, R., 2015. Effect of drive cycle and gasoline particulate filter on the size and morphology of soot particles emitted from a gasoline-direct-injection vehicle. Environmental science & technology 49 (19), 11950–11958. https://doi.org/10.1021/acs.est.5b02185.

Sakai, S., Rothamer, D., 2019. Impact of ethanol blending on particulate emissions from a spark-ignition direct-injection engine. Fuel 236, 1548–1558. https://doi.org/10.1016/j.fuel.2018.09.037.

Salamanca, M., Sirignano, M., Commodo, M., Minutolo, P., D'anna, A., 2012. The effect of ethanol on the particle size distributions in ethylene premixed flames. Exp. Thermal Fluid Sci. 43, 71–75. https://doi.org/10.1016/j.expthermflusci.2012.04.006.

Saliba, G., Saleh, R., Zhao, Y., Presto, A.A., Lambe, A.T., Frodin, B., Robinson, A.L., 2017. Comparison of gasoline direct-injection (GDI) and port fuel injection (PFI) vehicle emissions: emission certification standards, cold-start, secondary organic aerosol formation potential, and potential climate impacts. Environ. Sci. Technol. 51 (11), 6542–6552. https://doi.org/10.1021/acs.est.6b06509.

Samaras, Z.C., Andersson, J., Bergmann, A., Hausberger, S., Toumasatos, Z., Keskinen, J., Bainschab, M., 2020. Measuring Automotive exhaust particles Down to 10 nm. European Commission, Horizon 2020 H2020-GV-02-2016 GA No. 724085.

Samuel, S., Austin, L., Morrey, D., 2002. Automotive test drive cycles for emission measurement and real-world emission levels-a review. Proc. Inst. Mech. Eng. D 216 (7), 555–564. https://doi.org/10.1243/095440702760178587.

Sanders, P.G., Xu, N., Dalka, T.M., Maricq, M.M., 2003. Airborne brake wear debris: size distributions, composition, and a comparison of dynamometer and vehicle tests. Environ. Sci. Technol. 37 (18), 4060–4069. https://doi.org/10.1021/es034145s.

Santoro, R.J., Yeh, T.T., Horvath, J.J., Semerjian, H.G., 1987. The transport and growth of soot particles in laminar diffusion flames. Combust. Sci. Technol. 53 (2–3), 89–115. https://doi.org/10.1080/00102208708947022.

Seinfeld, J.H., Pandis, S.N., 2016. Atmospheric Chemistry and Physics: From Air Pollution to Climate Change. 3rd edition. Wiley.

Senecal, P.K., Leach, F., 2019. Diversity in transportation: why a mix of propulsion technologies is the way forward for the future fleet. Results Eng. 4, 100060. https://doi.org/10.1016/j.rineng.2019.100060.

Seong, H., Choi, S., Lee, K., 2014. Examination of nanoparticles from gasoline direct-injection (GDI) engines using transmission electron microscopy (TEM). Int. J. Automot. Technol. 15 (2), 175–181. https://doi.org/10.1007/s12239-014-0019-5.

Seong, H., Choi, S., Matusik, K.E., Kastengren, A.L., Powell, C.F., 2019. 3D pore analysis of gasoline particulate filters using X-ray tomography: impact of coating and ash loading. J. Mater. Sci. 54 (8), 6053–6065. https://doi.org/10.1007/s10853-018-03310-w.

Shanahan, C.S., Smith, S.S., Sears, B.D., 2017. A general method for fouling injectors in gasoline direct injection vehicles and the effects of deposits on vehicle performance. SAE Int. J. Fuels Lubr. 10 (3), 778–788.. https://www.jstor.org/stable/26390380.

Shao, H., Lam, W., Remias, J., Roos, J., Choi, S., Seong, H., 2016. Effect of lubricant oil properties on the performance of gasoline particulate filter (GPF). SAE Int. J. Fuels Lubr. 9 (3), 650–658.. https://www.jstor.org/stable/26273494.

Shuai, S., Ma, X., Li, Y., Qi, Y., Xu, H., 2018. Recent progress in automotive gasoline direct injection engine technology. Autom. Innov. 1, 95–113. https://doi.org/10.1007/s42154-018-0020-1.

Siebers, D., Higgins, B., 2001. Flame lift-off on direct-injection diesel sprays under quiescent conditions. SAE Trans., 400–421.. https://www.jstor.org/stable/44724317.

Simons, A., 2016. Road transport: new life cycle inventories for fossil-fuelled passenger cars and non-exhaust emissions in ecoinvent v3. Int. J. Life Cycle Assess. 21 (9), 1299–1313. https://doi.org/10.1007/s11367-013-0642-9.

Slavchov, R.I., Mosbach, S., Kraft, M., Pearson, R., Filip, S.V., 2018. An adsorption-precipitation model for the formation of injector external deposits in internal combustion engines. Appl. Energy 228, 1423–1438. https://doi.org/10.1016/j.apenergy.2018.06.130.

Snelling, D.R., Thomson, K.A., Smallwood, G.J., Gülder, Ö.L., 1999. Two-dimensional imaging of soot volume fraction in laminar diffusion flames. Appl. Opt. 38 (12), 2478–2485. https://doi.org/10.1364/AO.38.002478.

Sommer, F., Dietze, V., Baum, A., Sauer, J., Gilge, S., Maschowski, C., Gieré, R., 2018. Tire abrasion as a major source of microplastics in the environment. Aerosol Air Qual. Res. 18 (8), 2014–2028. https://doi.org/10.4209/aaqr.2018.03.0099.

Song, J., Park, S., 2015. Effect of injection strategy on the spray development process in a single-cylinder optical GDI engine. Atomization Sprays 25, 819–836. https://doi.org/10.1615/AtomizSpr.2015012018.

Song, J., Lee, Z., Song, J., Park, S., 2018. Effects of injection strategy and coolant temperature on hydrocarbon and particulate emissions from a gasoline direct injection engine with high pressure injection up to 50 MPa. Energy 164, 512–522. https://doi.org/10.1016/j.energy.2018.09.011.

Stevens, E., Steeper, R., 2001. Piston wetting in an optical DISI engine: fuel films, pool fires, and soot generation. SAE Trans., 1287–1294.. https://www.jstor.org/stable/44724397.

Stumpp, G., Ricco, M., 1996. Common rail—an attractive fuel injection system for passenger car DI diesel engines. SAE Technical Paper, 960870.

Su, J., Xu, M., Yin, P., Gao, Y., Hung, D., 2015. Particle number emissions reduction using multiple injection strategies in a boosted spark-ignition direct-injection (SIDI) gasoline engine. SAE Int. J. Engines 8 (1), 20–29.. https://www.jstor.org/stable/26277913.

Suarez-Bertoa, R., Lähde, T., Pavlovic, J., Valverde, V., Clairotte, M., Giechaskiel, B., 2019. Laboratory and on-road evaluation of a GPF-equipped gasoline vehicle. Catalysts 9 (8), 678. https://doi.org/10.3390/catal9080678.

Sun, Z., Cui, M., Ye, C., Yang, S., Li, X., Hung, D., Xu, M., 2021. Split injection flash boiling spray for high efficiency and low emissions in a GDI engine under lean combustion condition. Proc. Combust. Inst. 38 (4), 5769–5779. https://doi.org/10.1016/j.proci.2020.05.037.

Swanson, J., Kittelson, D., 2010. Evaluation of thermal denuder and catalytic stripper methods for solid particle measurements. J. Aerosol Sci. 41 (12), 1113–1122. https://doi.org/10.1016/j.jaerosci.2010.09.003.

Szybist, J.P., Youngquist, A.D., Barone, T.L., Storey, J.M., Moore, W.R., Foster, M., Confer, K., 2011. Ethanol blends and engine operating strategy effects on light-duty spark-ignition engine particle emissions. Energy Fuel 25 (11), 4977–4985. https://doi.org/10.1021/ef201127y.

Timmers, V.R., Achten, P.A., 2016. Non-exhaust PM emissions from electric vehicles. Atmos. Environ. 134, 10–17. https://doi.org/10.1016/j.atmosenv.2016.03.017.

Timmers, V.R., Achten, P.A., 2018. Non-exhaust PM emissions from battery electric vehicles. Non-exhaust Emissions, pp. 261–287 https://doi.org/10.1016/B978-0-12-811770-5.00012-1.

Toll, M., 2018. Regenerative braking: how it works and is it worth it in small EVs? Electrek. https://electrek.co/2018/04/24/regenerative-braking-how-it-works/#:~:text=Efficiency%20of%20the%20regenerative%20braking,of%2060%2D70%25%20efficient.

Tutuianu, M., Bonnel, P., Ciuffo, B., Haniu, T., Ichikawa, N., Marotta, A., Steven, H., 2015. Development of the world-wide harmonized light duty test cycle (WLTC) and a possible pathway for its introduction in the european legislation. Transp. Res. Part D: Transp. Environ. 40, 61–75. https://doi.org/10.1016/j.trd.2015.07.011.

U.S. Department of Energy, 2022. Alternative Fuels Data Centerr: Renewable hydrocarbon biofuels. https://afdc.energy.gov/fuels/emerging_hydrocarbon.html.

U.S. Environmental Protection Agency, 1986. Air quality criteria for lead. EPA-600/8-83/028aF. 1.

U.S. Environmental Protection Agency, 2013. EPAct/V2/E-89 Tier 2 Gasoline Fuel Effects Study. https://www.epa.gov/moves/epactv2e-89-tier-2-gasoline-fuel-effects-study.

U.S. Environmental Protection Agency, 2014. Brake and tire wear emissions from on-road vehicles in MOVES2014. Technical report EPA-420-R-14-013. https://cfpub.epa.gov/si/si_public_file_download.cfm?p_download_id=525701.

U.S. Environmental Protection Agency, 2021a. Final rule to revise existing national GHG emissions standards for passenger cars and light trucks through model year 2026. https://www.epa.gov/regulations-emissions-vehicles-and-engines/final-rule-revise-existing-national-ghg-emissions.

U.S. Environmental Protection Agency, 2021b. The 2021 EPA Automotive Trends Report: Greenhouse Gas Emissions, Fuel Economy, and Technology since 1975. https://www.epa.gov/automotive-trends.

U.S. Environmental Protection Agency, 2021c. Annual certification data for vehicles, engines, and equipment, light-duty vehicles and trucks. https://www.epa.gov/compliance-and-fuel-economy-data/annual-certification-data-vehicles-engines-and-equipment.

U.S. Environmental Protection Agency, 2021d. Brake wear particle emission rates and characterization. Technical report EPA-420-R-21-009. https://nepis.epa.gov/Exe/ZyPDF.cgi?Dockey=P1013TSX.pdf.

Velji, A., Yeom, K., Wagner, U., Spicher, U., Roßbach, M., Suntz, R., Bockhorn, H., 2010. Investigations of the formation and oxidation of soot inside a direct injection spark ignition engine using advanced laser-techniques. SAE Technical Paper 2010-01-0352 https://doi.org/10.4271/2010-01-0352.

Wang, H., 2011. Formation of nascent soot and other condensed-phase materials in flames. Proc. Combust. Inst. 33 (1), 41–67. https://doi.org/10.1016/j.proci.2010.09.009.

Wang, H., Frenklach, M., 1997. A detailed kinetic modeling study of aromatics formation in laminar premixed acetylene and ethylene flames. Combust. Flame 110 (1–2), 173–221. https://doi.org/10.1016/S0010-2180(97)00068-0.

Wang, X., Grose, M.A., Caldow, R., Osmondson, B.L., Swanson, J.J., Chow, J.C., Hu, S., 2016. Improvement of engine exhaust particle sizer (EEPS) size distribution measurement–II. Engine exhaust particles. J. Aerosol Sci. 92, 83–94. https://doi.org/10.1016/j.jaerosci.2015.11.003.

Wang, J., Yan, F., Fang, N., Yan, D., Zhang, G., Wang, Y., Yang, W., 2020a. An experimental investigation of the impact of washcoat composition on gasoline particulate filter (GPF) performance. Energies 13 (3), 693. https://doi.org/10.3390/en13030693.

Wang, Y., Kamp, C.J., Wang, Y., Toops, T.J., Su, C., Wang, R., Wong, V.W., 2020b. The origin, transport, and evolution of ash in engine particulate filters. Appl. Energy 263, 114631. https://doi.org/10.1016/j.apenergy.2020.114631.

Wei, H., Zhu, T., Shu, G., Tan, L., Wang, Y., 2012. Gasoline engine exhaust gas recirculation–a review. Appl. Energy 99, 534–544. https://doi.org/10.1016/j.apenergy.2012.05.011.

Whelan, I., Timoney, D., Smith, W., Samuel, S., 2013. The effect of a three-way catalytic converter on particulate matter from a gasoline direct-injection engine during cold-start. SAE Int. J. Engines 6 (2), 1035–1045.. https://www.jstor.org/stable/26277681.

Whitaker, P., Kapus, P., Ogris, M., Hollerer, P., 2011. Measures to reduce particulate emissions from gasoline DI engines. SAE Int. J. Engines 4 (1), 1498–1512.. https://www.jstor.org/stable/26278238.

White House, Office of the Press Secretary, 2012. Obama Administration Finalizes Historic 54.5 MPG Fuel Efficiency Standards. https://obamawhitehouse.archives.gov/the-press-office/2012/08/28/obama-administration-finalizes-historic-545-mpg-fuel-efficiency-standard.

Winkler, S.L., Anderson, J.E., Garza, L., Ruona, W.C., Vogt, R., Wallington, T.J., 2018. Vehicle criteria pollutant (PM, NOx, CO, HCs) emissions: how low should we go? Npj Clim. Atmos. Sci. 1 (1), 1–5. https://doi.org/10.1038/s41612-018-0037-5.

Woo, S.H., Jang, H., Na, M.Y., Chang, H.J., Lee, S., 2022. Characterization of brake particles emitted from non-asbestos organic and low-metallic brake pads under normal and harsh braking conditions. Atmos. Environ. 278, 119089. https://doi.org/10.1016/j.atmosenv.2022.119089.

Wooldridge, M.S., Singh, R., Gutierrez, L.G., Clancy, S., 2022. Survey of strategies to reduce cold-start particulate, CO, NOx, and hydrocarbon emissions from direct-injection spark-ignition engines. Int. J. Engine Res. https://doi.org/10.1177/14680874211068576 14680874211068576.

Wu, J., Song, K.H., Litzinger, T., Lee, S.Y., Santoro, R., Linevsky, M., Liscinsky, D., 2006. Reduction of PAH and soot in premixed ethylene–air flames by addition of ethanol. Combust. Flame 144 (4), 675–687. https://doi.org/10.1016/j.combustflame.2005.08.036.

Wu, S., Xu, M., Hung, D.L., Li, T., Pan, H., 2016. Near-nozzle spray and spray collapse characteristics of spark-ignition direct-injection fuel injectors under sub-cooled and superheated conditions. Fuel 183, 322–334. https://doi.org/10.1016/j.fuel.2016.06.080.

Xu, F., Sunderland, P.B., Faeth, G.M., 1997. Soot formation in laminar premixed ethylene/air flames at atmospheric pressure. Combust. Flame 108 (4), 471–493. https://doi.org/10.1016/S0010-2180(96)00200-3.

Xu, H., Wang, C., Ma, X., Sarangi, A.K., Weall, A., Krueger-Venus, J., 2015. Fuel injector deposits in direct-injection spark-ignition engines. Prog. Energy Combust. Sci. 50, 63–80. https://doi.org/10.1016/j.pecs.2015.02.002.

Yamaguchi, A., Koopmans, L., Helmantal, A., 2019. Characterization of Gasoline Direct Injection Sprays Under Fuel Injection Pressure up to 150 MPa with Different Nozzle Geometries, SAE Technical Paper 2019-01-0063. https://doi.org/10.4271/2019-01-0063.

Yang, J., Roth, P., Durbin, T.D., Johnson, K.C., Cocker III, D.R., Asa-Awuku, A., Karavalakis, G., 2018. Gasoline particulate filters as an effective tool to reduce particulate and polycyclic aromatic hydrocarbon emissions from gasoline direct injection (GDI) vehicles: a case study with two GDI vehicles. Environ. Sci. Technol. 52 (5), 3275–3284. https://doi.org/10.1021/acs.est.7b05641.

Yang, J., Roth, P., Durbin, T.D., Shafer, M.M., Hemming, J., Antkiewicz, D.S., Karavalakis, G., 2019a. Emissions from a flex fuel GDI vehicle operating on ethanol fuels show marked contrasts in chemical, physical and toxicological characteristics as a function of ethanol content. Sci. Total Environ. 683, 749–761. https://doi.org/10.1016/j.scitotenv.2019.05.279.

Yang, J., Roth, P., Durbin, T.D., Johnson, K.C., Asa-Awuku, A., Cocker III, D.R., Karavalakis, G., 2019b. Investigation of the effect of mid-and high-level ethanol blends on the particulate and the mobile source air toxic emissions from a gasoline direct injection flex fuel vehicle. Energy Fuel 33 (1), 429–440. https://doi.org/10.1021/acs.energyfuels.8b02206.

Yang, J., Roth, P., Zhu, H., Durbin, T.D., Karavalakis, G., 2019c. Impacts of gasoline aromatic and ethanol levels on the emissions from GDI vehicles: part 2. Influence on particulate matter, black carbon, and nanoparticle emissions. Fuel 252, 812–820. https://doi.org/10.1016/j.fuel.2019.04.144.

Yang, L., Yu, B., Yang, B., Chen, H., Malima, G., Wei, Y.M., 2021. Life cycle environmental assessment of electric and internal combustion engine vehicles in China. J. Clean. Prod. 285, 124899. https://doi.org/10.1016/j.jclepro.2020.124899.

Yao, B., Lv, J., Xiao, D., Li, X., Jin, S., 2021. Tip-wetting film analysis using laser-induced fluorescence for multihole gasoline direct injectors under flash boiling conditions. Energy Fuel https://doi.org/10.1021/acs.energyfuels.1c03410.

Yi, J., Wooldridge, S., Coulson, G., et al., 2009. Development and optimization of the ford 3.5L V6 EcoBoost combustion system. SAE Int. J. Engines 2, 1388–1407. https://www.jstor.org/stable/26308477.

Yu, S., Yin, B., Bi, Q., Chen, C., Jia, H., 2021. Experimental and numerical investigation on inner flow and spray characteristics of elliptical GDI injectors with large aspect ratio. Energy 224, 120119. https://doi.org/10.1016/j.energy.2021.120119.

Yue, H., Lehmen, A., Van Nieuwstadt, M., Pan, Z., Wang, J., Fang, Z., 2021. A study on the filtration efficiency and regeneration capacity of the gasoline particulate filter. Proc. Inst. Mech. Eng. D 235 (2–3), 346–361. https://doi.org/10.1177/0954407020962633.

Zelenyuk, A., Wilson, J., Imre, D., Stewart, M., Muntean, G., Storey, J., Parks, J., 2017. Detailed characterization of particulate matter emitted by lean-burn gasoline direct injection engine. Int. J. Engine Res. 18 (5–6), 560–572. https://doi.org/10.1177/1468087416675708.

Zhang, S., McMahon, W., 2012. Particulate emissions for LEV II light-duty gasoline direct injection vehicles, SAE Technical Paper 2012–01-0442. https://www.jstor.org/stable/26272697.

Zhang, S., McMahon, W., Toutoundjian, H., Cruz, M., Frodin, B., 2010. Particulate mass and number emissions from light-duty low emission gasoline vehicles. SAE Technical Paper 2010-01-0795 https://doi.org/10.4271/2010-01-0795.

Zhang, R., Howard, K., Kirkman, P., Browne, D., Lu, Z., He, S., Boger, T., 2019. A study into the impact of engine oil on gasoline particulate filter performance through a real-world fleet test. SAE Technical Paper 2019-01-0299 https://doi.org/10.4271/2019-01-0299.

Zhang, W., Ma, X., Xinhui, L., Shuai, S., Wu, K., Macias, J., Guan, L., 2020. Impact of Fuel Properties on GDI Injector Deposit Formation and Particulate Matter Emissions. SAE Technical Paper 2020-01-0388. https://doi.org/10.4271/2020-01-0388.

Zhang, X., Xiao, D., Qiu, S., Li, T., Su, J., Hung, D.L., Xu, M., 2021. Influence of different injector structures on tip wetting by visualization method. International Conference on Liquid Atomization and Spray Systems (ICLASS). 1 No. 1.

Zhao, Y., Lambe, A.T., Saleh, R., Saliba, G., Robinson, A.L., 2018. Secondary organic aerosol production from gasoline vehicle exhaust: effects of engine technology, cold start, and emission certification standard. Environ. Sci. Technol. 52 (3), 1253–1261. https://doi.org/10.1021/acs.est.7b05045.

Zinola, S., Leblanc, M., Boréave, A., R'Mili, B., Cartoixa, B., Vernoux, P., Raux, S., 2013. The particulate number emissions from GDI engines: Advanced characterization and reduction through a gasoline particulate filter with membrane technology. SIA Paper.

zum Hagen, F.H.F., Mathissen, M., Grabiec, T., Hennicke, T., Rettig, M., Grochowicz, J., Benter, T., 2019. Study of brake wear particle emissions: impact of braking and cruising conditions. Environ. Sci. Technology 53 (9), 5143–5150. https://doi.org/10.1021/acs.est.8b07142.

zum Hagen, F.H.F., Mathissen, M., Grabiec, T., Hennicke, T., Rettig, M., Grochowicz, J., Benter, T., 2019. On-road vehicle measurements of brake wear particle emissions. Atmospheric Environment 217, 116943. https://doi.org/10.1016/j.atmosenv.2019.116943.